

RADIO PROPAGATION IN HALLWAYS AND STREETS  
FOR UHF COMMUNICATIONS

A DISSERTATION  
SUBMITTED TO THE DEPARTMENT OF ELECTRICAL ENGINEERING  
AND THE COMMITTEE ON GRADUATE STUDIES  
OF STANFORD UNIVERSITY  
IN PARTIAL FULFILLMENT OF THE REQUIREMENTS  
FOR THE DEGREE OF  
DOCTOR OF PHILOSOPHY

Dana Porrat  
December 2002

© Copyright by Dana Porrat 2003  
All Rights Reserved

I certify that I have read this dissertation and that, in my opinion, it is fully adequate in scope and quality as a dissertation for the degree of Doctor of Philosophy.

---

Donald C. Cox  
(Principal Adviser)

I certify that I have read this dissertation and that, in my opinion, it is fully adequate in scope and quality as a dissertation for the degree of Doctor of Philosophy.

---

Antony C. Fraser-Smith

I certify that I have read this dissertation and that, in my opinion, it is fully adequate in scope and quality as a dissertation for the degree of Doctor of Philosophy.

---

Andrea Goldsmith

Approved for the University Committee on Graduate Studies:

# Abstract

Models of radio propagation are indispensable in the design and analysis of wireless communication systems. They are used to predict power and interference levels and analyze other properties of the radio link. Guidance of radio waves along urban streets is a well known phenomenon; a similar effect takes place along indoor hallways. We propose a propagation model based on the wave-guiding characteristics of hallways and streets that captures the dominant propagation mechanism in these environments and predicts average power levels along the structure, near junctions and in adjacent rooms. A substantial decrease of power level is predicted when the receiver turns a corner from a waveguide that guides high power into a side waveguide, even where the waveguide that carries power continues after the intersection.

The waveguide model is multi-moded and includes coupling among the propagating modes that is caused by the roughness of the waveguide walls. The mode coupling is a key feature of the waveguide; it is used to explain the changes of the propagation characteristics along the structure. In addition to predicting power levels, the model is useful in analyzing the capacity of indoor multiple antenna systems and the delay profile in micro-cellular systems.

The waveguide model offers physical insight into observed phenomena in communication systems. It gives simple intuition to power levels near junctions, leakage from hallways to rooms, delay profiles and capacity of multiple antenna systems. This intuition is an innovation offered by the waveguide model that is not available in currently used propagation models.

# Acknowledgments

I thank my advisor, Professor Cox, for his guidance and good advice, and for presenting me the data that initiated my interest in propagation near street intersections. I thank Persa Kyritsi for her very pleasant cooperation working on the radio channel capacity of indoor hallways, and for letting me use her measurement data. I also thank Dr. James Whitteker of Marconi and Dr. L. Damosso and Dr. L. Stola of CSELT for their Ottawa and Turin measurement data, that helped me develop the model and compare it with reality.

I thank the Stanford Graduate Fellowship for supporting me financially in the last three years in Stanford, this support allowed me to spend most of my time on research and thoroughly enjoy my years as a graduate student.

Most importantly, I want to thank my friends and especially Yonatan, who changed my life in the last two years. We spent most of the time in different parts of the world but we play the game of life together.

I am grateful to Tony Fraser-Smith for his support and guidance throughout my career. He was a great inspiration to my research and life in general.

I thank Jacob Bortnik for our friendship that started in the courses we took in our first year at Stanford and continues as we mature in our different fields. Good luck with your dissertation, Jacob.

# Contents

<b>Abstract</b>	<b>iv</b>
<b>Acknowledgments</b>	<b>v</b>
<b>1 Introduction</b>	<b>1</b>
<b>2 The Model</b>	<b>6</b>
2.1 A Smooth Multi-Moded Waveguide . . . . .	6
2.1.1 The Power Carried by the Modes . . . . .	12
2.1.2 The Orthogonality of the Modes . . . . .	13
2.2 A Rough Waveguide . . . . .	14
2.2.1 The Coupled Power Equations . . . . .	21
2.2.2 Solution to the Coupled Power Equation . . . . .	25
2.2.3 The TEM mode . . . . .	27
2.2.4 Penetration into Sidewalls . . . . .	27
2.3 A Three Dimensional Waveguide . . . . .	28
2.4 Junctions in the Waveguide . . . . .	29
2.5 Summary of the Model . . . . .	32
<b>3 Indoor Power Measurements</b>	<b>33</b>
3.1 Stanford Measurements . . . . .	33
3.1.1 The Measurement Setup . . . . .	33
3.1.2 Environment . . . . .	36
3.1.3 Measurement Results . . . . .	36
3.1.4 Comparison of Measurement and Theory . . . . .	46

3.2	Crawford Hill Measurements . . . . .	51
3.3	Summary of Indoor Power Measurements . . . . .	52
<b>4</b>	<b>Outdoor Power Measurements</b>	<b>55</b>
4.1	Single Street Measurements (Turin) . . . . .	56
4.2	Measurements Across a City (Ottawa) . . . . .	56
<b>5</b>	<b>Delay Spread</b>	<b>64</b>
5.1	Waveguide Dispersion . . . . .	64
5.2	Calculation of the Delay Profile . . . . .	65
5.3	Comparison with an Empirical Model . . . . .	68
<b>6</b>	<b>Channel Capacity</b>	<b>70</b>
6.1	Theoretical Analysis . . . . .	71
6.1.1	Channel Capacity in a Smooth Waveguide . . . . .	72
6.1.2	Channel Capacity in a Rough Waveguide . . . . .	73
6.2	Measurements . . . . .	75
6.3	The Measurement Setup and Environment . . . . .	81
<b>7</b>	<b>Conclusion</b>	<b>84</b>
<b>A</b>	<b>Stanford Measurement File Format</b>	<b>88</b>
A.1	Measurement File Names . . . . .	92
<b>B</b>	<b>Matlab Code</b>	<b>93</b>
B.1	lossy_wg4.m . . . . .	93
B.2	pert_wg19.m . . . . .	96
	<b>Bibliography</b>	<b>110</b>

# List of Tables

4.1	Parameters for Ottawa east–west streets. . . . .	62
4.2	Parameters for Ottawa north–south streets. . . . .	62

# List of Figures

2.1	A smooth slab waveguide . . . . .	7
2.2	A rough slab waveguide . . . . .	15
2.3	A rough wall near $x = a$ . . . . .	17
2.4	A steady state distribution of power over modes. The horizontal axis is the mode number and the vertical axis is power on a logarithmic scale. . . . .	26
2.5	A waveguide junction model. The solid line represents a low order mode of the main waveguide coupled into a high order mode of the side waveguide. The dashed line represents a high order mode of the main waveguide coupled into a low order mode of the side waveguide. . . . .	30
3.1	The Measurement Setup . . . . .	34
3.2	The Receiver Cart . . . . .	34
3.3	Locations of the transmitter and receiver in the Packard basement, with median power level at each receiver location [dBm]. The single digit numbers indicate hallways and the two-digit numbers indicate rooms in the building. The lines indicate the inner boundary of the hallway and room walls. Details of the walls and doors were omitted. . . . .	37
3.4	Power received near the transmitter, the geometry is shown in Figure 3.3. The free space curve is an estimation based on measurements at close range. . . . .	38
3.5	Power received along a wall, the geometry is shown in Figure 3.6. The free space curve is an estimation based on measurements at close range. . . . .	39
3.6	Geometry of the measurements near room 75. . . . .	40

3.7	Median power in Hallway 1 and adjacent rooms. The hallway data is at points 0.5 m or more from both walls. The room data are obtained at points between 1 m and 5 m from one of the walls. . . . .	41
3.8	Power across Hallway 1 (median over band). Top: The receiver is 4.4 m from the transmitter. Bottom: The receiver is 12 m from the transmitter, and in a smooth line the predicted power levels for the first order TE mode. The vertical lines indicate the inner boundary of the hallway walls. . . . .	42
3.9	Median power in Hallway 5 and adjacent rooms . . . . .	43
3.10	Median power in Hallway 3 and adjacent rooms . . . . .	44
3.11	Median power in Hallway 6 and adjacent rooms . . . . .	45
3.12	Median power in Hallway 1, with the theoretical prediction. Model parameters are $\epsilon = 3$ , $\sigma = 0.075$ S/ m, $D = 2$ m and $s^2 = 0.2$ m <sup>2</sup> and hallway width 1.8 m. The power distribution at the source is a TE narrow source in the middle of the hallway. The free space curve is an estimation based on measurements at close range. . . . .	47
3.13	Median power in Hallway 3, with the theoretical prediction. Model parameters are $\epsilon = 3$ , $\sigma = 0.075$ S/ m, $D = 2$ m and $s^2 = 0.2$ m <sup>2</sup> and hallway width 1.8 m. The power distribution at the junction is uniform. . . . .	48
3.14	Median power in Hallway 5, with the theoretical prediction. Model parameters are $\epsilon = 3$ , $\sigma = 0.075$ S/ m, $D = 2$ m and $s^2 = 0.2$ m <sup>2</sup> and hallway width 1.8 m. The power distribution at the junction is uniform. . . . .	49
3.15	Median power in Hallway 6, with the theoretical prediction. Model parameters are $\epsilon = 3$ , $\sigma = 0.075$ S/ m, $D = 2$ m and $s^2 = 0.2$ m <sup>2</sup> and hallway width 1.8 m. The power distribution at the junction is uniform. . . . .	50
3.16	Measurement and theoretical prediction for Crawford Hill. The measured power is indicated with small square dots and the theoretical prediction with a smooth line. The large round dots indicate the predicted power in free space. Measurement data and the free space curve from [15].	

4.1	Measurements and calculation. Measurements taken in Via Baracca, Turin, Italy, moving north away from Via Coppino (that contained the transmitter). . . . .	57
4.2	Measurements and calculation. Measurements taken in Via Baracca, Turin, Italy, moving south away from Via Coppino (that contained the transmitter). . . . .	58
4.3	Map of Ottawa, Canada, with a transmitter at 300 Slater St. (marked by concentric circles) and path loss levels indicated by bars. Reproduction of figure 1 from J. H. Whitteker, ‘Measurement of Path Loss at 910 MHz for Proposed Microcell Urban Mobile Systems’, IEEE Transactions on Vehicular Technology, August 1988, Vol. 37, No. 3, ©1988 IEEE. The numbers 1–3 and the letters A–D were added to indicate city blocks. . .	59
4.4	Measured Power and Prediction in Ottawa, North–South Streets . . . .	60
4.5	Measured Power and Prediction in Ottawa, East–West Streets . . . . .	61
5.1	The wave vector and its components . . . . .	65
5.2	The modes of a hollow slab waveguide, described in an angular diagram. The cross–waveguide component of the wave vector increases at more or less fixed steps, while the parallel components of the low order modes are clustered. . . . .	66
5.3	Delay profile of a multi-moded waveguide 300 m long with no mode coupling. The arrival time and power of each mode is indicated by a vertical line. Power distribution among the modes is the steady state distribution for a waveguide with mode coupling. . . . .	67
5.4	Delay profile of a multi-moded waveguide with no mode coupling, based on the steady state mode power distribution for a waveguide with mode coupling. The graph indicates the (normalized) predicted power at a receiver in the waveguide, 300 m from the transmitter. The delay profile calculated from <i>Ichitsubo</i> ’s empirical model and from COST207 are also plotted. . . . .	68

6.1	Average power along the hallway. The straight line indicates the approximate steady state power loss rate. The short vertical lines indicate the minimum and maximum power levels received at each location. . . . .	76
6.2	Power measured across the hallway. For the top plot, the receiver is 6.4 m from the transmitter, the middle plot is at 35.7 m and the bottom plot is at 73.2 m . . . . .	77
6.3	Average capacity of the measured channel in the hallway for SNR=20 dB and theoretically calculated capacity. . . . .	78
6.4	Antenna arrangement used in the waveguide calculation . . . . .	79
6.5	Average capacity of the measured channel in the labs for SNR=20 dB, for the receiver antenna facing the four cardinal directions. . . . .	80
6.6	Antenna array layout, V and H represent different polarizations. . . . .	82
6.7	Geometry of hallways with the transmitter location and two receiver locations . . . . .	82
A.1	A single measurement, the mean (-44.7 dB) is indicated in a dashed line and the median (-45.1 dB) in a full line. . . . .	91

# Chapter 1

## Introduction

Propagating radio waves are the basis for wireless communication systems. Understanding this propagation is very important in the design and layout of such systems, especially when they contain mobile terminals. Modeling of radio channels has been an active area of research for many years, and the frequency band of interest shifts with the demands of concurrent communication systems.

Mobile voice communications had gained immense popularity in the last decade. Mobile systems are characterized by a link between a fixed base station and a small mobile device. They operate in the ultra high frequency (UHF) band, 300 MHz – 3 GHz, with future systems planned in higher frequency bands.

Mobile data systems have been gaining popularity in recent years, they operate in the UHF band and above, in the 3-6 GHz frequency range. These systems operate with smaller coverage than voice systems, and higher data rates. Considerable attention is paid to coverage inside big buildings that hold a concentration of users.

### Channel Models

Good radio channel models are necessary for the effective design of transmitters and receivers, and for determining the positions of the base stations. Propagation models range from deterministic to stochastic: Deterministic channel models predict field strength in an area around a transmitter and take into account the structure and materials used at every location in the area. A fully deterministic model requires a huge amount of structural data which are rarely available. Stochastic channel models predict average field

strength and the variations around this average. A purely stochastic model does not take into account the details of the radio propagation environment. Stochastic models are simple and require little computing resources. They are useful in the design of radio systems, where the layout area is not known or where it is very large and varied.

When some knowledge of the propagation environment is available, channel models that combine known features of this environment with the statistics of radio propagation are widely used. Propagation models that combine the deterministic and stochastic approach constitute the main area of research in propagation modeling. The model suggested in this work belongs in this category.

Power law models [72, 38, 2, 28] constitute an important family of semi-stochastic models, where the average power level is given by the distance raised to some power that depends on the environment. When used in indoor situations, the loss caused by walls and floors is often treated deterministically [72].

Ray tracing is the most common approach to modeling specific environments. The transmitter is modeled as a source of many rays in all directions around it. Each ray is traced as it bounces and penetrates different objects in the environment including, most importantly, the ground and walls. An important addition to ray tracing is the uniform diffraction theory (UTD), which improves the accuracy of ray tracing models near corners and roof edges. The literature on ray tracing is vast, we note here only some of the important contributions. *Bertoni* and his collaborators [5, 4, 85] pioneered much of the development and introduced rooftop diffraction. *Tan* and *Tan* [80, 81, 82] formulated the UTD theory, and *Erceg* and others [26, 27, 29] made important contributions relating the theory to propagation measurements.

Ray tracing models require a large amount of information to describe the environment, because each surface has to be modeled in terms of its accurate position and material properties. When considering a large area with many obstacles, a very large number of rays is needed in order to provide reasonable accuracy of the predictions. As a result, ray tracing models are computationally complex. For example, the calculation of power levels over one floor of a large building requires a few hours of computation on a current desktop computer. The accuracy in the areas far from the transmitter deteriorates significantly, because of the accumulation of errors due to interactions with objects that cannot be modeled exactly.

The waveguide model is superior to ray tracing in modeling long structures (hallways and streets) because it describes the main propagation phenomenon (i.e. guiding along the structures). In contrast to ray tracing, only a very simple average description of the environment is required, namely two parameters describing the wall materials and two parameters describing the wall roughness. A ray tracing calculation requires as input a detailed description of the environment, because every point of reflection of each ray from a surface has to be characterized in terms of the surface material and geometry. A calculation of power levels based on the waveguide model requires an order of magnitude less computer resources than the equivalent ray tracing computation, both in the number of operations and in the size of the input.

### **Guiding by Hallways and Streets**

Guiding of radio waves by indoor hallways in large buildings is a dominant propagation mechanism, as shown in [41, 2] and in Chapter 3. Similarly, guiding of waves along urban streets (the ‘street canyon’ effect) is dominant in areas with tall buildings [38, 22, 24, 67, 51].

The dominance of the guiding effect calls for a propagation model based on this premise. The model presented in this thesis concentrates on the guiding of radio waves in hallway and street environments. It predicts average power levels and other properties of the radio channel, while requiring as input only a simple description of the environment without much detail. Specifically, the required parameters are the width of the hallway/street, the statistics of the wall roughness (variance and correlation length), and the average electrical parameters (dielectric constant and conductivity) of the construction materials.

Waveguides are long structures that confine radiation and guide it. Dielectric waveguides, such as optical fibers, guide radiation because of the reflective properties of their coating. Hollow waveguides such as the model brought here guide radiation because their boundaries are reflective and because radiation that penetrates into the surrounding material is attenuated.

Propagation in waveguides is characterized by modes that act as the eigenfunctions of the structure, in the sense that power can travel along the guide only if the field shapes conform to the modal shapes. The modal fields can be calculated from the boundary

conditions of the waveguide and they depend on the materials of the waveguide and the surrounding environment and on the waveguide geometry.

The number of different modes in a waveguide depends on the ratio between the waveguide dimensions and the wavelength. A waveguide with width (or diameter, for a cylindrical guide) of around half the wavelength can normally carry a single mode, sometimes two modes with different polarization. Larger waveguides carry more modes and they are called ‘multimoded’ waveguides. The rule of thumb is that the number of modes per polarization approximately equals the ratio of the waveguide width or diameter to half the wavelength.

The modes of a waveguide are orthogonal, i.e. the power carried in the waveguide can be calculated as the sum of the mode power. In ideal waveguides (structures made of uniform material with smooth boundaries) there is no coupling, so power is not transferred from one mode to another. Imperfections in the waveguide geometry or the uniformity of the materials cause mode coupling, which means that power is transferred from some modes to others.

Waveguide models in radio communications have been suggested for tunnels [25], but the common approach to propagation in tunnels is ray tracing [14, 18, 32, 54, 88]. These waveguides are hollow, with non uniform walls, the roughness of the walls is taken into account in [25, 54, 88]. Measurement results of attenuation levels of radio waves in tunnels are shown in [38] Section 2.2.9.

A waveguide model for urban streets was suggested by *Blaunstein* and co-authors [6, 7, 8, 9]; their model is based on a waveguide with smooth walls, so it does not include the effects of coupling (transfer of power) among the waveguide modes. A waveguide model for indoor hallways has not been investigated in the literature, despite the importance of the guiding by indoor hallways.

Hollow waveguide theory was developed mainly for use in the analysis of lasers; an important early work is [55]. The fields of the modes of a rectangular waveguide are given in [1, 48], and a graphic solution of the characteristic equation is given in [69]. A good review of the hollow multimoded waveguide is given in [21]. Multimoded waveguides with rough walls gained interest in the 1960s and 1970s, when optical fibers were thick (and therefore multimoded), and the smoothness of the surface was limited by the production processes. The most important work on multimoded rough waveguides was

published in a series of papers by *Marcuse* [56, 57, 58, 62]; other relevant publications are [34, 84].

The roughness of the walls is a significant feature of a waveguide because even a small roughness causes coupling among the waveguide modes. For a general discussion of scattering off rough surfaces see [37]. *Landron et al.* investigated the reflection coefficients of typical exterior surfaces [50, 49], and showed that the roughness of the surfaces is significant at 2 and 4 GHz. Rough surface scattering in ray tracing models (also called ‘diffuse scattering’) was investigated in [19, 44, 20].

The waveguide model is developed in Chapter 2. The model starts with an ideal waveguide with smooth walls and is then generalized to a waveguide with rough walls that cause mode coupling. The waveguide model is useful in predicting power levels in the hallways of big buildings as well as in the rooms adjacent to them which receive power mostly by leakage from the hallway. Our model gives particular insight into the power levels measured near hallway junctions and around corners. Similarly, the model is useful in predicting power levels in the streets of an urban grid and near street intersections. Chapter 3 shows power levels measured in buildings and Chapter 4 shows measurements from urban environments.

This work emphasizes hallways over streets because the hallways hold fewer modes than the streets in the UHF band, and the wall roughness is of a smaller scale in hallways, normally smaller than a wavelength in this frequency band. Thus, the model assumptions are a better description of the actual situation in hallways than in streets.

Our waveguide model is useful in predicting the delay spread and the shape of the delay profile in the indoor/urban environments. The predicted shape compares well with measurements, and provides an intuition that connects the propagation process with the delay profile. Chapter 5 compares our model to an empirical delay profile model for microcells.

The model also predicts a reduction of channel capacity along hallways/streets, that agrees with indoor measurements. The predictions provide physical insight into the behavior of channel capacity, see Chapter 6 for details.

# Chapter 2

## The Model

A waveguide model with smooth walls is discussed in Section 2.1 as a basis for the theory. This model is extended by considering rough (non-smooth) walls in Section 2.2. The theory is based on optical fiber literature, in particular publications by *Marcuse* [64, 56]. The model is extended from a slab (two dimensional) waveguide to three dimensions in section 2.3, junctions are discussed in Section 2.4.

### 2.1 A Smooth Multi-Moded Waveguide

The simple model we present here consists of a slab waveguide, which represents a hallway or a street. The walls of the waveguide are made of a lossy dielectric material (Figure 2.1). The waveguide is filled with air, so between the walls we assume the electrical properties of free space. With this simple model, we ignore the effects of the ground and ceiling and any objects within the waveguide (such as people, cars and trees). The ceiling, floor and ground are discussed in Section 2.3.

In this section we discuss a waveguide with smooth homogeneous walls, as a basis for the presentation of the more complicated waveguide with rough walls in the next section. The waveguide can be defined in terms of its width and the relative complex dielectric constant of the walls  $\epsilon$ :

$$\epsilon_s(x, z) = \begin{cases} 1 & |x| \leq a \\ \epsilon & |x| > a \end{cases} \quad (2.1)$$

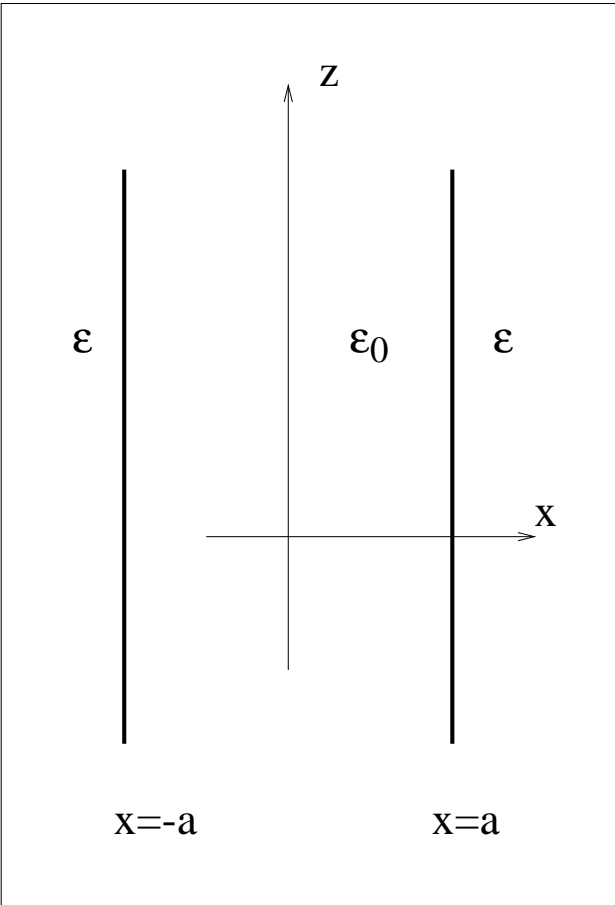


Figure 2.1: A smooth slab waveguide

where  $\epsilon_s(x, z)$  stands for the relative dielectric constant of the smooth waveguide. The permeability is fixed at the vacuum value of  $\mu_0 = 4\pi \times 10^{-7}$  H/m for the walls and interior of the waveguide.

Hollow dielectric waveguides gained interest in the 1970s, when they were considered for laser structures [1, 21, 43, 48, 61, 68, 69]. We are interested in multi-moded waveguides because the normal width of hallways and streets is many times the wavelength; a typical hallway is about 2 m wide and a street may be 10 – 30 m wide, and the wavelength in the UHF band varies between 10 cm and 1 m.

We follow the waveguide analysis presented by *Adam and Kneubühl* [1] in the discussion of the smooth lossy hollow waveguide. Consider a slab waveguide of width  $2a$  with propagation along the  $z$  direction. There is no variation in the  $y$  direction so  $\partial/\partial y = 0$ . The lossy dielectric walls of the waveguide have the relative complex dielectric constant

$$\epsilon = \epsilon' + j\epsilon'' = \epsilon_r - j\frac{\sigma}{\omega\epsilon_0} \quad (2.2)$$

where  $\epsilon_r$  is the relative permittivity (dielectric constant) of the walls,  $\sigma$  is their conductivity;  $\omega$  is the angular frequency, the time dependence is  $e^{j\omega t}$  and  $\epsilon_0 = 8.85 \times 10^{-12}$  F/m is the vacuum dielectric constant. High conductivity values ( $\sigma$ ) increase the losses in the side walls and low dielectric constants ( $\epsilon_r$ ) lower the reflectivity of the side walls, also causing an increase of the losses.

The field expressions for the transverse electric (TE) modes inside the waveguide  $|x| \leq a$  are brought from [1]:

$$E_x = 0 \quad (2.3)$$

$$E_y = j\frac{k}{k_x}Z_0\mathcal{H}\left\{\begin{array}{l} \cos(k_x x) \\ \sin(k_x x) \end{array}\right\}e^{j\omega t - j\beta z} \quad (2.4)$$

$$E_z = 0 \quad (2.5)$$

$$H_x = j\frac{k_x^2 - k^2}{k_x\beta}\mathcal{H}\left\{\begin{array}{l} \cos(k_x x) \\ \sin(k_x x) \end{array}\right\}e^{j\omega t - j\beta z} \quad (2.6)$$

$$H_y = 0 \quad (2.7)$$

$$H_z = \left\{\begin{array}{l} - \\ + \end{array}\right\}\mathcal{H}\left\{\begin{array}{l} \sin(k_x x) \\ \cos(k_x x) \end{array}\right\}e^{j\omega t - j\beta z} \quad (2.8)$$

The transverse magnetic (TM) modes:

$$E_x = j \frac{k_x^2 - k^2}{k_x \beta} \mathcal{E} \begin{Bmatrix} \cos(k_x x) \\ \sin(k_x x) \end{Bmatrix} e^{j\omega t - j\beta z} \quad (2.9)$$

$$E_y = 0 \quad (2.10)$$

$$E_z = \begin{Bmatrix} + \\ - \end{Bmatrix} \mathcal{E} \begin{Bmatrix} \sin(k_x x) \\ \cos(k_x x) \end{Bmatrix} e^{j\omega t - j\beta z} \quad (2.11)$$

$$H_x = 0 \quad (2.12)$$

$$H_y = -j \frac{k}{k_x} \frac{\mathcal{E}}{Z_0} \begin{Bmatrix} \cos(k_x x) \\ \sin(k_x x) \end{Bmatrix} e^{j\omega t - j\beta z} \quad (2.13)$$

$$H_z = 0 \quad (2.14)$$

The upper functions in (2.4), (2.6), (2.8), (2.9), (2.11), (2.13) apply to the symmetric modes and the lower to the antisymmetric modes, where the symmetry/antisymmetry characterizes the field component in the  $y$  direction. A few definitions:  $k = 2\pi/\lambda$  is the free space wave number, where  $\lambda$  is the free space wavelength.  $\beta = \sqrt{k^2 - k_x^2}$  and  $k_x = u/a$  represent the  $z$  and  $x$  components of the wave vector for propagation inside the waveguide, where  $u$  is the normalized wave vector in the  $x$  direction. In the walls of the waveguide, the propagation constant is  $k_2 = (\epsilon\mu_0\omega^2)^{1/2}$  and its  $x$  component is  $k_a = q/a$ ;  $q$  is the normalized wave vector in the  $x$  direction.  $Z_0 = \sqrt{\mu_0/\epsilon_0}$  is the vacuum impedance, and  $\mathcal{H}$  and  $\mathcal{E}$  are arbitrary field amplitudes.

The complex parameters  $u$  and  $q$  must be determined in order to complete the characterization of the modes. These parameters are related via the equation

$$u^2 + q^2 = \left(\frac{2\pi a}{\lambda}\right)^2 (1 - \epsilon) = R^2 \quad (2.15)$$

Using the boundary conditions, the characteristic equation can be formulated in terms of  $u$ , the propagation constant in the waveguide and  $R$ , which represents the properties of the waveguide:

For the TE modes:

$$\left\{ \begin{array}{c} \frac{u^2}{\cos^2 u} \\ \\ \frac{u^2}{\sin^2 u} \end{array} \right\} = R^2 \quad (2.16)$$

For the TM modes:

$$\left\{ \begin{array}{c} \cotan^2 u \\ \tan^2 u \end{array} \right\} = \frac{\epsilon^2 u^2}{R^2} - u^2 \quad (2.17)$$

where the upper equation applies to the symmetric modes and the lower to the antisymmetric.

An exact solution of the characteristic equations is very difficult. *Burke* [10] gives a graphical solution for the TE case but we follow [1] and discuss an approximate solution. We assume that the imaginary parts of  $\epsilon$  and  $u$  are small compared to their real parts. In order to test the assumption on  $\epsilon$  we calculate it for an example case of brick that has a relative electrical permittivity  $\epsilon_r = 4.44$  and a conductivity  $\sigma = 0.01$  S/m [50]. For radiation at 1 GHz,  $\epsilon = 4.44 - j0.18$ , so the imaginary part is indeed smaller than the real part and the assumption on  $\epsilon$  holds. The assumption on  $u$  relies on observing the solution obtained elsewhere (for example, in a graphical method).

Under these approximations on  $u$  and  $\epsilon$ , the characteristic values of  $u = u' + ju''$  are as follows [1] for the TE modes:

$$u' = \pi(1 - \eta) \frac{n}{2} \quad (2.18)$$

$$u'' = -\frac{\lambda}{2a(\epsilon_r - 1)^{1/2}} \frac{n}{2} \quad (2.19)$$

where

$$\eta = \frac{\epsilon'' \lambda}{4\pi a(\epsilon_r - 1)^{3/2}} \quad (2.20)$$

and

$$n = 1, 2, \dots \quad (2.21)$$

For the TM modes:

$$u' = \pi(1 - \eta) \frac{n}{2} \quad (2.22)$$

$$u'' = -\frac{\epsilon_r \lambda}{2a(\epsilon_r - 1)^{1/2}} \frac{n}{2} \quad (2.23)$$

where

$$\eta = \frac{\epsilon' + \frac{2\pi a}{\lambda} \epsilon'' (\epsilon_r - 1)^{1/2}}{(2\pi a/\lambda)^2 (\epsilon_r - 1)} \quad (2.24)$$

and

$$n = 1, 2, \dots \quad (2.25)$$

Odd values of  $n$  correspond to the symmetric modes and even values of  $n$  correspond to antisymmetric modes.

The propagation constant in the  $z$  direction is determined from  $\beta^2 = k^2 - (u/a)^2$ . By separating real and imaginary parts and neglecting terms of second degree we obtain the approximations for  $\beta = \beta' + j\beta''$  [1]:

$$\beta' = \left[ \left( \frac{2\pi}{\lambda} \right)^2 - \left( \frac{u'}{a} \right)^2 \right]^{1/2} \quad (2.26)$$

The imaginary part for the TE modes is given by:

$$\beta'' = -\frac{\lambda^2}{4a^3(\epsilon_r - 1)^{1/2}} \left( \frac{n}{2} \right)^2 \quad n = 1, 2, \dots \quad (2.27)$$

and for the TM modes:

$$\beta'' = -\frac{\epsilon_r \lambda^2}{4a^3(\epsilon_r - 1)^{1/2}} \left( \frac{n}{2} \right)^2 \quad n = 1, 2, \dots \quad (2.28)$$

The number of significant modes  $M$  (for a single polarization) is determined by the condition  $u' < ka$  and it can be approximated by  $M \approx 2a/\lambda$  (assuming  $\eta \ll 1$ ). When both TE and TM modes are considered, the number of significant modes is  $N = 2M$ . In order to appreciate the number of propagating modes in the street waveguide, we calculate  $M$  for  $a = 10$  m (the street width is 20 m) and  $\lambda = 30$  cm (carrier frequency 1 GHz), and find  $M = 67$  modes for each polarization. In a typical indoor hallway (2 m

wide) the number of modes is around  $M = 10$  per polarization for radiation at 1 GHz.

### 2.1.1 The Power Carried by the Modes

We now calculate the power carried by the different modes. The Poynting vector is given by

$$S = \frac{1}{2} \text{real} (\mathbf{E} \times \mathbf{H}^*) \quad (2.29)$$

For the TE modes the Poynting vector is given by

$$S_z \approx \frac{1}{2} \frac{k(k^2 a^2 - u_m'^2)}{u_m'^2 \beta_m'} Z_0 \mathcal{H}_m^2 \left\{ \begin{array}{l} \cos^2 \left( u_m' \frac{x}{a} \right) \\ \sin^2 \left( u_m' \frac{x}{a} \right) \end{array} \right\} \quad (2.30)$$

where the top function applies to the symmetric modes and the bottom to the antisymmetric as before. For the TM modes:

$$S_z \approx \frac{1}{2} \frac{k(k^2 a^2 - u_m'^2)}{u_m'^2 \beta_m'} \frac{\mathcal{E}_m^2}{Z_0} \left\{ \begin{array}{l} \sin^2 \left( u_m' \frac{x}{a} \right) \\ \cos^2 \left( u_m' \frac{x}{a} \right) \end{array} \right\} \quad (2.31)$$

The power  $P$  per unit length in the  $y$  direction is calculated by

$$P = \int_{-a}^a S_z dx \quad (2.32)$$

where we disregard the power propagating inside the walls of the waveguide. From this point on, we adopt the convention that the mode amplitudes  $\mathcal{H}_n$  and  $\mathcal{E}_n$  are normalized so that all the modes carry the same amount of power. We also assume that the modal amplitudes  $\mathcal{H}_n$  and  $\mathcal{E}_n$  are real and positive. When we later consider modes with different power levels or with complex amplitudes, we use a multiplicative coefficient for each mode. The power carried by each TE mode is given by

$$P = \frac{k \beta_m' a^3}{2 u_m'^2} Z_0 \mathcal{H}_m^2 = \frac{k a^3 Z_0}{2} \frac{\sqrt{\beta_m'} \mathcal{H}_m}{u_m'} \frac{\sqrt{\beta_n'} \mathcal{H}_n}{u_n'} \quad (2.33)$$

and the power carried by the TM modes is given by

$$P = \frac{k\beta'_m a^3 \mathcal{E}_m^2}{2u'_m{}^2 Z_0} = \frac{ka^3 \sqrt{\beta'_m} \mathcal{E}_m \sqrt{\beta'_n} \mathcal{E}_n}{2Z_0 u'_m u'_n} \quad (2.34)$$

where the last equations in (2.33) and (2.34) are due to our assumption of equal power carried by all the modes.

### 2.1.2 The Orthogonality of the Modes

We refer to two modes as orthogonal if the power carried by their combined fields when they propagate in the waveguide can be expressed as the sum of the powers carried by each mode separately. If  $P_T$  is the total power measured in a waveguide and  $\{P_n\}_{n=1}^N$  are the powers carried by  $N$  propagating modes, then these modes are orthogonal if

$$P_T = \sum_{n=1}^N P_n \quad (2.35)$$

The mode orthogonality is very useful in the development of the rough waveguide in Section 2.2, where the modes are used as a basis for a perturbation calculation.

A condition on mode orthogonality can be expressed in terms of the electric fields of the modes. Two modes are orthogonal if

$$I_{nm} = \int_{-a}^a \mathbf{E}_n \cdot \mathbf{E}_m dx = 0 \quad (2.36)$$

or, equivalently, if

$$I_{nm} = \int_{-a}^a \mathbf{H}_n \cdot \mathbf{H}_m dx = 0 \quad (2.37)$$

where  $\cdot$  represents the vector dot product. We now establish the orthogonality of the modes in a smooth waveguide. This is important because these modes are used in Section 2.2 as a basis for the representation of other waveforms. Clearly, any TE mode is orthogonal to any TM mode as their respective electric fields are geometrically orthogonal. The orthogonality of the TE modes is determined by the expression

$$I_{nm} = \int_{-a}^a E_{yn} E_{ym}^* dx \quad (2.38)$$

where  $E_{yn}$  represents the electric field of the  $n^{\text{th}}$  mode in the  $y$  direction. The orthogonality of the TM modes is determined via a similar expression that contains the magnetic field component in the  $y$  direction.

The modes of the hollow slab are approximately orthogonal, under the assumptions

$$u'' \ll u' \quad (2.39)$$

$$\eta \ll 1 \quad (2.40)$$

This can be verified by inserting the field expressions (2.3)–(2.14) in (2.36) or (2.37).

## 2.2 A Rough Waveguide

The roughness of real walls has to be taken into account when modeling indoor hallways and urban streets. In the first case, the wall roughness is generated by doors, pictures and other objects on the walls, and the variation of building materials. In the second (outdoor) case, the roughness results from door and windows recesses, plants, masonry decoration, etc.

In this section we consider slab waveguides made of uniform material, but the geometry of the walls is no longer smooth, as shown in Figure 2.2. The wall roughness causes coupling among the propagating modes.

The analysis of multi-moded waveguides and the coupling between the propagating modes started with a series of papers by *Marcuse* [56, 57, 58, 59, 60, 62] and was extended by others [11, 17, 34, 42, 79]. These works analyze a dielectric multi-moded optical fiber in order to predict the effects of production imperfections and to understand the effects of mode coupling on the dispersion of signals transmitted through the fiber.

We follow the approach taken by *Marcuse* in [56] to analyze the mode coupling caused by the roughness of the waveguide walls. We follow a perturbation analysis of the waveguide that uses the modes of the smooth waveguide as a basis; the analysis relies on the assumption of small perturbations of the wall geometry, where ‘small’ in this case is relative to the wavelength.

The roughness of the walls inside office buildings is the result of door recesses, pictures and other objects hung on the walls, and the roughness of the wall material

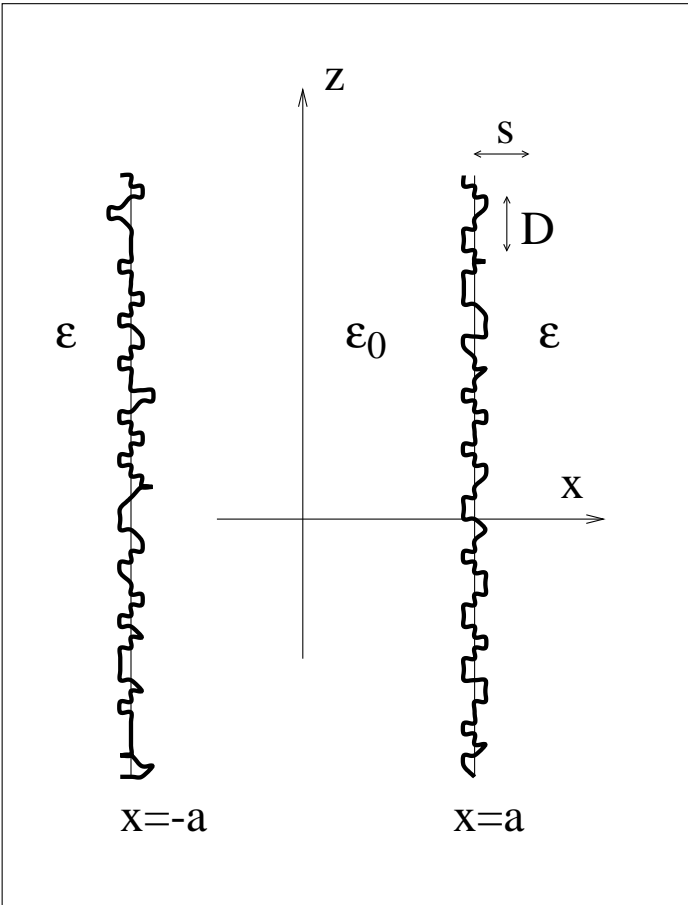


Figure 2.2: A rough slab waveguide

itself. Additionally, the variation of the electrical properties among the materials that constitute the walls increases the effective roughness. The geometric roughness is in the order of less than a wavelength in the UHF band, so the small perturbation assumption is acceptable.

In an outdoor environment the situation is different. Wall roughness is caused by rough construction materials (such as bricks and plaster), with bigger perturbations caused by building elements such as windows, masonry decoration, doors and metal bars. The wall roughness is in the order of a wavelength, and the small perturbation assumption holds only in the lower frequencies in the UHF band. However, the coupled waveguide model is useful as a simple first order approximation of a more complex reality, and the qualitative intuitions it offers are useful.

The two dimensional model is maintained, where there is no variation in the  $y$  direction. The wall boundary near  $x = a$  is given by the function  $x = f(z)$  (Figure 2.3) and the boundary near  $x = -a$  is given by  $x = h(z)$ . We characterize the wall perturbations statistically, using their correlation functions, where we assume that the perturbations on both walls are independent of each other and stationary in the wide sense, i.e. the statistical properties do not change along the street. For any point  $z_0$  along the waveguide:

$$\langle [f(z_0) - a][f(z_0 + z) - a] \rangle = s^2 e^{-(z/D)^2} \quad (2.41)$$

where  $s$  is the rms deviation of the wall from perfect straightness and  $D$  is the correlation length. We assume the same statistics for  $h(z)$  that defines the deviations of the wall near  $x = -a$ . The Gaussian correlation assumption may not be exact, but it captures the two important features of wall variation and of every correlation function, namely a correlation length and a variance.

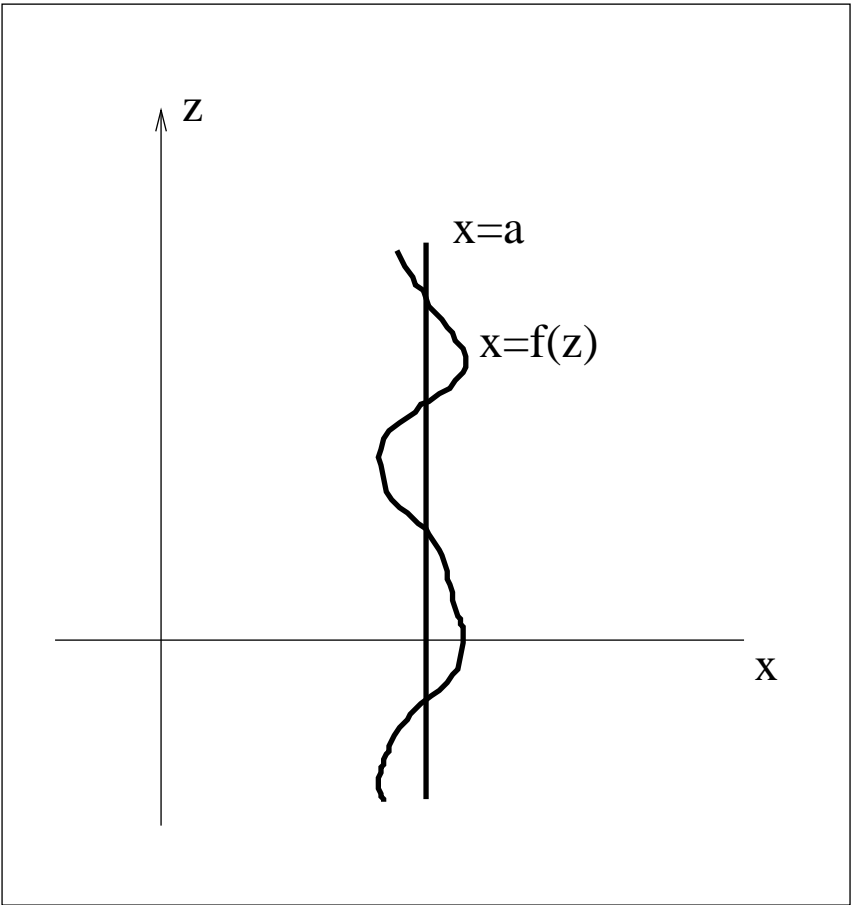


Figure 2.3: A rough wall near  $x = a$

We now examine the deviation of the complex dielectric constant of the rough waveguide from the smooth case. Near the boundary  $x = a$  this deviation is given by

$$\epsilon_r(x, z) - \epsilon_s(x, z) = \Delta\epsilon(x, z) = \begin{cases} 0 & \begin{cases} x < a & a < f(z) \\ x < f(z) & f(z) < a \end{cases} \\ 1 - \epsilon & a < x < f(z) \quad a < f(z) \\ -(1 - \epsilon) & f(z) < x < a \quad f(z) < a \\ 0 & \begin{cases} x > f(z) & f(z) > a \\ x > a & a > f(z) \end{cases} \end{cases} \quad (2.42)$$

where  $\epsilon_r(x, z)$  stands for the relative dielectric constant of the rough waveguide and  $\epsilon_s(x, z)$  is defined in (2.1). The deviation near  $x = -a$  is expressed in a similar manner, in terms of  $h(z)$ .

The following analysis applies to the TE modes; the TM analysis is very similar, where the magnetic field  $H_y$  replaces the electric field  $E_y$ .

The TE fields in the waveguide are solutions of the wave equation:

$$\frac{\partial^2 E_y}{\partial x^2} + \frac{\partial^2 E_y}{\partial z^2} + (\epsilon_s(x, z) + \Delta\epsilon(x, z)) \epsilon_0 k^2 E_y = 0 \quad (2.43)$$

The modes of the smooth waveguide are solutions of

$$\frac{\partial^2 E_y}{\partial x^2} + \frac{\partial^2 E_y}{\partial z^2} + \epsilon_s(x, z) \epsilon_0 k^2 E_y = 0 \quad (2.44)$$

We express the field  $E_y$  in the perturbed waveguide in terms of the modal fields  $E_{yn}$  of the smooth waveguide:

$$E_y = \sum_{n=1}^M C_n(z) E_{yn} \quad (2.45)$$

where  $C_n(z)$  are complex modal coefficients. The summation in (2.45) is taken over all the symmetric and antisymmetric TE modes. When we insert this expansion in equation (2.43), we obtain an equation in terms of the modal coefficients  $C_n(z)$ :

$$\sum_n \frac{\partial^2 C_n(z)}{\partial z^2} E_{yn} + 2 \sum_n (-j\beta_n) \frac{\partial C_n(z)}{\partial z} E_{yn} + \Delta\epsilon(x, z) \epsilon_0 k^2 \sum_n C_n(z) E_{yn} = 0 \quad (2.46)$$

We multiply this equation by the expression of the field of a specific mode,  $E_{ym}$ , and integrate from  $x = -a$  to  $x = a$ . The orthogonality of the modes of the smooth waveguide is very useful at this stage because it removes most of the terms in the integral, and we are left with a differential equation for the coefficient of the  $m^{\text{th}}$  mode:

$$\frac{\partial^2 C_m}{\partial z^2} - 2j\beta_m \frac{\partial C_m}{\partial z} = F_m(z) \quad (2.47)$$

where  $F_m(z)$  is given by:

$$F_m(z) = -\frac{\epsilon_0 k^2}{I_m} \int_{-a}^a \Delta\epsilon(x, z) \sum_n C_n(z) E_{yn} E_{ym}^* dx \quad (2.48)$$

$I_m = \int_{-a}^a |E_{ym}|^2 dx = 2w\mu_0 P / \beta_m$  and  $P$  is defined in (2.33).

We calculate below the coupling between the first mode and all the other modes in terms of coupling coefficients, where each coupling coefficients describes the coupling between two of the propagating modes. This result is later extended to derive the coupling coefficient between any two modes. The 1<sup>st</sup> mode is not particularly different from the other modes, we choose to use it for the calculation of the coupling coefficient for the ease of notation.

In order to calculate the coupling coefficients between the 1<sup>st</sup> mode and the other modes, we assume that the 1<sup>st</sup> mode is excited at  $z = 0$  and calculate the amplitudes of the other modes at a point  $z$  (namely  $C_m(z)$ ). The excitation is expressed by:

$$C_m(0) = \begin{cases} 1 & m = 1 \\ 0 & m > 1 \end{cases} \quad (2.49)$$

We assume that coupling is low, which means either that  $z$  is close enough to zero or that coupling is so small that second order coupling is negligible. This assumption may not always be realistic, especially in cases of large wall roughness. However, this assumption renders a simple linear theory (equation 2.77) that may be considered a first order approximation of the actual coupling process. Thus, we consider only the coupling of power from the 1<sup>st</sup> mode into other modes, and disregard coupling among the higher order modes. We also neglect the coupling from any mode into the 1<sup>st</sup> mode.

The solution of (2.47) is:

$$C_m(z) = A_m + B_m e^{2j\beta_m z} + \frac{1}{2j\beta_m} \int_0^z [e^{2j\beta_m(z-\zeta)} - 1] F_m(\zeta) d\zeta \quad (2.50)$$

The coupling coefficient (2.50) contains forward traveling (toward  $+z$ ) and backward traveling waves:

$$C_m = C_m^{(+)} + C_m^{(-)} \quad (2.51)$$

where the forward traveling part is

$$C_m^{(+)}(z) = A_m - \frac{1}{2j\beta_m} \int_0^z F_m(\zeta) d\zeta \quad (2.52)$$

and the backward part is

$$C_m^{(-)}(z) = \left\{ B_m + \frac{1}{2j\beta_m} \int_0^z e^{-2j\beta_m\zeta} F_m(\zeta) d\zeta \right\} e^{2j\beta_m z} \quad (2.53)$$

Using the low coupling assumption described above, we disregard the backward traveling waves for  $z > 0$  and use the approximation  $C_m(z) \approx C_m^{(+)}(z)$ . After applying the initial conditions (2.49), the coupling coefficients are then given by

$$C_m(z) = -\frac{1}{2j\beta_m} \int_0^z F_m(\zeta) d\zeta \quad m > 1 \quad (2.54)$$

Using the low coupling assumption and a small geometrical perturbation assumption, we calculate  $F_m(z)$  from (2.48):

$$\begin{aligned} F_m(z) &\approx -\frac{\beta_m k^2}{2\omega\mu_0 P} (1 - \epsilon) \\ &\quad \times [(f(z) - a) E_1(a, z) E_m^*(a, z) \\ &\quad - (h(z) + a) E_1(-a, z) E_m^*(-a, z)] \end{aligned} \quad (2.55)$$

Using the field expressions from (2.4) we calculate:

$$\begin{aligned} E_1(a, z) E_m^*(a, z) &= E_1(-a, z) E_m^*(-a, z) \\ &\approx \frac{(ka)^2}{u'_1 u'_m} Z_0^2 \mathcal{H}_1 \mathcal{H}_m T_1(u'_1) T_m(u'_m) e^{-j(\beta_1 - \beta_m)z} \end{aligned} \quad (2.56)$$

where

$$T_n(v) = \begin{cases} \cos(v) & n \text{ odd, TE symmetric} \\ \sin(v) & n \text{ even, TE antisymmetric} \end{cases} \quad (2.57)$$

Rearranging  $F_m(z)$  we have

$$F_m(z) \approx (\epsilon - 1) \frac{k^2 \beta_m}{a} \frac{T_1(u'_1)}{\sqrt{\beta'_1}} \frac{T_m(u'_m)}{\sqrt{\beta'_m}} [f(z) - a - h(z) - a] e^{-j(\beta_1 - \beta_m)z} \quad (2.58)$$

Now we calculate the integral in (2.52):

$$\int_0^z F_m(\zeta) d\zeta \approx (\epsilon - 1) \frac{k^2 \beta_m z}{a} \frac{T_1(u'_1)}{\sqrt{\beta'_1}} \frac{T_m(u'_m)}{\sqrt{\beta'_m}} (\phi_m^* - \psi_m^*) \quad (2.59)$$

where

$$\phi_m = \frac{1}{z} \int_0^z (f(\zeta) - a) e^{-j(\beta_1 - \beta_m)\zeta} d\zeta \quad (2.60)$$

$$\psi_m = \frac{1}{z} \int_0^z (h(\zeta) + a) e^{-j(\beta_1 - \beta_m)\zeta} d\zeta \quad (2.61)$$

$\phi_m$  and  $\psi_m$  are the Fourier coefficients of the functions  $f(z) - a$  and  $h(z) + a$  calculated at the spatial frequency  $\beta_1 - \beta_m$  (the difference of frequencies between the two coupled modes  $E_1$  and  $E_m$ ). The coupling between the two modes is related to a particular Fourier component of the geometry of the walls, which corresponds to the spatial frequency difference between the modes. This is a well known result of electromagnetic scattering theory [73, 66].

The modal coefficients are calculated using (2.59) in (2.54):

$$C_m(z) = -(\epsilon - 1) \frac{k^2 z}{2ja} \frac{T_1(u'_1)}{\sqrt{\beta'_1}} \frac{T_m(u'_m)}{\sqrt{\beta'_m}} (\phi_m^* - \psi_m^*) \quad (2.62)$$

$m > 1$

## 2.2.1 The Coupled Power Equations

The coupling coefficients of the modes contain amplitude and phase information, but the quantity of interest in the analysis of cellular systems is often the power. Another reason to calculate the coupling among the modes in terms of their power and not their

amplitude is that the power coupling coefficients can be calculated in an average manner, as we show below, whereas the amplitude coupling coefficients contain a phase factor that is very hard to analyze in an average manner. The modal amplitudes  $C_n$  contain too much information for our needs; The power exchange among the modes is best expressed in terms of power equations.

We now proceed to derive the coupled power equations of the modes of the rough waveguide following *Marcuse* [58]. The derivation is based on the above calculation of the complex amplitudes of the waveguide modes.

The coupling coefficients of the modes affect the mode amplitudes through the wave equation

$$\frac{\partial A_m}{\partial z} = \sum_{n=1}^M c_{mn} A_n \quad (2.63)$$

where  $\{A_n\}$  represent the complex mode amplitudes (phasor) and  $c_{mn}$  is the coupling coefficient from the  $n^{\text{th}}$  mode to the  $m^{\text{th}}$ .  $c_{nn}$  represents the propagation constants of the  $n^{\text{th}}$  mode, so  $c_{nn} = -j\beta_n$ . We represent the  $z$  dependence of the modes explicitly as

$$A_n(x, z) = C_n(z) B_n(x) e^{-j\beta_n z} \quad (2.64)$$

where  $B_n(x)$  contains the  $x$  dependence of the  $n^{\text{th}}$  mode. The coupled equations in terms of the new notation are:

$$\frac{\partial C_m}{\partial z} B_m(x) = \sum_{\substack{n=1 \\ n \neq m}}^M c_{mn} C_n(z) B_n(x) e^{j(\beta_m - \beta_n)z} \quad (2.65)$$

In order to calculate the coupling coefficients  $c_{mn}$ , we solve (2.65), with the initial conditions defined in (2.49): at  $z = 0$  only the 1<sup>st</sup> mode is excited. Using a first order perturbation solution we obtain:

$$C_m(z) \approx \begin{cases} 1 & m = 1 \\ c_{m1} z e^{j(\beta_m - \beta_1)z} & m > 1 \end{cases} \quad (2.66)$$

A comparison of (2.66) with (2.62) gives the coupling coefficient from the 1<sup>st</sup> mode to

the  $m^{\text{th}}$ :

$$c_{m1} = -(\epsilon - 1) \frac{k^2}{2ja} \frac{T_1(u'_1)}{\sqrt{\beta'_1}} \frac{T_m(u'_m)}{\sqrt{\beta'_m}} [f(z) - a - h(z) - a] \quad (2.67)$$

We extend this result and write that the coupling from the  $n^{\text{th}}$  mode to the  $m^{\text{th}}$  is described by:

$$c_{mn} = -(\epsilon - 1) \frac{k^2}{2ja} \frac{T_n(u'_n)}{\sqrt{\beta'_n}} \frac{T_m(u'_m)}{\sqrt{\beta'_m}} [f(z) - a - h(z) - a] \quad (2.68)$$

The coupling coefficients are reciprocal, i.e.

$$c_{mn} = -c_{nm}^* \quad (2.69)$$

The reciprocity can be shown by considering the conservation of power of the coupling process (for details see *Marcuse* [58]).

A further extension of the calculation of the coupling coefficients applies the result to the TM modes. We present a new indexing method which is used in the remainder of the thesis. The TE modes are numbered  $1, \dots, M$  and the TM modes are numbered  $M + 1, \dots, N$ , where  $N = 2M$ . When using the propagation constants  $u_n$  and  $\beta_n$  for  $n > M$ , we apply the appropriate formulas (2.22), (2.23) and (2.28) with  $n - M$ .

The waveguide model presented in this section does not introduce coupling between TE and TM modes. However, a more realistic model that allows for variations in the  $y$  direction does introduce such coupling. We now include TE–TM coupling in our model and assume that the coupling coefficients are given by (2.68) with:

$$T_n(v) = \begin{cases} \cos(v) & 1 \leq n \leq M & n \text{ odd,} & \text{TE symmetric} \\ \sin(v) & 1 \leq n \leq M & n \text{ even,} & \text{TE antisymmetric} \\ \sin(v) & M + 1 \leq n \leq N & (n - M) \text{ even,} & \text{TM symmetric} \\ \cos(v) & M + 1 \leq n \leq N & (n - M) \text{ odd,} & \text{TM antisymmetric} \end{cases} \quad (2.70)$$

The coupled wave equations (2.63) are translated into a system of coupled power equations using *Marcuse's* theory [58]. The average power carried by the  $n^{\text{th}}$  mode is  $P_n = \langle |A_n|^2 \rangle = \langle |C_n|^2 \rangle$ , where the brackets  $\langle \cdot \rangle$  indicate an ensemble average over

many waveguides with (statistically) similar wall perturbations. An important assumption in the development of this theory is that the coupling coefficients are of the form

$$c_{mn} = K_{mn}\gamma(z) \quad (2.71)$$

where  $\gamma(z)$  has the following correlation properties:

$$\langle \gamma(z)\gamma(z - z_0) \rangle = \sigma_\gamma^2 e^{-(|z_0|/D_\gamma)^2} \quad (2.72)$$

The coupled power equations are [58]:

$$\frac{dP_m}{dz} = \alpha_m P_m + \sqrt{\pi}\sigma_\gamma^2 D_\gamma \sum_{n=1}^{2N} |K_{mn}|^2 e^{-[(\beta_m - \beta_n)D_\gamma/2]^2} (P_n - P_m) \quad (2.73)$$

where  $\alpha_m$  represent the modal loss factors. Natural choices for the loss factors are the modal loss factors  $\alpha_m = 2\beta_m''$  calculated in (2.27) and (2.28), where the multiplication by 2 is necessary because  $\beta_m$  are the amplitude loss factors and  $\alpha_m$  are the power loss factors. We use the coupling coefficients calculated in (2.68), and recognize that

$$K_{mn} = -(\epsilon - 1) \frac{k^2}{2ja} \frac{T_n(u'_n)}{\sqrt{\beta'_n}} \frac{T_m(u'_m)}{\sqrt{\beta'_m}} \quad (2.74)$$

and  $\gamma(z) = f(z) - h(z) - 2a$ . Using (2.41) we calculate the correlation of  $\gamma(z)$  as

$$\sigma_\gamma = \sqrt{2}s \quad (2.75)$$

$$D_\gamma = D \quad (2.76)$$

The coupled power equations for the rough waveguide now become

$$\frac{dP_m}{dz} = \alpha_m P_m + \sqrt{\pi}2s^2 D \sum_{n=1}^N |K_{mn}|^2 e^{-[(\beta_m - \beta_n)D/2]^2} (P_n - P_m) \quad (2.77)$$

The coupled power equations (2.77) constitute an approximation to the description of a waveguide with weak mode coupling and small loss. The linear coupling model is a first order approximation; it relies on the assumption of slow coupling among the propagating modes [56], which is justified in the case of small perturbations in the geometry

of the waveguide. This theory may be considered a first order approximation of the behavior of the waveguide that is very useful in understanding the principal propagation phenomena in it.

The coupled power equations (2.77) can be expressed as a simple matrix equation, where the unknown is a vector containing the power level of each mode:

$$\bar{P} = \begin{pmatrix} P_1 \\ \vdots \\ P_N \end{pmatrix} \quad (2.78)$$

and the coupled power equation takes the form:

$$\frac{\partial \bar{P}}{\partial z} = \Gamma \bar{P} \quad (2.79)$$

where  $\Gamma$  is an  $N \times N$  matrix which holds all the power coupling coefficients. The  $mn^{\text{th}}$  location holds

$$\Gamma_{mn} = \sqrt{\pi} 2s^2 D |K_{mn}|^2 e^{-[(\beta_m - \beta_n)D/2]^2} \quad (2.80)$$

and the diagonal elements hold the sum of the coupling coefficients and the loss of each mode

$$\Gamma_{mm} = \alpha_m - \sqrt{\pi} 2s^2 D \sum_{\substack{n=1 \\ n \neq m}}^N |K_{mn}|^2 e^{-[D/2(\beta_m - \beta_n)]^2} \quad (2.81)$$

## 2.2.2 Solution to the Coupled Power Equation

The coupled power equation (2.77) is easily solved in terms of the eigenvalues and eigenvectors of the coupling matrix  $\Gamma$ :

$$\bar{P} = \sum_{n=1}^N \bar{B}_n e^{\lambda_n z} \quad (2.82)$$

where  $\bar{B}_n$  are the eigenvectors of  $\Gamma$  and  $\lambda_n$  are the corresponding eigenvalues. We note that all the eigenvalues of  $\Gamma$  are real and negative, because of its special form. In order to investigate the steady state behavior of the solution, we are interested in  $\lambda_1$ , the first (smallest in absolute value) eigenvalue of  $\Gamma$ , that describes the slowest decrease in power

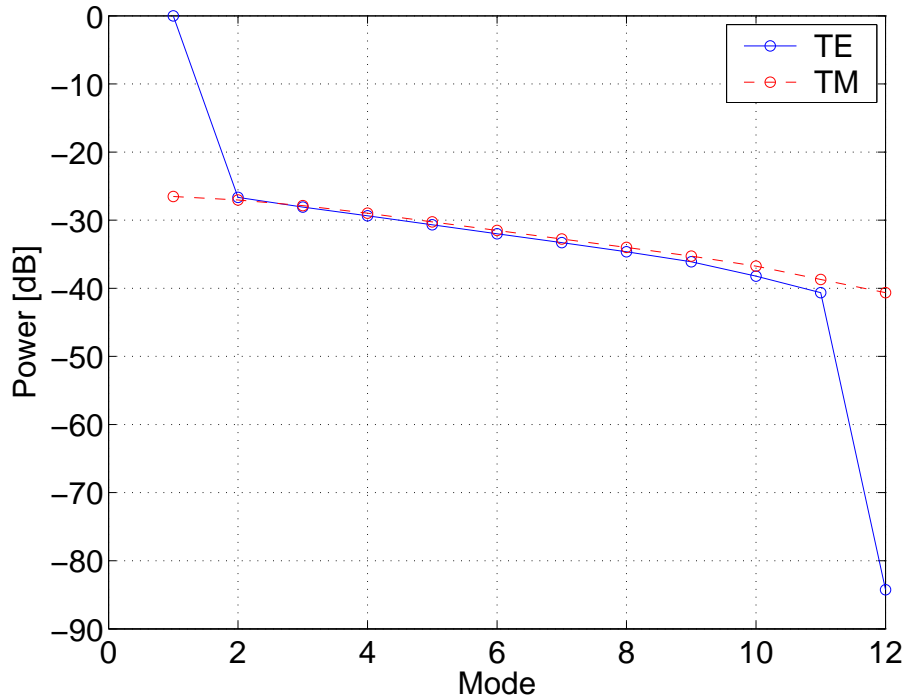


Figure 2.4: A steady state distribution of power over modes. The horizontal axis is the mode number and the vertical axis is power on a logarithmic scale.

level at increasing distance from a source.

$$\bar{P} = \bar{B}_1 e^{\lambda_1 z} \quad (2.83)$$

Equation (2.83) describes the solution of (2.77) at large distances from the source, where the fast decaying exponentials (all except  $e^{\lambda_1 z}$ ) are very low.

The steady state solution (2.83) varies with distance along the waveguide, but only via the exponential decay. After reaching steady state the distribution of the power among the modes does not change along the waveguide. The steady state solution tends to concentrate most of the power in the low order modes, because the high order modes have higher losses. A typical example of a steady state power distribution is shown in Figure 2.4. This example is calculated for the parameters of an indoor hallway presented in Chapter 3 for the Packard Building hallways (hallways 1.8 m wide, walls with  $\epsilon = 3$ ,  $\sigma = 0.075$  S/m,  $D = 2$  m<sup>2</sup> and  $s^2 = 0.2$  m<sup>2</sup>). The TE mode of the 12th order is very

weak in this example because it is close to cutoff, so its losses are very high.

In addition to our interest in the steady state solution, we also looked at the dynamic behavior of the power measured at small distances from a source. We model the source as a distribution of power among the waveguide modes, and then solve (2.79) numerically. The results we present in Chapters 3 and 4 are the total power along the waveguide calculated as numerical solutions of equation (2.79).

### 2.2.3 The TEM mode

The lowest order TM mode is the transverse electromagnetic (TEM) mode, which has both its electric and magnetic fields in the  $x$ - $y$  plane and no field components in the  $z$  direction. The magnetic field is in the  $y$  direction and the electric field is in the  $x$  directions and both fields are fixed across the waveguide.

The TEM mode is present in a slab (two dimensional) waveguide, but it does not exist if the waveguide has a third dimension — a floor or a ceiling. The reason is the high tangential electric field near the floor/ceiling. The TEM mode was not included in the development in this chapter or in the calculations presented in Chapters 3 — 6. Thus the simulated waveguide is similar to the waveguides induced by real environments, with a floor and ceiling (or a ground for the outdoor case).

### 2.2.4 Penetration into Sidewalls

The penetration of an incident plane wave into a thick wall made of uniform material and with a planar interface [83] is given by

$$T_{TE} = \begin{cases} \left[ \frac{2Z_2 \cos(\theta_1)}{Z_2 \cos(\theta_1) + Z_0 \cos(\theta_2)} \right]^2 \frac{Z_0}{Z_2} & \sin(\theta_2) \leq 1 \\ 0 & \sin(\theta_2) > 1 \end{cases} \quad (2.84)$$

for the power of the TE modes, and

$$T_{TM} = \begin{cases} \left[ \frac{2Z_2 \cos(\theta_2)}{Z_2 \cos(\theta_2) + Z_0 \cos(\theta_1)} \right]^2 \frac{Z_0}{Z_2} & \sin(\theta_2) \leq 1 \\ 0 & \sin(\theta_2) > 1 \end{cases} \quad (2.85)$$

for the TM modes, where  $\theta_1$  and  $\theta_2$  are the incident and refraction angles, measured from the normal to the wall and  $Z_2 = \sqrt{\mu_0/\epsilon_0\epsilon}$ . The refraction angle is calculated using Snell's Law:

$$\sin(\theta_2) = \sqrt{\epsilon'} \sin(\theta_1) \quad (2.86)$$

and total reflection takes place whenever  $\sin(\theta_2) > 1$ .

This penetration analysis assumes a very simple wall structure: an infinitely thick wall. See [39] for a more detailed theoretical treatment of reflection off drywall.

## 2.3 A Three Dimensional Waveguide

The introduction of a third spatial dimension into our waveguide model creates considerable complications, so we take here an approximate approach to the effects of the floor and ceiling on the hallway propagation, and the ground on the street propagation.

The floor and ceiling of a hallway are modeled as smooth surfaces made of very good conductors. Thus, their effects can be considered separately from the effects of the walls. We note that in many modern office buildings, the floors are made of concrete poured over metal trays, so they are highly reflective.

The hallway can be seen as an intersection between two slab waveguides, one with smooth conducting boundaries (the floor and ceiling) and the other with rough, lossy dielectric boundaries (the walls of the hallway). The effects of these two waveguides can be separated, where the floor–ceiling guide determines the  $y$  dependence of the field components and the wall guide determines the  $x$  dependence. Using this coordinate separation model, there is only a minor effect of the floor and ceiling on the behavior of the fields and the coupling among the modes. The results we will show in Chapter 3 are calculated with the two dimensional model.

Considering an outdoor street, the ground is modeled as a smooth surface made of very good dielectric reflector, with reflection coefficient  $\rho=-1$  for the electric field [38]. The ground plane affects each of the propagating modes differently, because the wave vectors of the modes point in different directions.

The coupling between the modes reduces the coherency between the direct propagating wave (of a certain mode) and its reflections off the ground. We consider the effect

of incoherent addition of the direct and reflected waves for each mode, so we sum the power of these waves. For each mode we use the loss rate  $\alpha_n$  and multiply the power of the mode by  $1 - e^{-2\alpha_n \Delta d}$ , where  $\Delta d$  is the difference of the lengths of the direct and ground reflected paths.

When looking at a street corner (Section 2.4), we consider the junction as an initialization reference for propagation down the side street. Therefore, we calculate the reflection effects from the junction instead of the location of the actual transmitter antenna, and  $\Delta d$  is measured from the junction.

## 2.4 Junctions in the Waveguide

This section describes the model of waveguide junctions, where power flows along one waveguide ('main') into another ('side') waveguide. We are interested in the behavior of power levels along the side waveguide. We present here an intuitive explanation of the mode coupling mechanism, for a more thorough analysis see [7, 52, 74].

In order to look at the coupling mechanism in some detail, we consider the plane wave decomposition of the modes. Each mode can be decomposed into a pair of plane waves propagating at equally oblique angles with the  $z$  direction. The lower order modes are decomposed into plane waves that propagate in an almost parallel direction to the  $z$  axis. High order modes travel in directions increasingly oblique to the  $z$  axis. When considering a perpendicular waveguide corner, the low order modes in the main waveguide couple into high order modes in the side waveguide (Figure 2.5). Similarly, high order modes in the main waveguide couple into low order modes in the side waveguide.

The analysis is further complicated when we take into account the coupling efficiency of the different modes. The low order modes radiate only a small part of their power into the side waveguide, because of the direction of the wave vector. On the other hand, the high order modes radiate into the side waveguide a greater part of their power. The variation in coupling efficiency tends to equalize the distribution of power at the side waveguide, because the stronger (low order) modes couple with low efficiency than the weaker (high order) modes.

Consider a steady state distribution of power of the modes in the main waveguide,

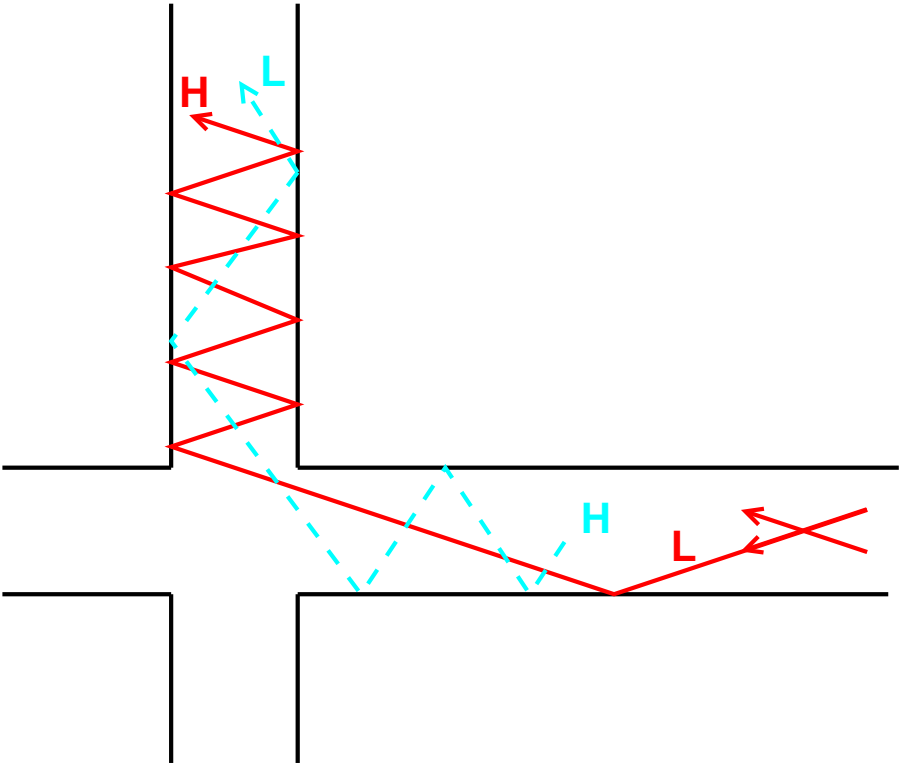


Figure 2.5: A waveguide junction model. The solid line represents a low order mode of the main waveguide coupled into a high order mode of the side waveguide. The dashed line represents a high order mode of the main waveguide coupled into a low order mode of the side waveguide.

where most of the power is contained in the low order modes. The power leaking into the side waveguide is re-distributed among the modes as it propagates along the waveguide.

Measurements shown in [12, 27, 29, 30, 35, 40, 53, 75] for outdoor environments demonstrate the sharp decrease of power levels in the side street in the vicinity of the junction. The overall decrease in power level in side streets, near a junction with a main street, can be related to the distribution of power among the modes in the main streets. Near the transmitter, power is distributed more or less uniformly among the modes in the main street, so an intersecting side street there accepts an approximately flat distribution of power among the modes at the intersection. The re-distribution of power among the modes that occurs along the side street causes a moderate decrease of power level.

If we consider another side street, intersecting with the main street at a larger distance from the transmitter, the theory predicts that the power distribution near a junction at this side street will be biased toward the high order modes, because the distribution in the main street tends to concentrate power in the low order modes. The result is that in the further side street (from the transmitter), the overall power decrease in the area of the junction is larger.

Looking at a series of side streets at increasing distances from the transmitter, we therefore expect that the side streets closest to the transmitter will incur a small decrease of power level in the region of the junction. At further side streets the amount of power loss increases, until a steady state is reached. Measurements showing a similar behavior are reported in figure 13 of [27].

The expected effect in the side waveguide is a significant decrease of power level as the receiver moves away from the junction. At some distance, where the modal distribution of power reaches its steady state, the rate of decrease of power loss along the waveguide resumes its steady state rate.

The model assumes solid walls, so it doesn't present leakage between the waveguides through the rooms (for the hallway case) or buildings (for the street case). This leakage may be significant if propagation through the walls is low loss.

Observations of measured power levels in Chapters 3 and 4 show that a uniform distribution of power over the modes is a realistic and useful initial condition for propagation in the side waveguide both in the indoor (hallway) and outdoor (street) cases. This initial condition was used in the calculations shown later.

## 2.5 Summary of the Model

This chapter presented the model of hallways and streets as multimoded lossy waveguides. The analysis began with an ideal waveguide with smooth lossy walls and then followed with a waveguide with rough walls, that induce mode coupling. The coupling was described in terms of the power coupling equation (2.77), that was solved in Section 2.2.2. The steady state solution (2.83) is attained at large distances from the source and major disturbances in the waveguide.

The floor and ceiling of a hallway were modeled as smooth conducting surfaces in Section 2.3, so their effect can be separated from the effects of the walls. The ground surface of a street was modeled as a very good reflector, and the reflected path is incoherently added to the direct path. An intersection of two waveguides, where power flows from one waveguide into another, constitutes an initial condition for the propagation in the second waveguide. This initial condition was discussed in Section 2.4.

The rest of this thesis presents different usages of the waveguide model. Chapter 3 describes the prediction of power levels in hallways of large buildings and shows measurements from two buildings. Chapter 4 discusses the prediction of power levels in an urban environment, and contains measurements from two cities. Chapter 5 discusses the delay profile and Chapter 6 brings a calculation of the capacity of a multiple antenna system, where both the transmitter and the receiver are located in a hallway.

# Chapter 3

## Indoor Power Measurements

This chapter describes power measurements from two buildings. Section 3.1 contains measurements taken in Stanford in 2001–2, and compares the results to the waveguide theory from the previous chapter. The measurements were taken in the basement of the Packard building, in the 850–950 MHz band. The attenuation of the radio channel was measured with a 250 kHz resolution, to an accuracy of  $\pm 1$  dB.

Section 3.2 contains measurements taken by Bell Core in the Bell Lab Crawford Hill Laboratory Building, in the main hallway of the first floor.

### 3.1 Stanford Measurements

#### 3.1.1 The Measurement Setup

The setup consisted of two carts holding equipment that were placed in the hallways (and sometimes in the rooms). The carts were made of polyethylene. One cart held the transmitting antenna and the other the receiving antenna and other equipment (Figures 3.1 and 3.2). The receiving equipment was connected to electric power via a long cable.

#### Antennas

The antennas were quarter-wave monopoles on a magnetic mount, with a ground plane. Metal boxes (31.5 cm  $\times$  32.9 cm  $\times$  15 cm) were used for the ground planes, with each

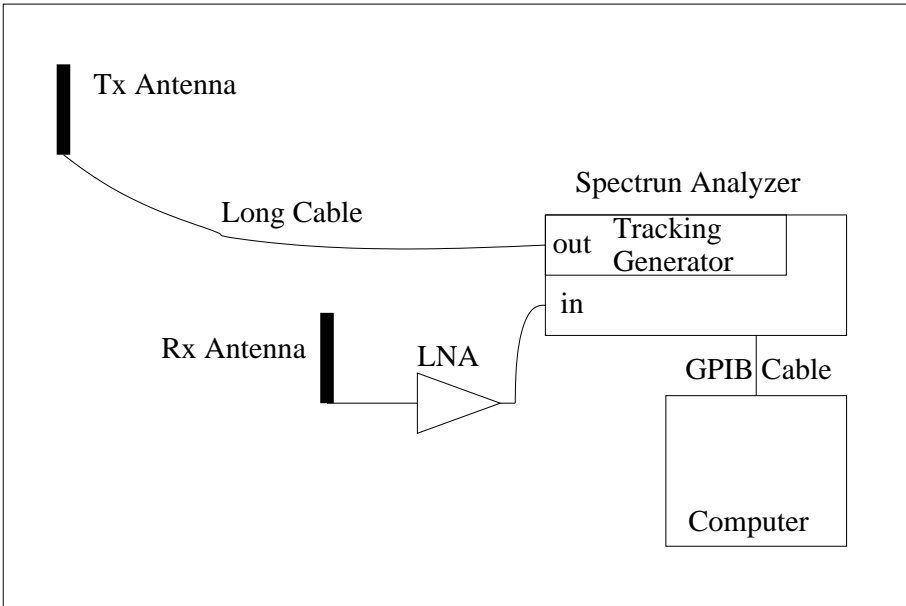


Figure 3.1: The Measurement Setup



Figure 3.2: The Receiver Cart

antenna at the center of the large face of a box. The ground planes were about 15 cm above the top of the cart, and 100 cm above ground. The antennas were made by Antenna Specialists, the model of one is ASP-1890T. They were very similar, with a difference of about 2 mm in length. The SWR of both antennas in the measurement band is below 1.55, with the maximum around 934 MHz. A comparative measurement was done by using a third transmitting antenna, and measuring with the two Antenna Specialist antennas in the receiving side. This measurement shows only insignificant differences between the two antennas, smaller than the variations caused by changes in the environment, over a period of a few minutes during which measurements were taken.

### **Cable**

A long cable connected the tracking generator output and the transmitting antenna. The cable was LMR-400 coaxial cable, made by Times Microwave Systems (model number 68999). The characteristic impedance of the cable was 50 ohm. The average cable attenuation over the band was 9.4 dB.

### **LNA**

The LNA was made by Mini-Circuits, model number ZFL-1000LN. This was a 50 ohm LNA with a 20 dB gain and noise figure of 2.9 dB.

### **Spectrum Analyzer**

The spectrum analyzer was HP8595E with the tracking generator (option 010) and the transmitter power was set at the maximum level of 2.75 dBm.

### **Computer**

The computer was used to record the received signal power from the spectrum analyzer via a GPIB cable. A computer program polled the spectrum analyzer for the received data and various parameters. The computer recorded each measurement in a text file. Together with data received from the spectrum analyzer, the output file contained information about the location of the transmitting and receiving antennas. See details of the

file format in Appendix A.

### 3.1.2 Environment

Experimental measurements were carried out in the Packard Building, which is an office and laboratory building on the Stanford campus built around 1999. The ceiling was made of insulating blocks laid on light aluminum frames, with metal plates between the top of the basement and the ground floor of the building. The interior walls were mostly drywall, 5/8" thick on each side, with aluminum studs 2" × 4", at 16" separations. The floor and some walls were made of reinforced concrete.

#### Measurement Locations

Measurements were taken in the hallways and rooms of the basement of the Packard Building. Most of the measurements were taken with the transmitter at one location and the receiver moving in the building. Figure 3.3 shows the location of the transmitter and the receiver locations for the relevant measurements with the median power level at each receiver location. The location was usually measured accurately (within 10 cm) in the hallways, but the locations in the room have lower accuracy because of the difficulty of relating precise location measurements in the rooms to those done in the hallways, and because of accumulated errors when moving the cart far from the walls. As a result, some measurements appear in Figure 3.3 to be on the walls.

### 3.1.3 Measurement Results

This section shows median power levels measured along the hallways and in adjacent rooms. The median power level over the band (850–950 MHz) is shown for each measurement location. The median was taken over the received power levels in dBm. Taking the median over the frequency band has a similar effect as taking a median over single frequency measurements over a small (spatial) neighborhood [16]. The median was used instead of a mean in order to reduce the effects of deep fades and interference over the result. For most measurements, the median is close to the mean (taken over frequency), specifically, the median is between mean-0.5 dB and mean+1.5 dB in 92% of the measurements. The sensitivity limit of the measurements is around -90 dB, where

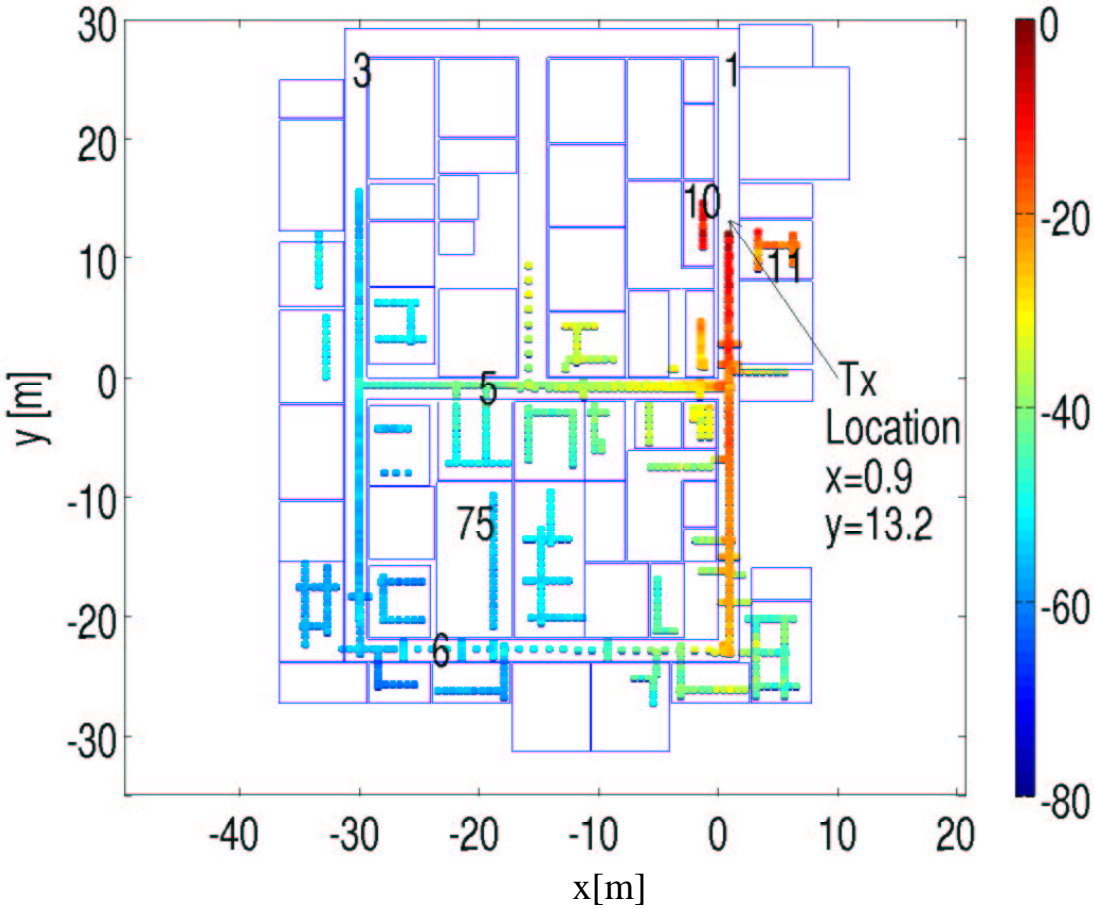


Figure 3.3: Locations of the transmitter and receiver in the Packard basement, with median power level at each receiver location [dBm]. The single digit numbers indicate hallways and the two-digit numbers indicate rooms in the building. The lines indicate the inner boundary of the hallway and room walls. Details of the walls and doors were omitted.

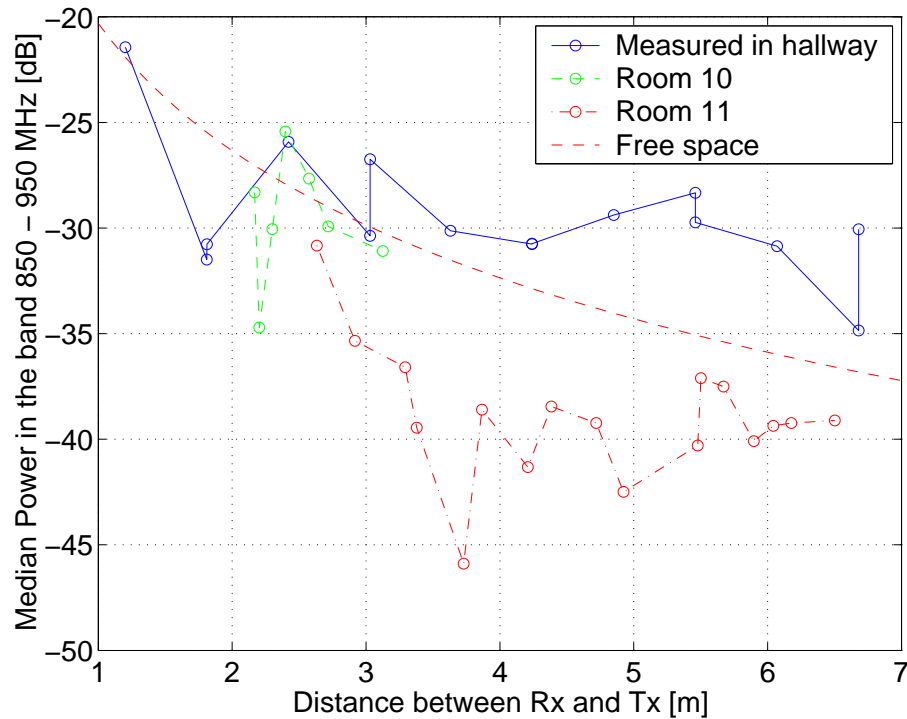


Figure 3.4: Power received near the transmitter, the geometry is shown in Figure 3.3. The free space curve is an estimation based on measurements at close range.

the limitation is leakage from the connector of the cable linking the generator to the transmitting antenna.

### Wall Penetration

Figure 3.4 shows the power received near the transmitter in the hallway and in two adjacent rooms, with the geometry shown in Figure 3.3. The measurements in room 11 show considerably lower power because a concrete wall separates this room from the hallway. In room 10, power levels are very similar to the hallway level. The difference is within the accuracy of our measurements, which is limited by temporal variations and the inaccuracy of the equipment. A reliable estimate of the drywall attenuation cannot be obtained from our measurements, except to say that the penetration is very good. Measurements in [77] and [39] show attenuation of 0.1–0.5 dB for perpendicular incidence on drywall boards of various widths.

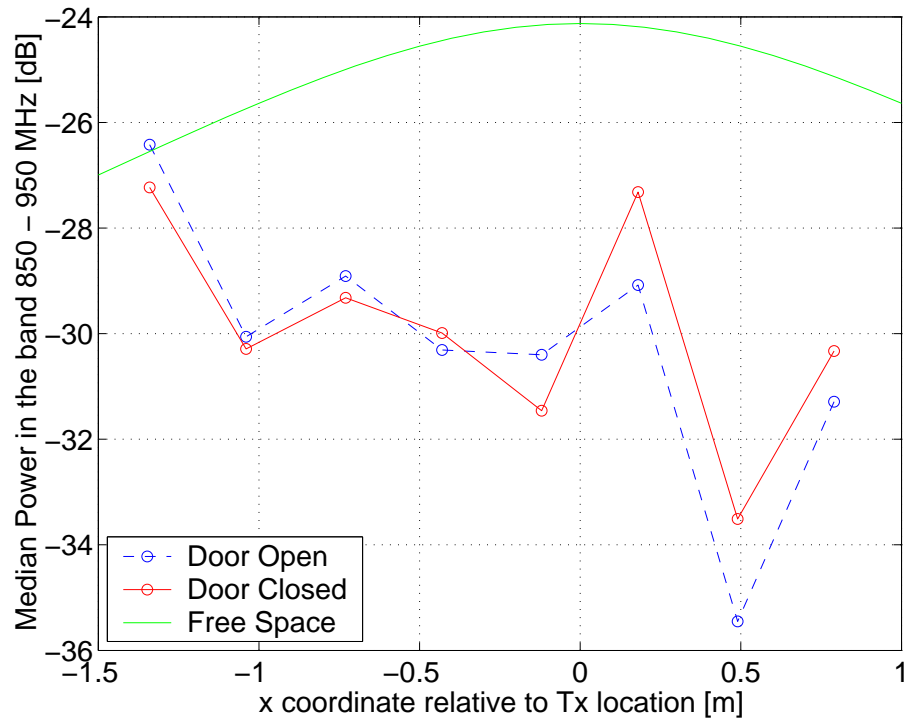


Figure 3.5: Power received along a wall, the geometry is shown in Figure 3.6. The free space curve is an estimation based on measurements at close range.

Another indication of the penetration through drywall is shown in Figure 3.5, that presents the power measured along the wall of room 75, with the door open and closed. The geometry of this measurement is shown in Figure 3.6. The state of the door (open or closed) has little effect on the power levels. This indicates that most of the radiation penetrates directly through the wall. Although penetration through the walls is strong, the measurements shown in Section 3.1.3 indicate that the main propagation mechanism near the hallways is guidance of the radiation.

### Power in the Hallways and Adjacent Rooms

Figure 3.7 shows the power measured in Hallway 1 (solid line) and the power measured in the adjacent rooms at distances up to 5 m from the hallway. Hallway 1 contains the transmitter so that the locations in the hallway, which have line of sight to the transmitter, receive more power than locations in the rooms.

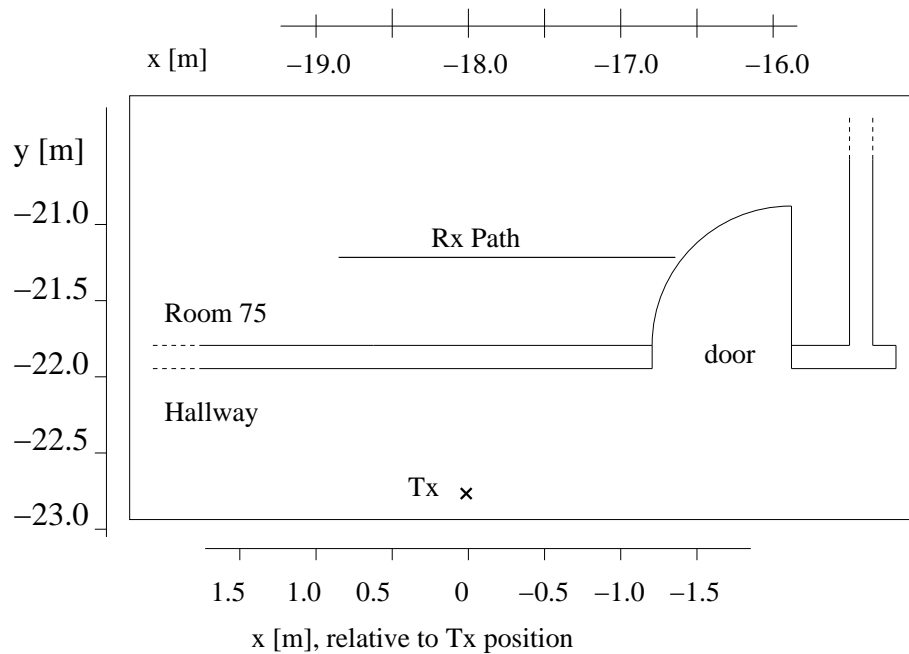


Figure 3.6: Geometry of the measurements near room 75.

One phenomenon seen in Hallway 1 is the increasing difference between the hallway power levels and the room power levels at increasing distances from the transmitter. At locations close to the transmitter, the difference between the power levels is small (0 dB for the negative  $x$  and about 10 dB for the positive  $x$ ). The walls in the positive  $x$  side are concrete in this area. At large distances from the transmitter, the difference between the hallway and the room levels is on the order of 15–20 dB for both sides.

The power levels in the hallway appear to be affected by the junction with Hallway 5 that is located between  $y=0$  m and  $y=-1.8$  m. Power levels *increase* from about  $y=-2$  m to  $y=-6$  m as the receiver moves away from the transmitter in Hallway 1 past the junction, and continue to decrease at larger (more negative) distances. Similar phenomena were measured in another building (Figure 6.1); this phenomenon has not been explained in a satisfactory manner.

Power level variations across Hallway 1 were measured at various distances from the transmitter (located at  $x=0.9$  m,  $y=13.2$  m). Figure 3.8 shows the median power at points across the hallway, with the receiver 4.4 m and 12 m from the transmitter. The power carried by the 1<sup>st</sup> TE mode is plotted over the measurement at 12 m, where

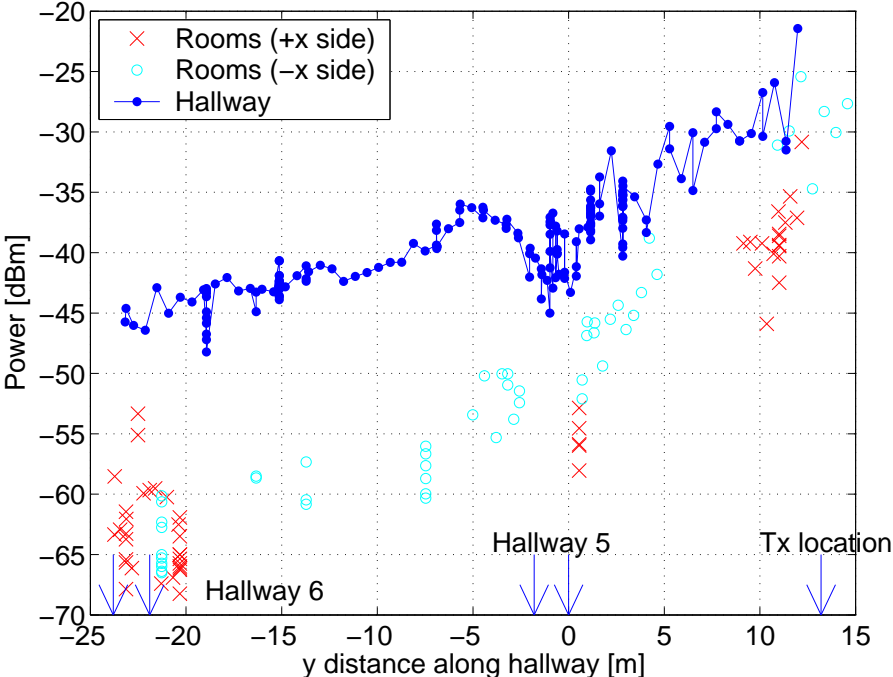


Figure 3.7: Median power in Hallway 1 and adjacent rooms. The hallway data is at points 0.5 m or more from both walls. The room data are obtained at points between 1 m and 5 m from one of the walls.

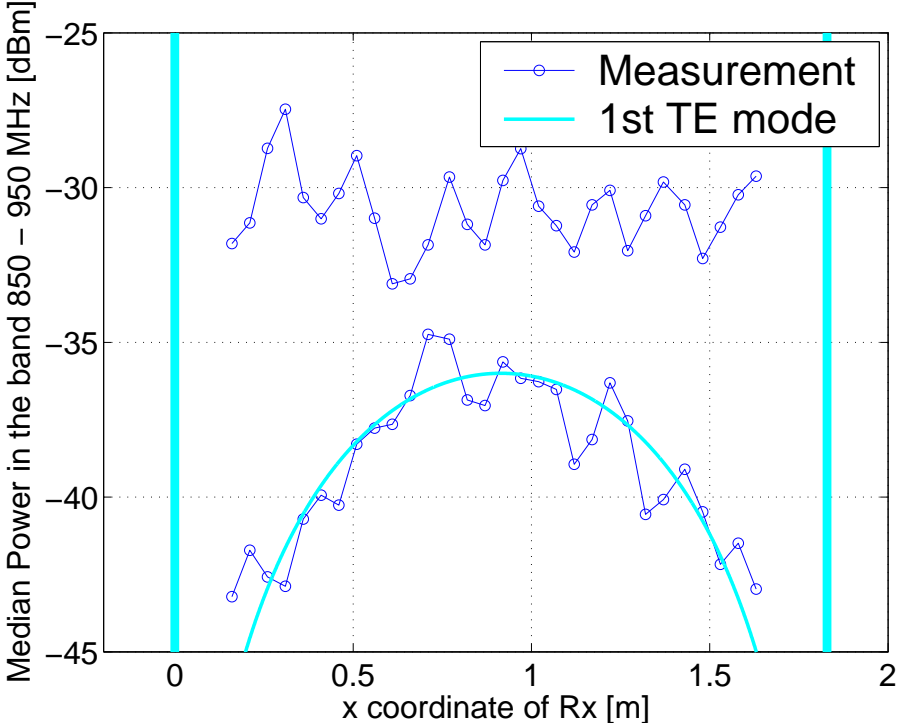


Figure 3.8: Power across Hallway 1 (median over band). Top: The receiver is 4.4 m from the transmitter. Bottom: The receiver is 12 m from the transmitter, and in a smooth line the predicted power levels for the first order TE mode. The vertical lines indicate the inner boundary of the hallway walls.

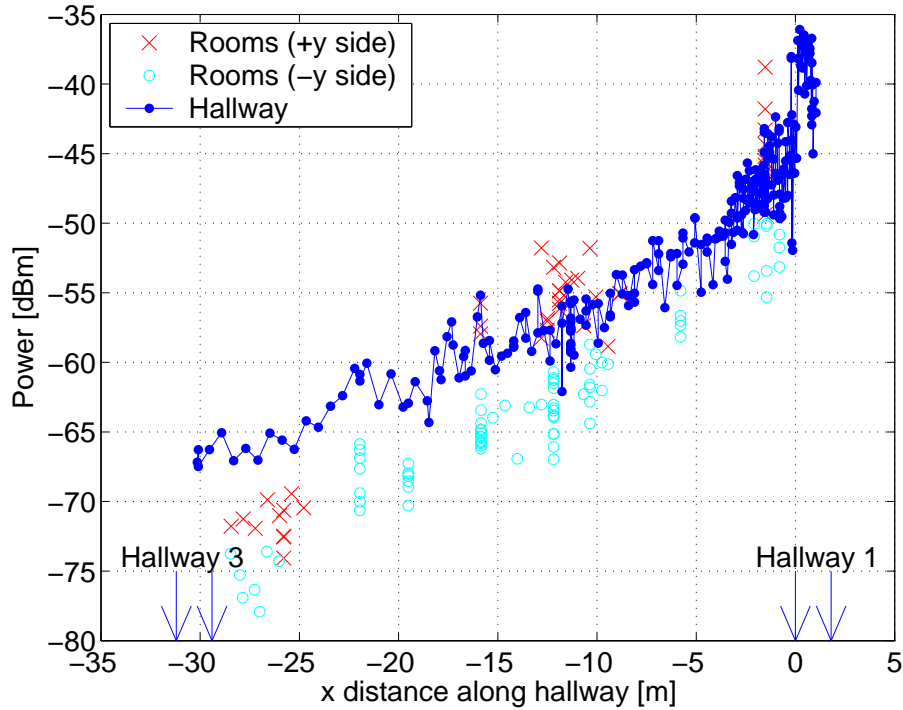


Figure 3.9: Median power in Hallway 5 and adjacent rooms

the 1<sup>st</sup> mode power was normalized to the measurement level. Measurements made in the same hallway for larger distances show a shape similar to the graph in Figure 3.8 corresponding to the 12 m distance, with higher power levels received in the center of the hallway. Measurements in other hallways did not show a similar pattern, perhaps because they have no line of sight to the transmitter.

The power in and near Hallway 5 is shown in Figure 3.9 (with the transmitter at  $x=0.9$  m,  $y=13.2$  m). The power levels in the rooms are similar to the levels in the hallway in the area closest to the junction with Hallway 1 ( $x=0$ ), with the difference growing as the receiver moves away from the junction. Rooms in the positive  $y$  side show higher power than the hallway, in the area near the junction. Rooms in this side may receive direct radiation from the transmitter normally incident on the intermediate walls. The power level in the rooms on both sides of the hallway is similar for distances bigger than about 20 m from the junction with Hallway 1 ( $x=0$ ).

Another effect is the sharp decrease of power levels at areas near the junction ( $x$

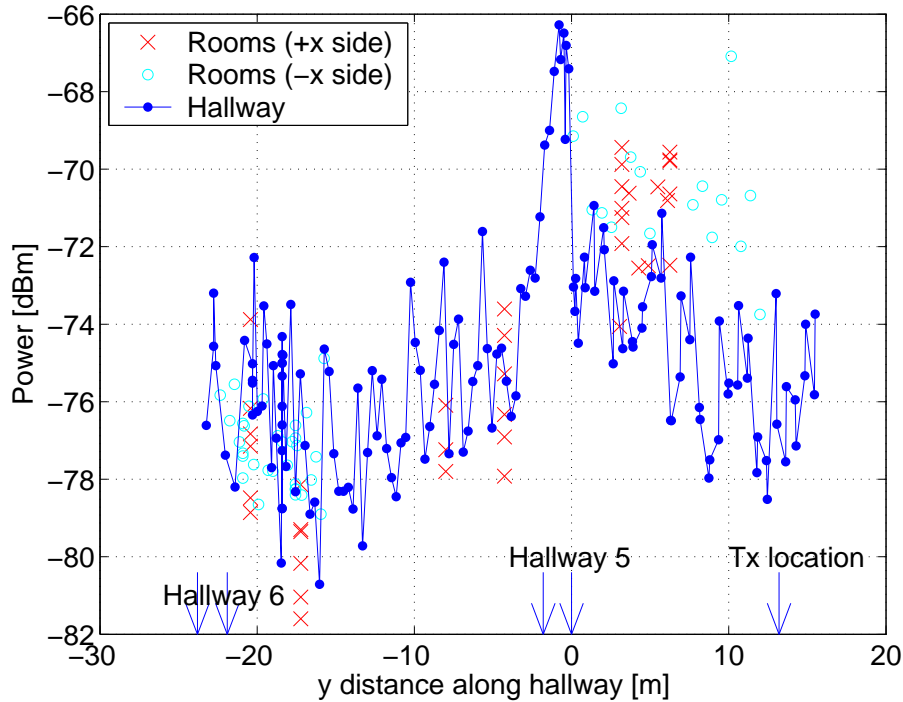


Figure 3.10: Median power in Hallway 3 and adjacent rooms

between 0 and -4 m) and the considerably lower rate of power loss at areas further away.

The power along and near Hallway 3 is shown in Figure 3.10 (with the transmitter at  $x=0.9$  m,  $y=13.2$  m). The highest power levels in this hallway were measured at the crossing with Hallway 5. An increase of power levels is evident also at the crossing with Hallway 6 (near  $y=-23$  m).

High power levels are apparent in the rooms on both sides of the hallway, for positive  $y$ . This may be explained by the normal incidence of direct propagation from the transmitter that passes through the intermediate walls with little loss.

The power along and near Hallway 6 is shown in Figure 3.11 (with the transmitter at  $x=0.9$  m,  $y=13.2$  m). The strongest power levels in Hallway 6 were measured in the junction with Hallway 1 ( $x=0$ ). The power levels in the rooms are lower than those measured in the hallway, even for rooms on the positive  $y$  side of the hallway, which are closer to the transmitter. The power levels measured in the rooms in the positive  $y$  side for  $x$  between -25 m and -30 m appear higher than those measured in the other side of the hallway. This may be an effect of the junction with Hallway 3 between  $x=-29.1$  m

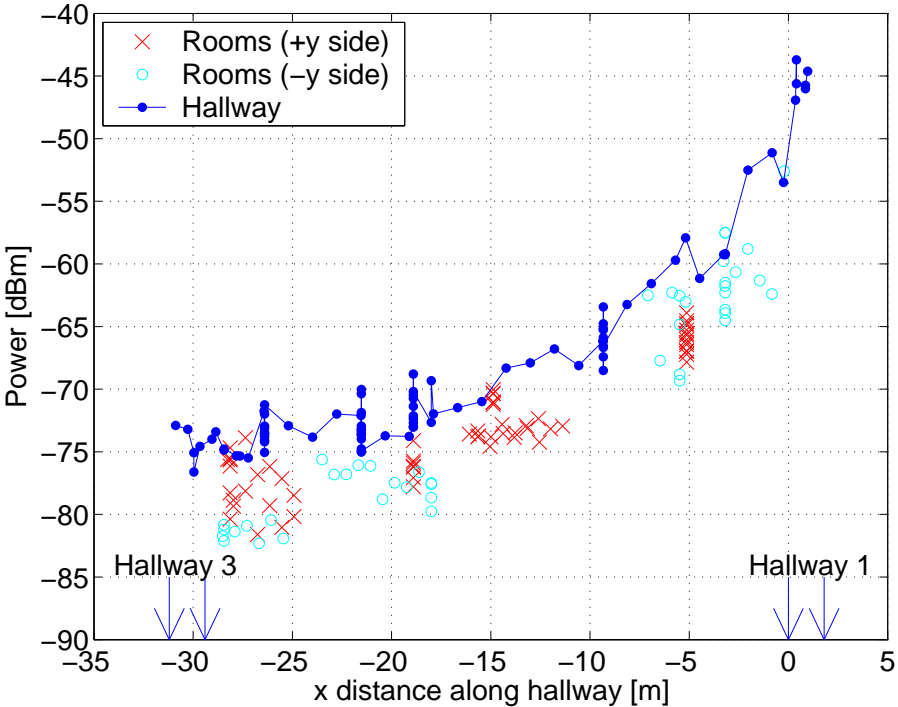


Figure 3.11: Median power in Hallway 6 and adjacent rooms

and -30.9 m.

### 3.1.4 Comparison of Measurement and Theory

The measurements along and near the hallways (Figures 3.7, 3.9, 3.10 and 3.11) show that when the receiver is 10 m or further from the transmitter, power levels are stronger in the hallways than in the adjacent rooms. This is true even when the rooms are closer to the transmitter (as in the case of Hallway 6). The power levels in the rooms may be higher than those of the hallway in cases where the direct propagation from the transmitter to the rooms is normally incident on the intermediate walls. This is shown for Hallway 3 (Figure 3.10) for positive  $y$ .

The guiding effect of the hallway is evident in Figure 3.12, where the measured power levels are higher than the free space prediction. A similar phenomenon is seen in Figure 3.16, which shows measured power levels in a line of sight hallway in another building.

The dominance of the hallway propagation over direct propagation through the walls is also clear when examining the power levels in hallway junctions. This is shown in Hallway 3 (Figure 3.10), where the power level at the junction with Hallway 5 is at least 6 dB higher than the level in adjacent rooms.

In the remainder of this chapter we show the agreement between the model presented in chapter 2 and our measurements.

The coupled mode theory presented in chapter 2 predicts that for radiation along a hallway, the low order TE modes dominate at large distances, and that a steady state rate of power loss is reached beyond an initial high loss area near the source (Section 2.2.2). The dominance of the lowest order mode is seen in Figure 3.8, where the electric field shape across the hallway is shown. The field is stronger in the middle of the hallway for sufficient distance from the transmitter, and the variation of power across the hallway matches the 1<sup>st</sup> order TE mode. Figure 3.8 shows that a uniform power across the hallway (at 4.4 m from the transmitter) evolves into a shape similar the 1<sup>st</sup> order TE mode, that is dominant in the steady state distribution of power over the modes in this hallway.

The theory predicts that the uniform field near the transmitter transforms to a field dominated by the low order modes at further distances. Calculation with the parameters

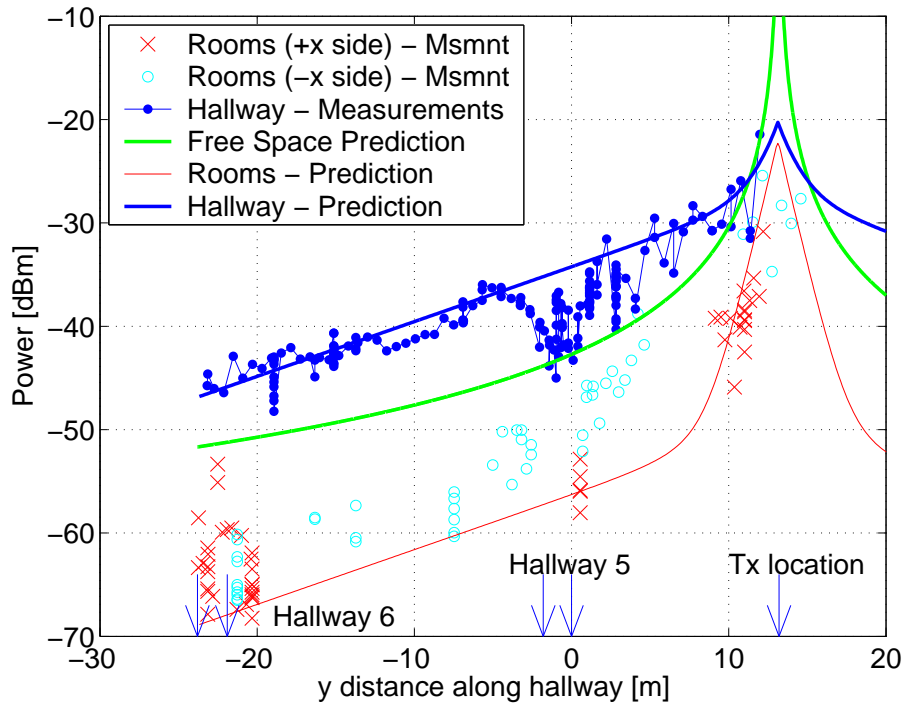


Figure 3.12: Median power in Hallway 1, with the theoretical prediction. Model parameters are  $\epsilon = 3$ ,  $\sigma = 0.075$  S/m,  $D = 2$  m and  $s^2 = 0.2$  m<sup>2</sup> and hallway width 1.8 m. The power distribution at the source is a TE narrow source in the middle of the hallway. The free space curve is an estimation based on measurements at close range.

that appear to characterize the Packard building (Hallways 1.8 m wide, walls with  $\epsilon = 3$ ,  $\sigma = 0.075$  S/m,  $D = 2$  m and  $s^2 = 0.2$  m<sup>2</sup>) shows that the steady state power distribution among the waveguide modes has almost all the power in the lowest order TE mode (Figure 3.8). The evolution from a uniform power distribution (over the modes) to the steady state takes place over a distance of about 5 m.

Figure 3.12 shows the measurements in Hallway 1, with the theoretical prediction for average power levels based on mode theory (Section 2.2.2) where the initial power distribution (over the modes) described a narrow TE source in the middle of the hallway. Power levels for a free space propagation model are also shown. The measured power is stronger than the free space prediction because of the guiding effect of the hallway (a similar result is shown in Figure 3.16 for another building). The waveguide prediction in Figure 3.12 agrees with measurements: it accurately predicts the rate of power loss

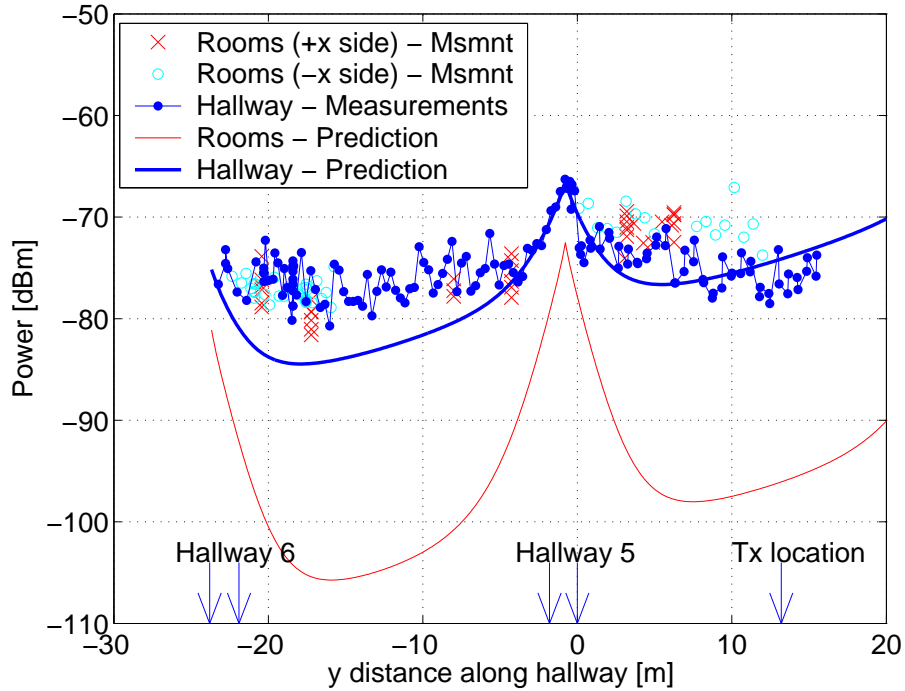


Figure 3.13: Median power in Hallway 3, with the theoretical prediction. Model parameters are  $\epsilon = 3$ ,  $\sigma = 0.075$  S/m,  $D = 2$  m and  $s^2 = 0.2$  m<sup>2</sup> and hallway width 1.8 m. The power distribution at the junction is uniform.

along the hallway.

The model predicts a significant change in the distribution of power when the receiver turns from one hallway to another. In particular, when turning from a hallway that has a steady state power distribution, the distribution after the turn is very different.

Figures 3.13, 3.14 and 3.15 show power measurements in hallways 3, 5 and 6 with the transmitter at  $x=0.9$  m,  $y=13.2$  m (Figure 3.3), and with the theoretical prediction based on the waveguide model with a uniform initial distribution (Section 2.2.2). The power level used after turning a corner was determined in the calculation from the power level calculated for the intersecting hallway. In junctions where the main hallway (that guides power into the junction) continues after the intersection, such as in a full (cross) junction, the power level at the cross hallway is half (-3 dB) of the main hallway level. In junctions where the main hallway ends (such as a corner), the power initializing the side hallway equals the power at the main hallway.

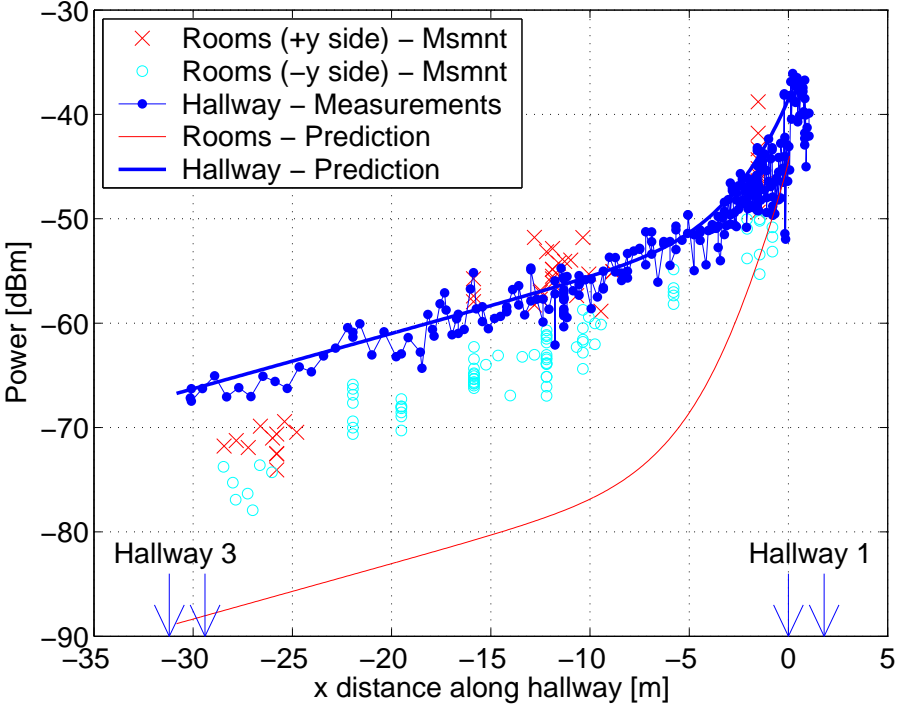


Figure 3.14: Median power in Hallway 5, with the theoretical prediction. Model parameters are  $\epsilon = 3$ ,  $\sigma = 0.075$  S/m,  $D = 2$  m and  $s^2 = 0.2$  m<sup>2</sup> and hallway width 1.8 m. The power distribution at the junction is uniform.

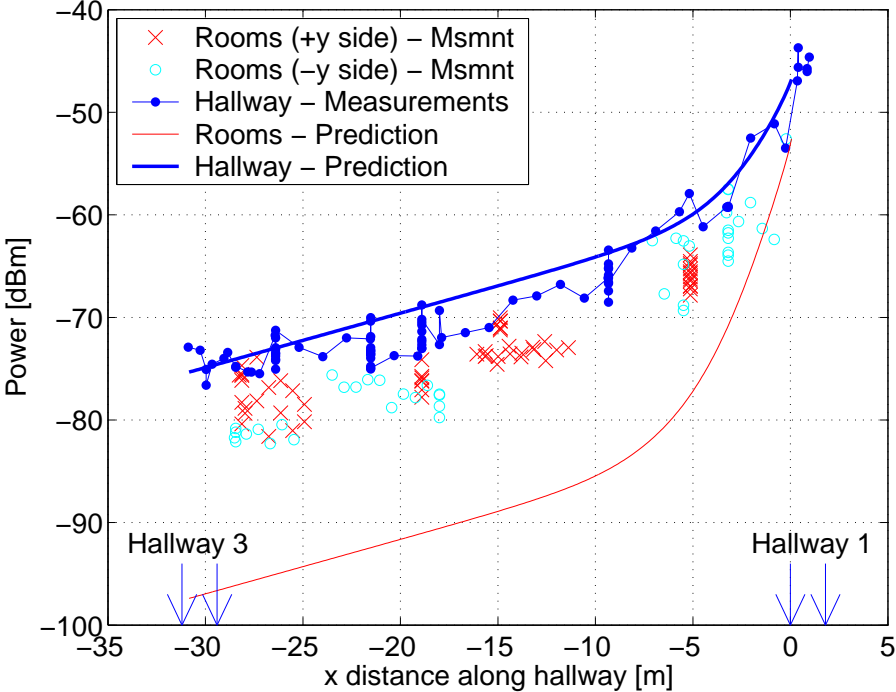


Figure 3.15: Median power in Hallway 6, with the theoretical prediction. Model parameters are  $\epsilon = 3$ ,  $\sigma = 0.075$  S/m,  $D = 2$  m and  $s^2 = 0.2$  m<sup>2</sup> and hallway width 1.8 m. The power distribution at the junction is uniform.

The agreement between measurement and theory is good for points inside Hallways 5 and 6 (Figures 3.14, 3.15). The junction effect is clearly seen in these figures, where power levels drop steeply near the junction with Hallway 1 ( $x=0$ ), and the steady state rate of power loss is attained at about 5 m from the junction. The measured power is higher than the prediction along Hallway 3 (Figure 3.13), except near the intersection with Hallway 5 ( $-1.8 \text{ m} < y < 0$ ). The high power levels are possibly the result of limitations on equipment sensitivity; these measurements may not reflect actual power levels.

### **Rooms near the Hallway**

The power level in the rooms adjacent to the hallways can be deduced in the model from the penetration of the different modes through the walls (Section 2.2.4). We note that our model considers only the hallway guiding effects, so it omits direct radiation from the transmitter.

The penetration from a hallway to the adjacent rooms varies along the hallway because the power distribution among the modes changes. The high order modes, which penetrate strongly into the walls, tend to be strong near the transmitter and hallway junctions, whereas the low order modes, that do not penetrate as well, dominate in the steady state power distribution. The power leaking from a hallway to an adjacent room is calculated for each mode separately using (2.84) and (2.85).

The agreement of the measured power levels in the rooms with the prediction is good for Hallway 1 (Figure 3.12), both near the transmitter and far from it. The agreement is not good in hallways 3, 5 and 6 (Figures 3.13, 3.14, 3.15), where measured power levels are much higher than the prediction. The difference may be partly explained by penetration of power through other paths into the rooms, and partly by the too simple model of the wall used in the calculation of the penetration coefficients in Section 2.2.4.

## **3.2 Crawford Hill Measurements**

This section presents measurements made at AT&T Bell Laboratories Crawford Hill Laboratory building in 1985. These measurements were taken by Bellcore personnel, and they are described in detail in [2].

The measurements were conducted at 815 MHz, with a small transmitter held at a height of 1.8 m at arm's length, with a vertical half-wavelength coaxial sleeve dipole antenna.

The receiver was static during the measurements. A telescoping antenna mast carried a vertical half wavelength coaxial sleeve dipole antenna at 2.9 m above the floor, near the suspended ceiling at 3 m. The analog receiver fed a digital storage oscilloscope used for data acquisition.

The measurements shown here were made in the two story building, along the first floor main hallway with the receiver at the end of the hallway. The transmitter was walked away from the receiver at 1.5 m/s along the centerline length of the hallway. During each measurement period 46 m of hallway length were covered, with 2048 signal level data points sampled at 20 msec/pt.

Each floor of the building had two hallways 1.8 m wide, intersecting in a T shape (figure 6.7), with rooms on both sides of the main hallway. Offices consisting of adjacent 3 m  $\times$  3 m cubicles lined one side of the hallway. Laboratory rooms (typically 3.7 m  $\times$  7.3 m) lined the other side of the main hallway. Inside walls were built of wood and wallboard, outside walls were largely glass. Ceilings and floors were reinforced concrete with solid corrugated steel forms between floors and in the roof.

Figure 3.16 shows the signal level measured along the first floor main hallway [15], together with power levels calculated using the waveguide model with these parameters:  $\epsilon=3.3$ ,  $\sigma=0.07$  S/m,  $s^2=0.1$  m<sup>2</sup>,  $D=2$  m, 1.8 m wide hallways with a small vertical source as an initial condition at the transmitter location. The initial power level was set so that at very close range the received power agrees with the free space prediction. The agreement between measurement and theory is good, and the guiding effect of the hallway is manifested by the power levels exceeding the free space prediction. A similar phenomenon is shown in figure 3.12.

### 3.3 Summary of Indoor Power Measurements

This chapter presented power measurements from two buildings. The Packard building measurements from Stanford were done across the basement of the building, in the hallways and rooms. The Crawford Hill Laboratory Building measurements were done

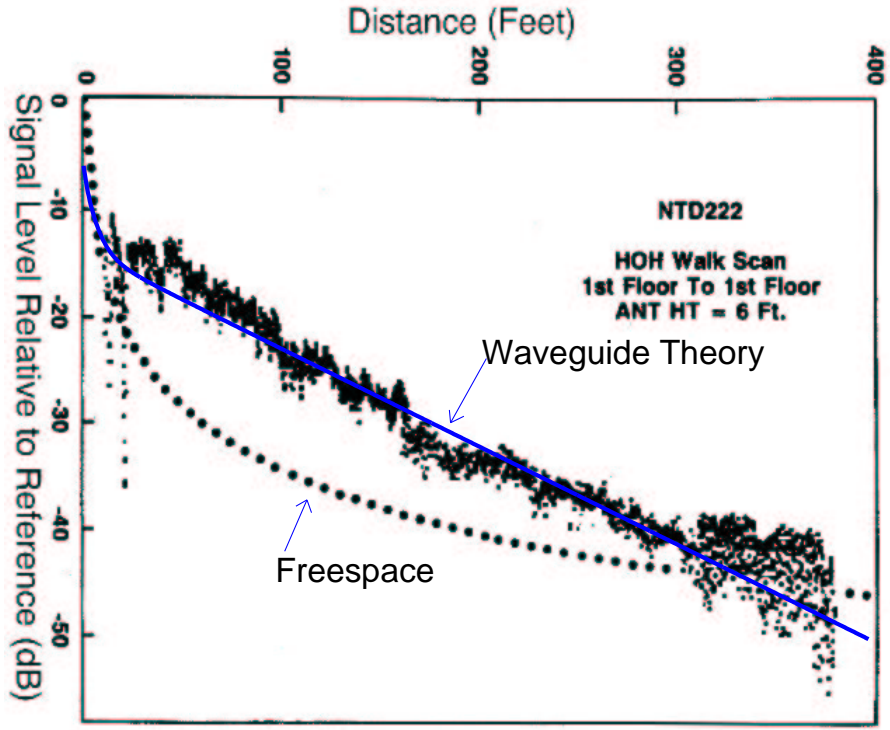


Figure 3.16: Measurement and theoretical prediction for Crawford Hill. The measured power is indicated with small square dots and the theoretical prediction with a smooth line. The large round dots indicate the predicted power in free space. Measurement data and the free space curve from [15].

in the first floor main hallway.

The waveguide theory predicts power levels in the hallways, in particular the sharp drop of power seen near hallway junctions. The room power levels are predicted accurately for Hallway 1 in the Packard Building (the line of sight hallway), but the prediction is too low for rooms near other hallways, the reason may be the over-simplified model used for wall penetration.

The waveguide theory works well for buildings with long hallways, in particular when these are mostly empty of furniture and big objects. The theory is applicable in the UHF band and above it, where the wall roughness is in the scale of a wavelength. The theory is applicable to buildings made of dense materials, where the low penetration into the walls emphasizes the guiding of radio waves in the hallways. However, even hallways with walls made of wallboard (that is easily penetrated at normal incidence) show very strong guidance, as shown in the measurements above.

Chapter 4 is similar in nature to Chapter 3; it presents power measurements in outdoor (urban) environments and compares them to the theoretical predictions.

## Chapter 4

# Outdoor Power Measurements

The measurements described in this chapter were obtained from two sources: Measurements in the 900 MHz band taken by Dr. E. Damosso and Dr. L. Stola of CSELT, Italy in Turin, Italy in 1992 [3], and measurements at 910 MHz taken by Dr. J. H. Whitteker in Ottawa, Ontario, Canada in 1986 [86]. The measurements were filtered over 2 m sections along the street: the Turin measurements were averaged over samples taken at 5 cm intervals and the Ottawa measurements were median filtered over non-uniform sampling distances, in the range of 1–2 m. This chapter presents the measurements and compares them to the waveguide model predictions.

We used the approximate widths of the streets in the calculations, but other parameters were adjusted to give the best match between measurement and theory. It is difficult to measure these parameters since they represent a simplified model of a true street. However, we used values that appear to be within realistic ranges. The electrical properties of the walls (permittivity and conductivity) were set at values reasonable for building materials ([72] Table 3.1), the geometric perturbation variance was set between 25 and 45 cm and the geometric correlation length was between 1–10 m, which correspond to the dimensions of external features of buildings. The ground was modeled as a dielectric reflector (Section 2.3).

## 4.1 Single Street Measurements (Turin)

The measurements shown in this section were taken in Turin, Italy at a frequency of around 900 MHz. The transmitter antenna was 4 m above ground and the receiver was 2 m above ground. The surrounding buildings are significantly higher than both antennas. The transmitter was static in Via Coppino, and the receiver was moved along an intersecting street, Via Baracca, that is 15 m wide.

Figures 4.1 and 4.2 show comparisons between the theory and measurements. The measurements are shown with a broken line and the theoretical prediction with a smooth line. The initial distribution of power over the modes of the side street (Via Baracca in our case) is uniform over the modes. Parameters are shown on the figure. The agreement between measurement and theory is good in both directions.

Figure 4.2 shows an increase in the measured power level that is evident near the rightmost part of the graph at large distances from the intersection. This behavior is caused by the proximity of a second street corner (at 490 m from the Via Baracca – Via Coppino intersection) that couples power into the street in the backward (-z) direction. This effect was not included in the theoretical calculation.

## 4.2 Measurements Across a City (Ottawa)

Figure 4.3 shows a map of a part of Ottawa where a measurement campaign was conducted in 1986 [86]. The location of a transmitter in Slater Street is indicated as well as the received power along the streets. The height of the buildings can be roughly estimated from the area they occupy on the map. Small buildings are usually three stories tall, and large buildings are much taller. The transmitting antenna was located 8.5 m above ground, and the receiving antenna was located 3.6 m above ground, both antennas were mounted on vehicles. A variable attenuator, with attenuation levels 0, 10, 20 and 30 dB, was used to avoid saturation of the receiver [87]. This attenuator was set manually for each street, and the attenuation values were guessed based on the measurement levels. The attenuation levels could not otherwise be determined from the data provided.

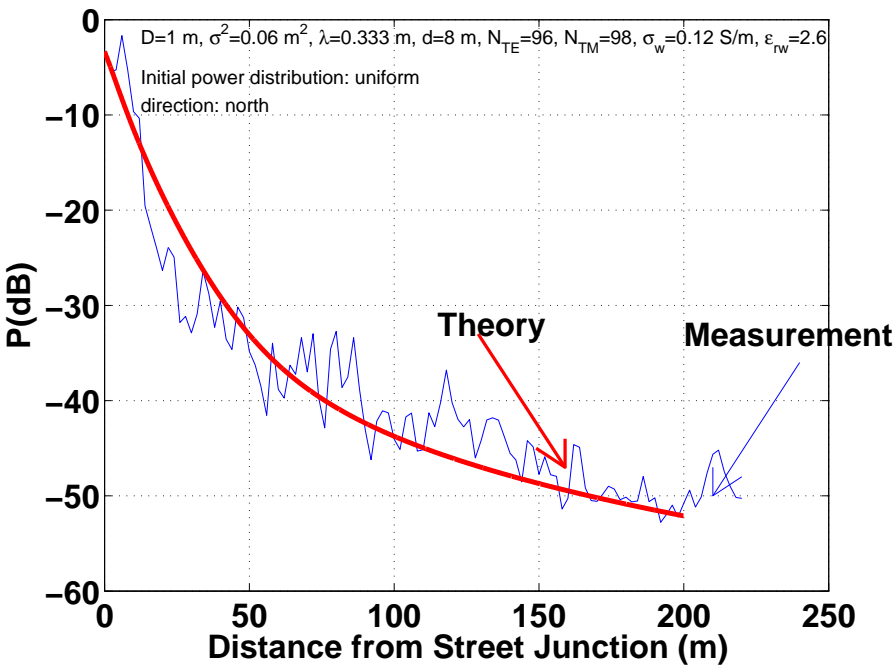


Figure 4.1: Measurements and calculation. Measurements taken in Via Baracca, Turin, Italy, moving north away from Via Coppino (that contained the transmitter).

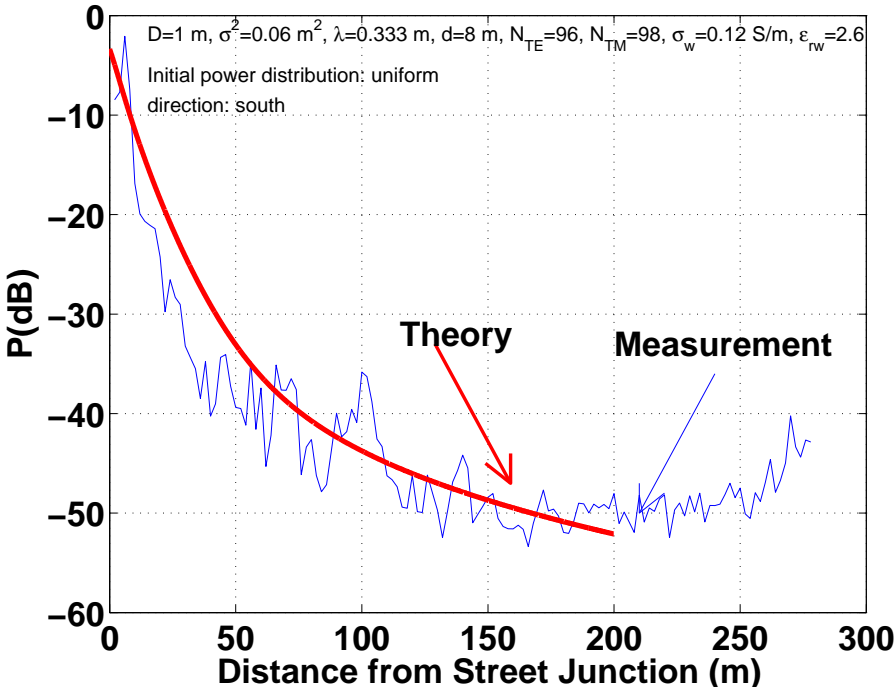


Figure 4.2: Measurements and calculation. Measurements taken in Via Baracca, Turin, Italy, moving south away from Via Coppino (that contained the transmitter).

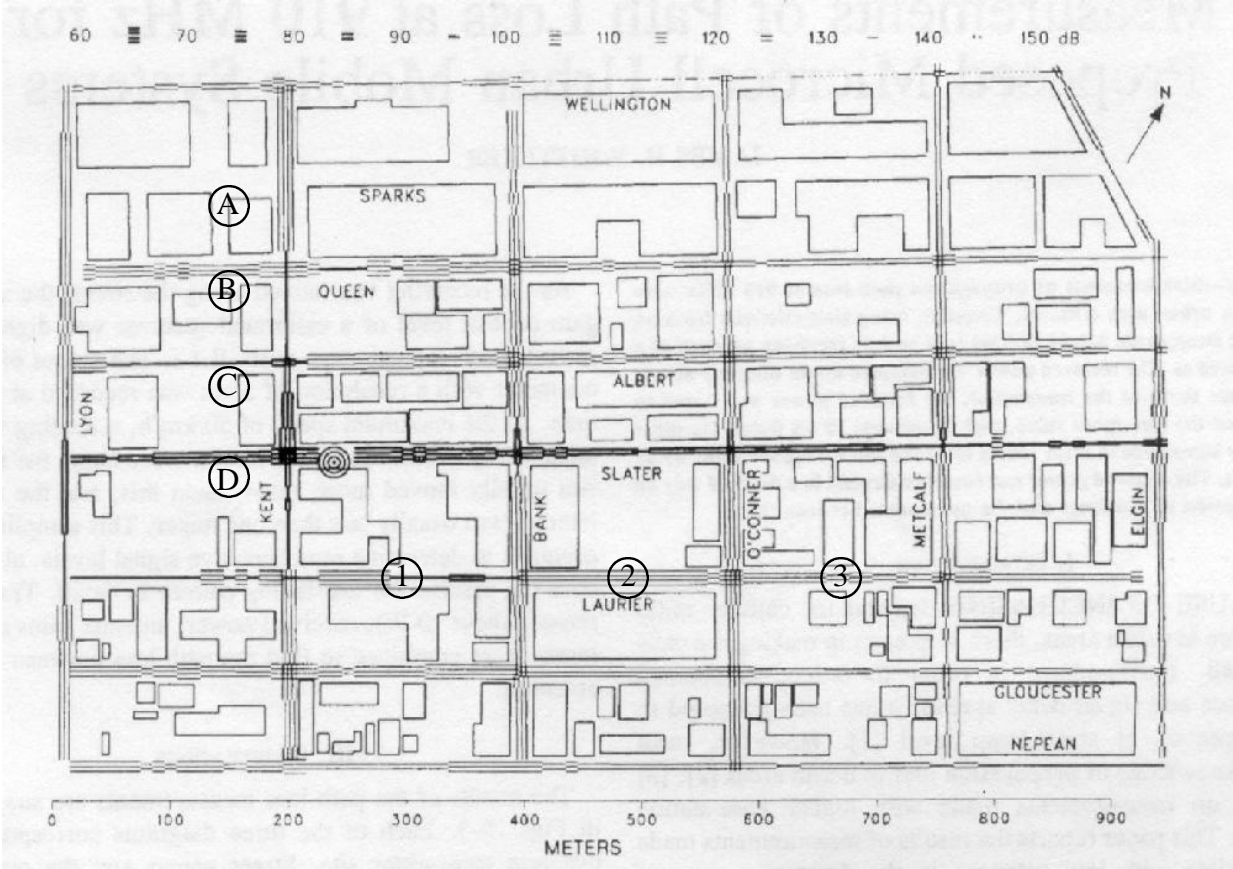


Figure 4.3: Map of Ottawa, Canada, with a transmitter at 300 Slater St. (marked by concentric circles) and path loss levels indicated by bars. Reproduction of figure 1 from J. H. Whitteker, 'Measurement of Path Loss at 910 MHz for Proposed Microcell Urban Mobile Systems', IEEE Transactions on Vehicular Technology, August 1988, Vol. 37, No. 3, ©1988 IEEE. The numbers 1–3 and the letters A–D were added to indicate city blocks.

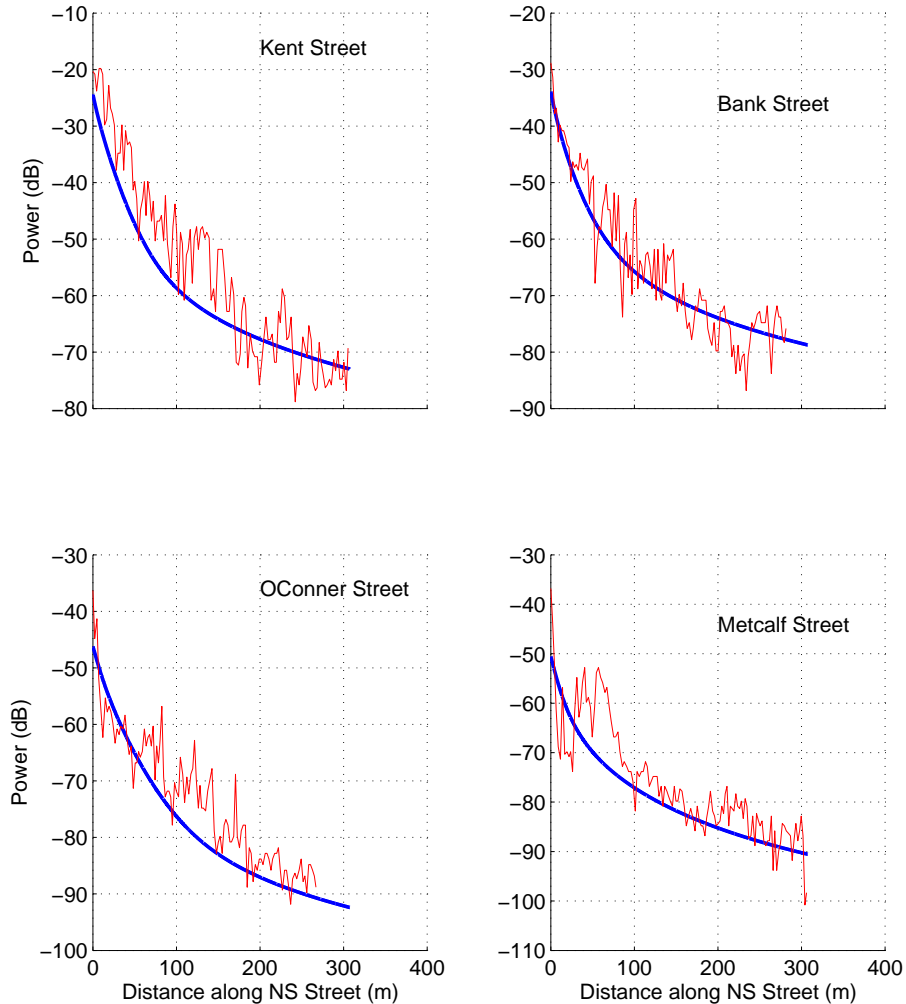


Figure 4.4: Measured Power and Prediction in Ottawa, North–South Streets

We predict the received power levels in the area between Slater St. and Wellington St., and between Kent St. and Metcalf St (the area between blocks 1–3 and A–D in Figure 4.3). The results are shown in Figures 4.4 and 4.5 together with the actual measurements. The measurements were all normalized by the transmitter power.

The prediction program calculated the power levels in all the paths that contain the transmitter and up to two turns in junctions. It is assumed that at every turning of a street corner from a main street into a side street, the power coupled into the side street is at the same level as the power at the main street. This assumption yields good agreement with the measurements, it is similar to the treatment of indoor junctions in Chapter 3. It

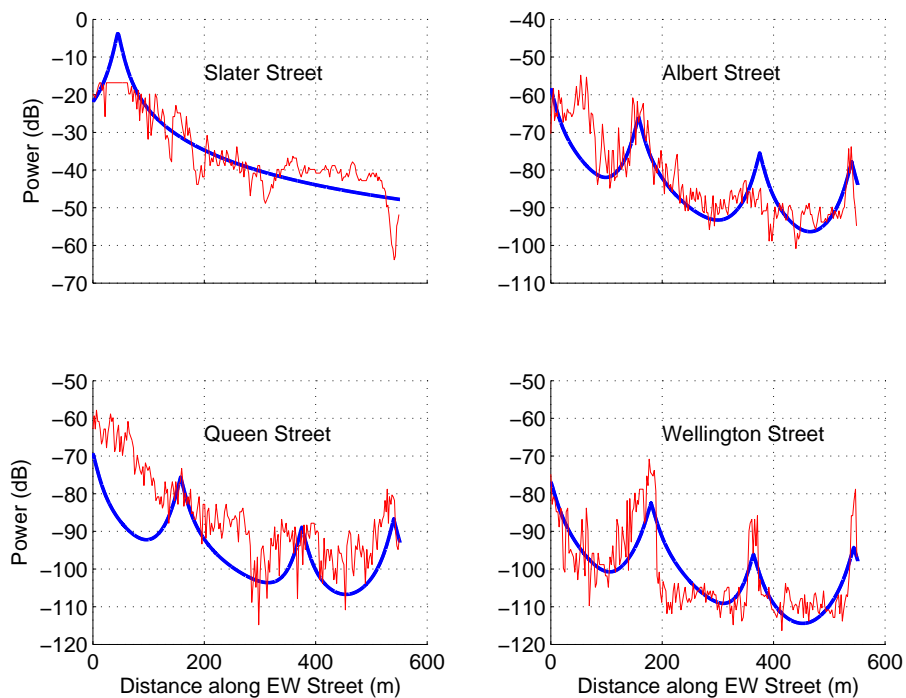


Figure 4.5: Measured Power and Prediction in Ottawa, East–West Streets

Street	Slater	Albert	Queen	Wellington
Correlation Length $D$ (m)	10	10	10	5
Perturbation Variance $s^2$ (m <sup>2</sup> )	0.08	0.2	0.1	0.1
Street Width $2a$ (m)	16	24	24	30
Wall Conductivity $\sigma$ (S/m)	0.10	0.12	0.12	0.12
Wall Permittivity $\epsilon_r$ (relative)	5	5	5	5

Table 4.1: Parameters for Ottawa east–west streets.

Street	Kent	Bank	O’Conner	Metcalf
Correlation Length $D$ (m)	5	5	5	10
Perturbation Variance $s^2$ (m <sup>2</sup> )	0.2	0.2	0.2	0.1
Street Width $2a$ (m)	16	16	24	20
Wall Conductivity $\sigma$ (S/m)	0.2	0.2	0.2	0.1
Wall Permittivity $\epsilon_r$ (relative)	3	5	3	5

Table 4.2: Parameters for Ottawa north–south streets.

was also assumed that the power flow in the main street is not affected by the presence of side streets.

The parameters used for the different streets are given in Tables 4.1 and 4.2. The parameters were set for best match between measurements and theory, and they are similar for all the streets. The initial conditions used at the transmitter location in Slater St. were a vertical antenna which was represented by a line source of TE polarization. This source is expressed as a sum over all the even TE modes. The initial condition for the other streets was a uniform distribution over the modes at the junction.

The agreement between measurement and theory is good in some streets, in particular those where the geometrical assumptions of the model hold. The north–south streets, namely Kent, Bank, O’Conner and Metcalf show a similar pattern of a steep decrease of power level near Slater Street and then convergence to the steady state slope of power levels at about 100 m from the junction (Figure 4.4). We note the difference between the measurements and theory in the southern part of Metcalf Street (left part of Figure 4.4d) between Albert Street and Queen street in blocks 3C–3D in Figure 4.3. This area of Metcalf Street is open on both sides and the waveguide model is not suitable. Power may flow from O’Conner Street or Albert Street via the almost empty block. The result is higher power levels than the theoretical prediction.

Slater Street shows a good agreement between measurement and theory, except in the area of the transmitter, where the receiver was saturated. The other east–west streets (Figure 4.5) show good agreement between the measurement and theory in areas with tall buildings on both sides of the street. In particular, Albert Street has buildings on both sides in most of block 2, and the east part of blocks 1 and 3 (Figure 4.3). The agreement between measurement and theory in these areas is better than the other parts of the street. Queen Street is flanked by tall buildings near the intersection with Bank and in the eastern part of block 2. The theory and measurement show good agreement in these areas. Wellington Street is flanked by tall buildings in its south side, but we do not know what is the construction of its north side. Wellington street shows 20 dB increase of power levels at the junctions. The power levels measured between the junctions show a pattern similar to the theoretical prediction in block 1, and a different, sharper pattern in blocks 2 and 3.

# Chapter 5

## Delay Spread

This chapter investigates the implications of the modal theory on the delay profile in microcellular urban environments; The delay profile describes the power received over time, where the transmitted signal is a narrow pulse. The steady state distribution of power over the modes translates into an exponential-like delay profile. A typical delay profile calculated using the waveguide theory compares well with an empirical model.

### 5.1 Waveguide Dispersion

The group velocity  $v_n$  is the speed of power carried by each mode [71]. For the  $n^{\text{th}}$  mode in a hollow slab waveguide it is given by

$$v_n = c \cos(\theta_n) \quad (5.1)$$

where  $c$  is the speed of light in air and  $\theta_n$  is the angle between the wave vector of the  $n^{\text{th}}$  mode and the direction of the waveguide (Figure 5.1). The velocity of information transfer equals the group velocity in a single mode waveguide. In multi-moded waveguides with no mode coupling, a single input pulse is split into a number of pulses that propagate down the waveguide. Each output pulse is carried by a different mode and travels at its group velocity.

In a waveguide with mode coupling the situation is more complicated. Energy is exchanged among the modes, so the response of the waveguide to an input pulse is

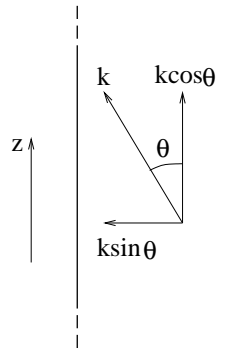


Figure 5.1: The wave vector and its components

a distorted and longer pulse instead of the comb-like response of the waveguide with no mode coupling. Mode coupling decreases the dispersion of waveguides, because it forces some power to switch between fast modes and slow modes [63].

## 5.2 Calculation of the Delay Profile

The delay spread calculated for a waveguide without mode coupling is generally an upper bound on the delay spread in similar waveguides with mode coupling. In the following section we describe the calculation of the delay profile of streets and hallways. This calculation is based on the rough waveguide model developed in Chapter 2. We use the steady state distribution of power over the modes in the rough waveguide, but calculate the delay profile in a smooth waveguide that does not introduce mode coupling. The resulting delay profile may serve to calculate an upper bound on the delay spread in real circumstances.

Consider an idealized waveguide of length  $L$  made of a similar material and with similar dimensions to the waveguide model with mode coupling presented in Chapter 2, but without mode coupling (i.e. without surface roughness). The distribution of power among the modes of this idealized waveguide is taken from the steady state distribution calculated for the waveguide with mode coupling. The power delay profile in the

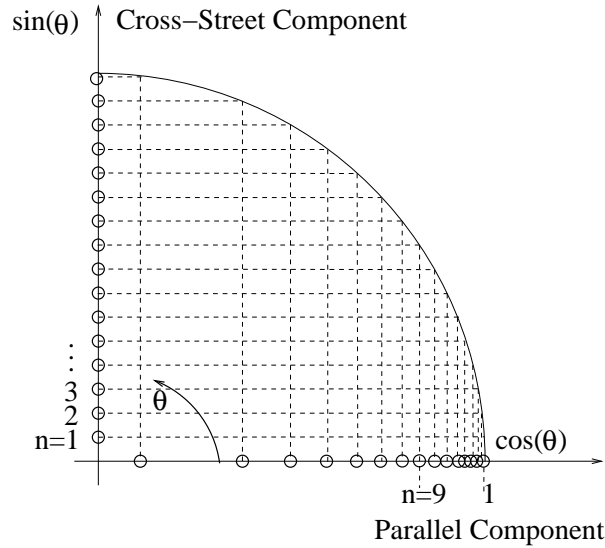


Figure 5.2: The modes of a hollow slab waveguide, described in an angular diagram. The cross-waveguide component of the wave vector increases at more or less fixed steps, while the parallel components of the low order modes are clustered.

idealized waveguide is given by:

$$P(t) = \sum_{n=1}^N P_n \delta(t - \tau_n) \quad (5.2)$$

where  $P_n$  is the power carried by the  $n^{\text{th}}$  mode and  $\tau_n$  is the delay, given by  $\tau_n = L/v_n$

In order to better understand the propagating modes, we look at their wave vectors  $\mathbf{k}_n$ , and note that the low order modes are clustered in the small angles (Figure 5.2). The difference between their group velocities is smaller than the difference between the group velocities of the high order modes. Therefore, the delays of the low order modes are spread with small differences between them, compared to the relative delays of the high order mode. This clustering of the power at low delays creates a non-uniform delay profile (Figure 5.3), where the profile is more dense at the low delays. The steady state distribution of power used in Figure 5.3 was calculated with the rough waveguide model for a 10 m wide street, with the relative dielectric constant of the walls set at  $\epsilon_r = 10$ , the conductivity set at  $\sigma = 0.4$  S/m, the variance of the wall perturbation  $0.04$  m<sup>2</sup> and the correlation length of the wall perturbation set at 5 m. The carrier frequency was

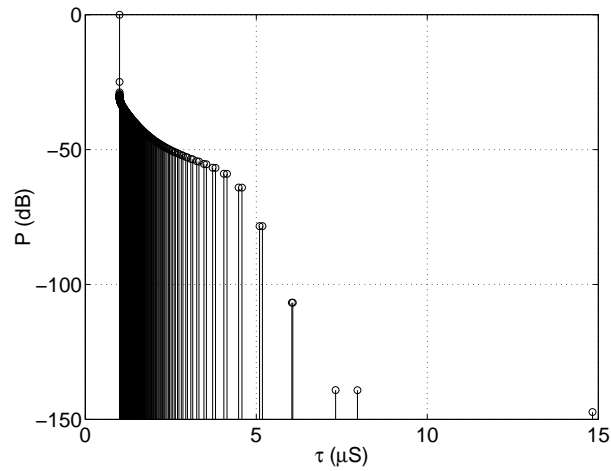


Figure 5.3: Delay profile of a multi-moded waveguide 300 m long with no mode coupling. The arrival time and power of each mode is indicated by a vertical line. Power distribution among the modes is the steady state distribution for a waveguide with mode coupling.

## 2.6 GHz.

Another reason for the importance of the low delays is the distribution of power among the propagating modes. The steady state distribution of power among the modes contains almost all the power in the low order modes which propagate with lower delays. This concentration of power, together with the clustering at the low delays, make very asymmetrical delay profiles with most of the power in the low delays.

For a transmitter located below roof level in an urban setting or in a hallway of a large building, power is spread mainly via the streets/hallways. As power flows from one ('main') waveguide into another intersecting it (the 'cross' waveguide), the distribution of power among the modes in the cross waveguide is set by the coupling mechanism at the intersection. The power distribution then returns to the steady state distribution at sufficient distances from the junction. The reference point for the delay spread in the cross waveguide is the junction.

One conclusion from the above argument is that the shape of the delay profile in waveguides that receive most of their power by coupling in a waveguide junction is only mildly dependent on the distance from the transmitter. In such waveguides, the delay profile depends strongly on the distance from the intersection where significant coupling

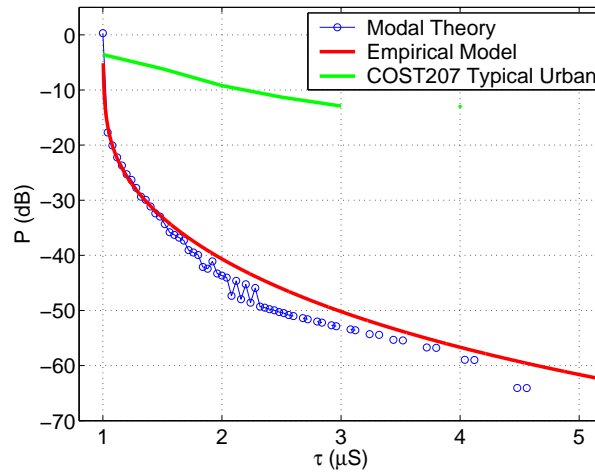


Figure 5.4: Delay profile of a multi-moded waveguide with no mode coupling, based on the steady state mode power distribution for a waveguide with mode coupling. The graph indicates the (normalized) predicted power at a receiver in the waveguide, 300 m from the transmitter. The delay profile calculated from *Ichitsubo*'s empirical model and from COST207 are also plotted.

takes place. The distance from the transmitter affects the delay profile by shifting it without a major change of its shape.

### 5.3 Comparison with an Empirical Model

We compare our calculated delay profiles to the empirical model suggested by *Ichitsubo et al.* [36] for line of sight (LOS) in streets at 2.6 GHz. We consider the LOS case the most appropriate for comparison because our model does not include propagation paths over the roofs of buildings, and each street intersection where power couples from one street to another effectively resets the shape of the delay profile.

The delay profile from Figure 5.3 for  $\tau$  less than  $5.2 \mu\text{S}$  is plotted again in Figure 5.4, where the graph represents the received power over time. Overlaying it is a delay profile calculated using *Ichitsubo*'s empirical model [36] for LOS microcellular streets, with the transmitter and receiver 300 m apart. The empirical model is a power function of time. The two profiles are quite similar.

Figure 5.4 also includes the delay profile calculated from the COST207 Typical Urban Model [78], Section 2.3.3. This model was developed for macrocellular environments and it predicts higher delay spread than the spread predicted by the two other models. The reason for the big difference is that line of sight locations have a propagation path that is much shorter than the typical urban paths in a macrocell environment.

The parameters used for the theoretical calculation were chosen for best match with the empirical model. It appears that these parameters describe the average electrical and geometrical properties of the environment of measurement (in the metropolitan area of Tokyo), but this was not validated otherwise. The agreement between the two models is good for transmitter–receiver separations in the range of 200–400 m, where 400 m is the range of validity of the empirical model [36]. For smaller transmitter–receiver separations, the assumption that the power distribution among the modes is similar to the steady state one is not valid, and the calculation of the delay profile based on modal considerations is more complicated.

The parameters used here to determine the steady state mode power distribution ( $\epsilon_r = 10$ ,  $\sigma = 0.4$  S/m,  $s^2 = 0.04$  m<sup>2</sup>,  $D = 5$  m and 2.6 GHz carrier frequency) are different from those used in Chapter 4 for comparison with the Ottawa measurements. The difference may indicate the range of variation of the parameters, but it is hard to determine this range because of insufficient measurement data. The difference in parameter values may also result from the difference in construction materials between Tokyo and Ottawa. The measurement frequency is also different in the two cities, and this may be an additional source of variation in the waveguide model parameters.

# Chapter 6

## Channel Capacity

Multiple antenna systems have received considerable attention in recent years, because of the promise they hold for very large channel capacities. High capacities are available when the sub-channels connecting each transmit antenna to each receive antenna are independent. Any coupling among these sub-channels causes reduced capacity. Two types of interaction among the sub-channels are:

- Correlation among the sub-channels, which may result from scattering off objects near the transmitter or the receiver.
- A keyhole effect [13, 33], which is caused by similarity of the propagation paths.

Both types of interaction reduce the rank of the channel matrix. In this chapter we investigate the limits on capacity, set by the propagation of radio waves in a waveguide with mode coupling. The channel is decomposed into the waveguide modes and the coupling among them reduces the channel matrix rank. The mechanism we discuss may cause high antenna correlation and/or a keyhole effect, depending on the extent of local scattering near the transmitter and receiver. High antenna correlation is expected for systems with little scattering near the transmitter and receiver; A significant keyhole effect is present for systems with a lot of local scattering at both ends. This is the situation in the measurements presented in this chapter.

The coupling among propagating modes in a waveguide reduces the channel capacity along the waveguide. A multiple antenna system operating in a building hallway shows diminishing capacities as the distance between the transmitter and the receiver

grows. This decrease in capacity is the result of a keyhole effect caused by mode coupling, and the decrease of power levels at growing distances from the transmitter. The capacity of channels with one end in a hallway and the second in a room beside the same hallway is also affected by the guiding of power along the hallway. The keyhole effect reduces the capacity of such channels as the distance increases along the hallway between the transmitter and the receiver.

The capacity was estimated from channel measurements, and a decrease is apparent along the hallway with growing distances from the transmitter. This decrease occurs in the hallway as well as in the rooms located beside it. We suggest that the main propagation mechanism into the rooms is leakage from the hallway, through the interior walls of the building. A keyhole effect in the hallway limits the capacities measured along it and in the adjacent rooms.

## 6.1 Theoretical Analysis

The general framework we consider is a linear time invariant narrow-band channel model:

$$\bar{v} = \mathbf{T} \bar{u} + \bar{n} \quad (6.1)$$

where  $\bar{v}$  is the received signal vector with  $N_r$  entries,  $\bar{u}$  is the  $N_t \times 1$  transmit vector and  $\bar{n}$  is the  $N_r \times 1$  noise vector. The noise at different antennas is assumed to be independently white Gaussian noise with average power  $\sigma^2$ .  $\mathbf{T}$  is the  $N_r \times N_t$  complex channel matrix, and we define the normalized channel matrix  $\mathbf{H} = \frac{1}{g} \mathbf{T}$ , where  $g^2 = \frac{1}{N_t N_r} \sum_i \sum_j |T_{ij}|^2$ .

The channel capacity for the case where each transmit antenna transmits with average power  $P_a$  is given by [31]:

$$C = \log_2(\det(I + \frac{P_a}{\sigma^2} \mathbf{T} \mathbf{T}^+)) = \log_2(\det(I + \frac{\rho}{N_t} \mathbf{H} \mathbf{H}^+)) \quad (6.2)$$

where  $\rho$  is the average SNR at each receiver branch and  $(\ )^+$  signifies the conjugate transpose operation.

### 6.1.1 Channel Capacity in a Smooth Waveguide

We proceed to express the channel matrix  $\mathbf{T}$  for an indoor hallway environment, where the hallway is modeled as a slab (two dimensional) waveguide with no variation in the  $y$  (vertical) direction. A three dimensional treatment is very similar and yields similar qualitative results [70]. Consider a hollow waveguide with the transmitter and a receiver at different positions along it. The waveguide modes act as eigenfunctions of the structure in the sense that power can only propagate in a modal fashion. The modes are of either of two polarization: transverse electric (TE) with zero electric field in the  $z$  direction, and transverse magnetic (TM), with zero magnetic field in the  $z$  direction. The variation of the electric field across the waveguide is described in Chapter 2.

Consider a set of transmitting antennas in a waveguide situated at  $z = 0$ . The  $i^{\text{th}}$  antenna excites the waveguide modes with amplitudes  $\bar{A}_i(0) = [A_{i1}, A_{i2}, \dots, A_{iN}]^T$  when it transmits a unit signal ( $[]^T$  stands for transpose). We form the matrix  $\mathbf{A}$  by stacking the vectors  $\bar{A}_i$  next to each other. It contains the complex amplitudes of all the modes, excited by all the antennas, so the  $(n, i)$  entry contains the excitation of the  $n^{\text{th}}$  mode by the  $i^{\text{th}}$  antenna. A lossless waveguide with smooth walls does not induce variations in the modal amplitudes, in which case the modal amplitudes are fixed at  $\mathbf{A}(z) = \mathbf{A}(0)$ .

The electric field received by the  $j^{\text{th}}$  receiving antenna, located at  $(x, z)$ , is expressed as a sum of modes. The  $y$  component of the field is

$$E_y = \sum_{n=1}^N A_n \begin{Bmatrix} \cos \\ \sin \end{Bmatrix} \left( \frac{u_n}{a} x \right) e^{-j\beta_n z} \quad (6.3)$$

where  $A_n = \sum_{i=1}^{N_t} A_{in}$  is the amplitude of the  $n^{\text{th}}$  mode. In the absence of noise, the received field in all the receiver antennas  $\bar{E}_r$  is expressed in a matrix equation:

$$\bar{E}_r = \mathbf{V} \mathbf{Z} \mathbf{A} \bar{E}_t \quad (6.4)$$

where  $\bar{E}_t$  is an  $N_t \times 1$  vector containing the transmitted signals at the  $N_t$  transmit antennas. The matrix  $\mathbf{Z}$  is an  $N \times N$  diagonal matrix with the elements  $e^{-j\beta_n z}$  on the diagonal. The matrix  $\mathbf{V}$  is an  $N_r \times N$  matrix that contains the contribution of each mode to the

signal received on each receiver antenna. The  $(i, n)$  element of  $\mathbf{V}$  is

$$\begin{Bmatrix} \sin \\ \cos \end{Bmatrix} \left( \frac{u_n}{a} x_i \right) \quad (6.5)$$

where  $x_i$  is the component of the location of the  $i^{\text{th}}$  receiver antenna and  $\cos$  or  $\sin$  are chosen according to the symmetry of the mode. The matrix  $\mathbf{A}$  is the excitation matrix determined by the transmitter location. We assume that all the receiver antennas are located at the same  $z$  coordinate.

By comparing (6.1) and (6.4) we see that the channel transfer matrix is given by

$$\mathbf{T} = \mathbf{P} \mathbf{A} \quad (6.6)$$

where  $\mathbf{P} = \mathbf{V} \mathbf{Z}$  contains the geometry of the receiver and  $\mathbf{A}$  describes the excitation.

### 6.1.2 Channel Capacity in a Rough Waveguide

In an ideal waveguide (with no loss and no mode coupling) the modal amplitudes are fixed at the transmitter location so  $\mathbf{A}(z) = \mathbf{A}(0)$ . In a real waveguide there is loss and coupling among the modes, and we consider a linear coupling model which is described by an equation of the form:

$$\frac{\partial \mathbf{A}}{\partial z} = \mathbf{\Gamma}_A \mathbf{A} \quad (6.7)$$

The diagonal elements  $\Gamma_{Ann}$  contain the loss coefficients of each mode  $c_{nn} = -j\beta_n''$ , where  $\beta_n''$  is given in (2.27)–(2.28). The off-diagonal element  $\Gamma_{Amn}$  contains the coupling factor from mode  $n$  to mode  $m$ , they are given by  $\Gamma_{Amn} = c_{mn}$ , where  $c_{mn}$  are given in (2.68). The average coupling factors between any pair of modes depend on the electrical properties of the waveguide walls, the waveguide dimensions and the statistics of the wall perturbations. Note that equation (6.7) is the matrix form of equation (2.63).

We now use the waveguide mode analysis with the linear coupling model to study the effect of coupling on the capacity of radio channels propagating in an indoor environment. In the calculations presented in section 6.2, we solve the average power coupled mode equation (2.79) instead of the amplitude coupled mode equation (6.7). This is done because the wall roughness functions ( $f(z)$  and  $h(z)$ ) are not given exactly,

but their statistical properties are known.

We begin the analysis by studying the solutions of equation (6.7). The general solution is a matrix  $\mathbf{A}(z)$ , where each column  $\bar{A}_i(z)$  is of the form:

$$\bar{A}^i(z) = \sum_{n=1}^N C_n^i \bar{B}_n e^{\lambda_n z} \quad i = 1, 2 \dots N_t \quad (6.8)$$

$\bar{B}_n$  are the eigenvectors of  $\Gamma_A$  and  $\lambda_n$  are the corresponding eigenvalues;  $C_n^i$  are scalar constants.

At large distances from the source, the modal coefficients converge to

$$\bar{A}_i(z) \rightarrow C_1^i \bar{B}_1 e^{\lambda_1 z} \quad (6.9)$$

where  $\lambda_1$  is the eigenvalue of  $\Gamma$  that has the biggest real part. Expression (6.9) is the steady state solution of the coupled modes equation (6.7). In this solution, the only variation along the hallway is  $e^{\lambda_1 z}$  (except for changes of the phase along  $z$ , which are included in  $\mathbf{Z}$ ). The steady state modal distribution has most of the power in the low order modes, because they have the least loss. We stress that (6.9) represents the average behavior at large distances from the transmitter. The actual behavior fluctuates around this average.

After convergence to steady state, the matrix  $\mathbf{A}$  is of the form

$$\mathbf{A} = \bar{B}_1 \begin{bmatrix} C_1^1 & C_1^2 & \dots & C_1^N \end{bmatrix} e^{\lambda_1 z} \quad (6.10)$$

and its rank equals one. From equation (6.6) this implies that the channel transfer matrix  $\mathbf{T}$  also has rank 1. At small transmitter—receiver distances the channel capacity is limited by the number of transmitter or receiver antennas [31], but at larger distances on the order of 10–20 m and above it is limited by the physics of the propagation channel. The reduced capacity results from high correlation between antennas or from a keyhole effect, depending on the environment of the transmitter and receiver, and the amount of local scattering. A similar behavior is predicted in [46, 13], where modal loss is the mechanism limiting the capacity of the channel. Another case of a limit on capacity for distant transmitter and receiver is shown in [76], where the propagation model is based on rays.

The convergence of  $\mathbf{A}(z)$  from an initial condition to the steady state behavior is accompanied by a convergence of the power loss rate. The initial power loss rate varies along  $z$ , as the amplitudes of the different modes change. When the steady state is reached, the power loss rate becomes  $2 \operatorname{real}(\lambda_1)$  Np/m. The convergence of the power loss rate in measurements is shown in the next section, with the reduction of capacity along a hallway.

## 6.2 Measurements

This section presents channel capacities estimated from channel measurements that were taken with a system with 12 transmit antennas and 15 receive antennas. The measurements were taken by Persefoni Kyritsi in the Bell Labs Crawford Hill Laboratory Building [46, 45], described in Section 3.2. The transmitter was located in a hallway and the receiver was located at different positions along the same hallway and in adjacent rooms (see section 6.3 for details of the measurement equipment and locations).

Figure 6.1 shows the average power measured at different positions along the hallway, averaged over 100 separate measurements at each location. These results, similar to those shown in Chapter 3, show that the power loss rate in hallways converges around 10 m from the transmitter. The variation of power in Figure 6.1 between 10 m and 20 m corresponds to the location of a junction of hallways (a similar phenomenon is seen in Figure 3.7).

The convergence of the power loss rate indicates the distance of convergence of  $\mathbf{A}$  to the steady state. Waveforms across the hallway converge to a half sinusoidal shape as seen in Figure 6.2. This is a consequence of the steady state modal distribution that has most of the power in the lowest order mode.

The capacity results shown below were calculated using (6.2) at different locations, with the signal to noise ratio fixed at  $\rho = 20$  dB. Figures 6.3 and 6.5 show the average capacity, over 100 separate measurements of the channel matrix at each location. A fixed value was used for the signal to noise ratio in order to isolate the effects of the channel variation from the effects of the power roll-off with distance.

Figure 6.3 shows the capacity calculated from the channel measurements at different locations along the hallway. The figure also contains the mean capacity calculated for

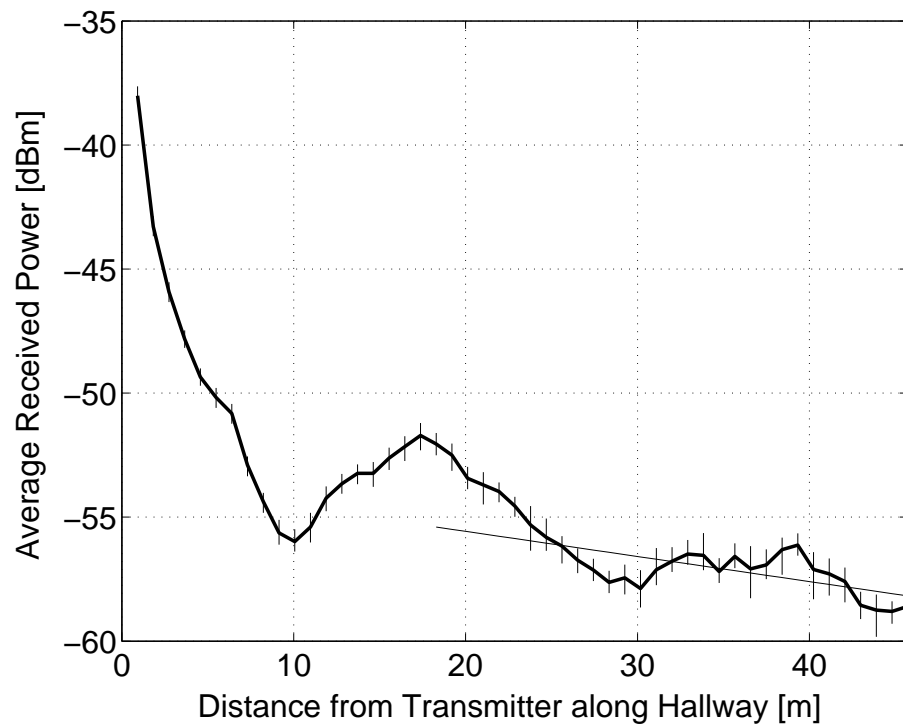


Figure 6.1: Average power along the hallway. The straight line indicates the approximate steady state power loss rate. The short vertical lines indicate the minimum and maximum power levels received at each location.

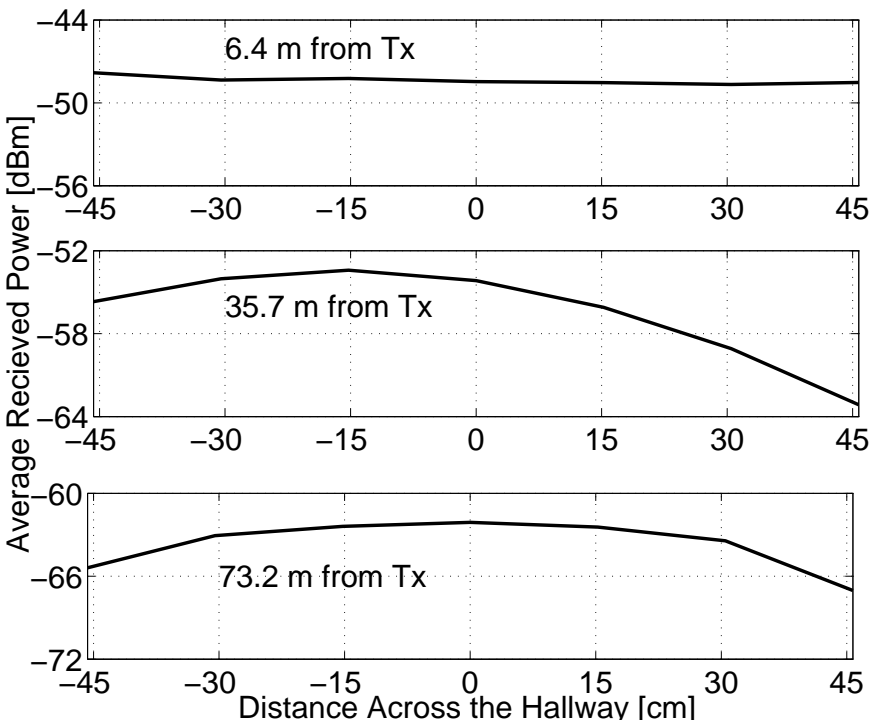


Figure 6.2: Power measured across the hallway. For the top plot, the receiver is 6.4 m from the transmitter, the middle plot is at 35.7 m and the bottom plot is at 73.2 m

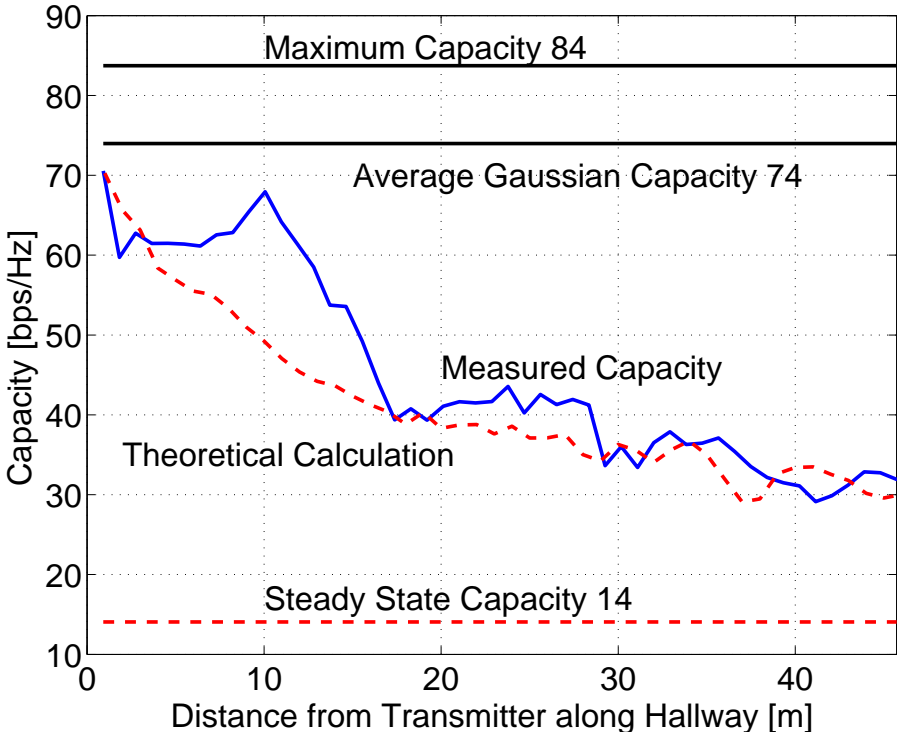


Figure 6.3: Average capacity of the measured channel in the hallway for SNR=20 dB and theoretically calculated capacity.

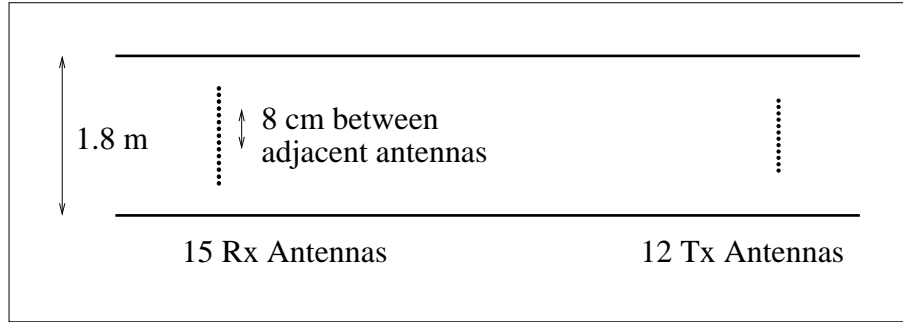


Figure 6.4: Antenna arrangement used in the waveguide calculation

a channel matrix with 180 independent Gaussian entries with average SNR of 20 dB and the maximum capacity with 12 transmit antennas and 15 receive antennas and the same SNR. The maximum capacity is calculated for a channel matrix with full rank and equal eigenvalues, and the mean capacity is taken over all channels with independent Gaussian entries in the channel matrix. The graph shows a reduction in capacity along the hallway.

Figure 6.3 also shows the capacity along the hallway, calculated from the coupled waveguide model. The model is two-dimensional, so the arrangement of the antenna arrays was simplified. The transmitter array used in the calculation contained 12 antennas arranged across the hallway around its center, as shown in Figure 6.4. The distance between adjacent antennas is 8 cm, and the operating frequency is 1.95 GHz, as in the real system. The other model parameters were taken from the calculation for the Packard building (Chapter 3), since that building and the Crawford Hill Laboratory building have similar construction.

The matrix  $\mathbf{A}(z)$ , that contains the amplitudes of all the modes along the hallway was modified using the power distribution over the modes, instead of using (6.7). Each column of  $\mathbf{A}(z)$  was calculated by

$$\bar{\mathbf{A}}_i(z) = \begin{bmatrix} A_{i1}(z) \\ \vdots \\ A_{iN}(z) \end{bmatrix} = \begin{bmatrix} A_{i1}(0)\sqrt{P_1(z)} \\ \vdots \\ A_{iN}(0)\sqrt{P_N(z)} \end{bmatrix} \quad (6.11)$$

where the power distribution over the modes was calculated by solving equation (2.79).

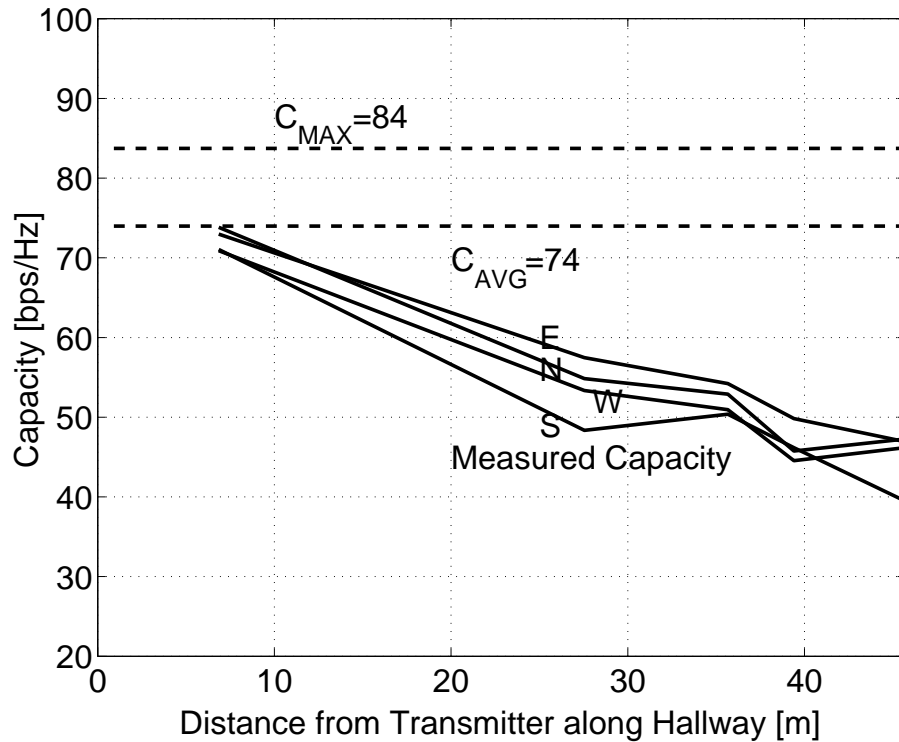


Figure 6.5: Average capacity of the measured channel in the labs for SNR=20 dB, for the receiver antenna facing the four cardinal directions.

The approximation of the modal amplitudes is needed because the coupling model presented in Chapter 2 applies to the power of the mode and not to their amplitudes.

Figure 6.3 also shows the capacity calculated for the steady state power distribution (section 2.2.2). This value, here 14 bps/Hz, is the limit of convergence of the theoretically calculated capacity at large distances from the transmitter.

Figure 6.3 shows good agreement between the measurements and the theoretical calculation. The high capacities measured at distances around 10 m from the transmitter are related to an intersection with another hallway in this area. The effects of this intersection were not included in the theoretical calculation.

Figure 6.5 shows capacity results for the channel measured in the laboratory rooms adjacent to the hallway (see the schematic plan in Figure 6.7). The horizontal axis contains the transmitter – receiver separations along the hallway. The figure also contains the mean capacity calculated for a Gaussian channel and the maximum capacity with 12

transmit antennas and 15 receive antennas. Four different graphs are shown, for the four orientations of the receiver array. The results for the four orientations are similar.

The capacity in the rooms adjacent to the hallway drops with increasing distance from the transmitter. The effect of the power level was excluded so the reduction of capacity values seen here is the result of variations in the channel matrix.

The decrease of capacity with distance (Figures 6.3, 6.5) is the result of the propagation mechanism. Most of the power in the rooms was leaked from the hallway, through the wallboards, so a low rank channel at a certain location in the hallway causes low capacities in nearby rooms.

The measured receiver correlation is low ( $<0.25$ ) for all measurements. Transmitter correlation cannot be estimated directly from the measurements, but it is similar to the receiver correlation in the hallway because of the symmetric geometrical arrangement of the two arrays.

### 6.3 The Measurement Setup and Environment

Some details were omitted from the descriptions below. For a full description of the measurements see [45].

#### Description of the Measuring Equipment

The measurements were taken with two antenna arrays: the transmitter array comprised 12 elements arranged on the sides of a square, and the receiver array comprised 15 elements arranged in a grid. Adjacent antennas were separated by 8 cm, and the elements on both arrays were arranged with alternate polarizations. Figure 6.6 shows the transmitter and the receiver arrays as seen from the front where V and H stand for vertically and horizontally polarized elements. The two arrays were placed at a height of 1.8 m above the floor. The system bandwidth was 30 kHz, the filters were raised cosine filters with a bandwidth expansion factor of  $\alpha = 0.23$ . The symbol rate was 24.3 ksymbols/sec and the symbol duration was 41.2  $\mu$ sec. That is long enough to support the narrow-band assumption, since the maximum delay spread measured in this buildings was 220 nsec, at a carrier frequency of 850 MHz ([23], Office HOH). The constellation size used was 4 QPSK and the operating frequency was 1.95 GHz.

V <sub>1</sub>	H <sub>6</sub>	V <sub>6</sub>	H <sub>5</sub>
H <sub>1</sub>			V <sub>5</sub>
V <sub>2</sub>			H <sub>4</sub>
H <sub>2</sub>	V <sub>3</sub>	H <sub>3</sub>	V <sub>4</sub>

H <sub>5</sub>	V <sub>6</sub>	H <sub>6</sub>	V <sub>1</sub>
V <sub>5</sub>	H <sub>8</sub>		H <sub>1</sub>
H <sub>4</sub>	V <sub>7</sub>	H <sub>7</sub>	V <sub>2</sub>
V <sub>4</sub>	H <sub>3</sub>	V <sub>3</sub>	H <sub>2</sub>

Figure 6.6: Antenna array layout, V and H represent different polarizations.

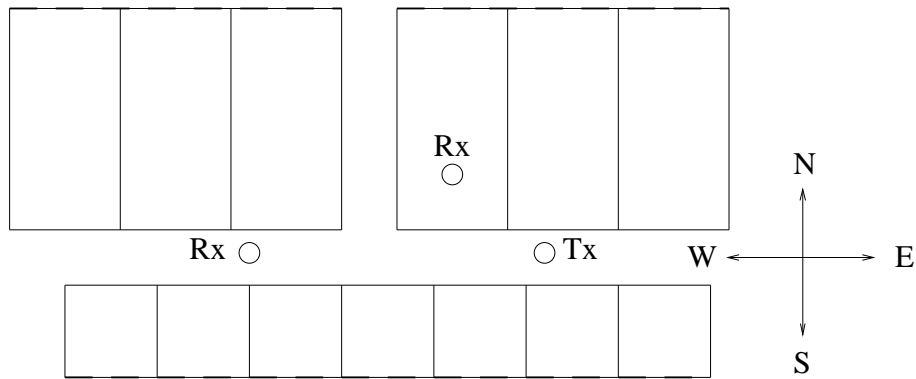


Figure 6.7: Geometry of hallways with the transmitter location and two receiver locations

**Description of the Measuring Process**

The measurements were taken within the Lucent (formerly AT&T) Crawford Hill Building, in the second floor main corridor, shown schematically in Figure 6.7. This straight 119 m corridor is 1.8 m wide, lined with offices (typically 3 m×3 m) on one side and laboratories (typically 3.7 m×7.3 m) on the other. A second corridor intersects the first one in a T shaped junction, but no measurements were taken in that hallway. The building extends in both the east and the west direction, and the second corridor extends in the north direction and is also lined with labs and offices. Inside walls were made of wallboard, outside walls were mainly glass. Ceilings and floors were reinforced concrete, with solid corrugated steel pour forms permanently in place beneath the floors and in the roof.

The transmitter was placed 21.4 m from the eastern end of the hallway and 60 cm

from the northern wall of the hallway, pointing west. The transmitter was kept at this location for all the hallway and lab measurements. For the lab measurements, the receiver was wheeled to the desired lab and was positioned 2.4 m north of the east-west line defined by the transmitter.

The data were transmitted in bursts of 100 symbols. In order to calculate the channel complex gains, the first 20 symbols of each burst were devoted to training. Since the transmitted signals are fully co-channel (all antennas transmit simultaneously within the same frequency band), the channel estimation was performed using orthogonal training sequences as suggested in [65]. After the receiver had learned the channel with the training process, the payload data (the last 80 symbols of each burst) were decoded using the V-BLAST algorithm, but we are interested here only in the channel properties as indicated in the measured channel transfer matrix.

The signal power was set to a sufficient value to guarantee a signal to noise ratio of at least 15 dB. This was done in order to guarantee the accuracy of the capacity calculation [47]. For each measurement location, about 100 bursts (100 separate measurements of the channel transfer matrix  $\mathbf{T}$ ) were recorded in order to average over the small scale temporal variation (doors opening and closing, people walking through the hallway or in the labs etc).

In order to estimate the receiver antenna correlation, the measurements were repeated with the receiver moved over a grid of 21 locations (in the hallway) or 33 locations (in the labs), with the points 15 cm from each other. The transmitter was not moved similarly, so transmitter correlations cannot be calculated.

The transmitter faced west in all the measurements, the receiver faced east for the hallway measurements, and it was placed at different directions for the room measurements.

# Chapter 7

## Conclusion

This thesis presents a propagation model for indoor hallways and urban streets that are bounded by tall buildings. The model analyzes these structures as waveguides, with theory adapted from fiber optic literature. The waveguide is multimoded and lossy and its walls are rough, so mode coupling is a key characteristic of the propagation model. The coupled mode theory constitutes a linear model and it renders predictions of power levels along the waveguide.

The distribution of power over the waveguide modes tends to a steady state distribution at sufficient distance from the source and from major disruptions of the waveguide (such as junctions). The steady state distribution of power has most of the power in the first (lowest order) transverse electric (TE) mode. The tendency of the power distribution to the steady state explains the change of power levels near junctions. When a receiver turns a corner and moves away from a power source, the power level it receives decreases rapidly, because of the re-distribution of power among the modes. The distribution of power starts with significant power in the high order modes at the junction, and tends to a steady state distribution further down the hallway/street.

The predictions of power level along indoor hallways were compared to measured levels in two office buildings. Power levels along four hallways in the Packard Building in Stanford (CA) were calculated with the same parameters used for all hallways and a uniform distribution of power over the modes at the junctions. The distribution of power over the modes at the transmitter location approximated a thin vertical antenna. Guidance of radiation by hallways was demonstrated by observing lower loss in the line

of sight hallway than the loss predicted in free space. Another indication of the guidance by hallways is the high power levels at hallway junctions, compared to nearby rooms.

Power levels measured in a hallway in an office building in Crawford Hill (NJ) also demonstrate the guiding effect of the hallway, as loss is lower than the predicted free space loss. The waveguide model predicts the measured power levels, where the parameters used for the calculation were similar to those used in the Packard Building in Stanford.

The theoretical calculation was also compared to measurements of power levels in urban areas in Ottawa, Canada and in Turin, Italy. The calculation matches the measured power levels in areas with tall buildings in both sides of the street. The model parameters were varied in different streets in order to improve the theoretical prediction. A uniform distribution of power over the modes was used as an initial condition in the junctions, and a thin vertical source was used as an initial condition in the transmitter location.

The model requires four input parameters:

- Dielectric constant  $\epsilon$ : low dielectric constants cause high loss and steep slopes in the graph of power vs. distance.
- Conductivity  $\sigma$ : high conductivities cause high loss and steep slopes in the graph of power vs. distance.
- Roughness  $s^2$ : large roughness causes high loss and steep slopes in the graph of power vs. distance.
- Correlation length  $D$ : large correlation lengths slow the coupling. The ‘knee’ in the power vs. distance graph occurs at greater distances from the junction for large correlation lengths.

The effect of decreasing  $\epsilon$ , increasing  $\sigma$  and increasing  $s^2$  are similar; these changes increase the loss in the waveguide.

Rooms beside the hallways in a big building receive power mostly by leakage from the hallway, if they are located at a sufficient distance from the transmitter. The room power levels are predicted from the waveguide model by considering the penetration of the different modes through the separating walls. The room power levels were calculated for the Packard Building and they match the measured levels near the line of sight

hallway. In other hallways the calculated power levels were lower than the measured levels.

The waveguide model for hallways and streets is useful in analyzing the delay profile in the indoor and urban settings. The delay spread is caused by the modal dispersion of the waveguide. Each mode carries power at a different speed, where the low order modes are faster than the high order modes. Combining this spread of velocities with the steady state distribution of power over the modes, the resulting delay profile is very asymmetric, with most of the power at the low delay and a ‘tail’ of lower power at higher delays, when the high order modes arrive. The resulting delay profile is very similar to the exponential form used in literature and to an empirical model based on measurements done in Tokyo, Japan. The theoretical delay spread is an upper bound because it is calculated for a waveguide with no mode coupling, where the power distribution over the modes is taken from the steady state of the waveguide with rough walls and mode coupling. The parameters used in the calculation differ from those used in the power prediction for Ottawa.

The waveguide model is also useful in explaining the reduction of channel capacity of a multiple antenna system along an indoor hallway or an urban street. Channel capacity is high where power is carried more or less uniformly by the waveguide modes. As power distribution tends to the steady state, with most of the power contained in the lowest order TE mode, capacity is reduced. The mechanism is an instance of a keyhole effect, where propagation conditions limit capacity despite low antenna correlations. Theoretically calculated capacities agree with the capacity estimated from multiple antenna measurements in an office building in Crawford Hill (NJ). The parameter values used for the theoretical prediction equal those used for the power level prediction in the Packard Building in Stanford (CA).

The waveguide model for hallways and streets focuses on the dominant propagation mechanisms in big buildings and the outdoor urban settings. It offers physical insight that is not available in ray tracing models, and relates measured properties of the radio channel to the physics of propagation. Other advantages of the waveguide model are its low computational complexity and the simplicity of the input it requires.

The model applies to a limited geometrical setting and it handles this setting effectively, with low computational complexity. It offers an alternative to ray tracing models,

that are very general and apply to any geometry, but are also complex and require considerable input data.

The waveguide model is useful at high frequencies, as long as the assumptions used for the development hold. The model is valid at a few giga-hertz for the indoor hallway case, where the dimensions of the hallways allow for a few tens of modes of each polarization, and the wall roughness is in the scale of a wavelength.

In the outdoor scenario, the model is useful below the UHF band. Above this band, it is not clear if the model holds, as the roughness of the walls and the obstacles in the waveguide are much larger (an order of magnitude or more) than the wavelength and the model assumptions no longer hold. A comparison of power measurements at different frequencies with the waveguide model is an interesting research possibility.

# Appendix A

## Stanford Measurement File Format

The measurement files are text files, which contain data in a matlab script format. They contain the location of the transmitting and receiving antennas (relative to point (0,0) in Figure 3.3), the date and time, some parameters of the spectrum analyzer and the received power vector, which contains 401 data points. Each measurement file can be called directly from matlab. An example of a measurement file follows:

```
% Base Location: C1
BaseLoc='C1'; % matlab
% Tx x (cm): 89
Txx=89; % matlab
% Tx y (cm): 1318
Txy=1318; % matlab
% Tx z (cm): 100
Txz=100; % matlab
% Tx Delta x (cm): 0.00
TxDx=0.00; % matlab
% Tx Delta y (cm): 0.00
TxDy=0.00; % matlab
% Rx x (cm): 28
Rxx=28; % matlab
% Rx y (cm): -1512
Rxy=-1512; % matlab
% Rx z (cm): 100
Rxz=100; % matlab
% Rx Delta x (cm): 5.08
RxDx=5.08; % matlab
```

```
% Rx Delta y (cm): 0.00
RxDy=0.00; % matlab
% Comment: cart at low x
comment='cart at low x'; % matlab
% Time: Mon Nov 26 13:41:38 2001
% Center Frequency (Hz): 900000000
cf=900000000; % center frequency matlab
% Sweep Time (sec): 33.333340
st=33.333340; % sweep time matlab
% Frequency Span (Hz): 100000000
sp=100000000; % frequency span matlab
% Start Frequency (Hz): 850000000
fa=850000000; % start frequency matlab
% Stop Frequency (Hz): 950000000
fb=950000000; % stop frequency matlab
% Resolution BW (Hz): 3000
rb=3000; % resolution bandwidth matlab
% Video BW (Hz): 3000
vb=3000; % video bandwidth matlab
% Reference Level (dBm): -30.00
rl=-30.00; % reference level matlab
% TG Power Level (dBm): 2.75
tgpl=2.75; % TG power level matlab
% TG Source Power Offset (dB): 0
tgspe=0; % TG source power offset matlab
% TG Source Power Attenuation (dB): 0
tgsat=0; % TG source power attenuation matlab
% TG ALC (INT/EXT): INT
tgalc='INT'; % TG ALC matlab
% TG Power Step Size (dB): 10.00
tgstp=10.00; % TG power step size matlab
% TG Power Sweep (dB): 0
tgswe=0; % TG power sweep matlab
% TG Power Tracking: 1072
tgtrk=1072; % TG power tracking matlab
% TG Coupling (SR/SA): SA
tgcpl='SA'; % TG coupling matlab
meas=[ % matlab
-47.71
```

```

-47.87
-48.22
-48.77
-44.83
.
.
.
-44.90
-45.04
]; % matlab

```

The parameter `BaseLoc` contains a fixed point in the basement (point (0,0) in Figure 3.3), which was used as a reference point for the locations. The locations of the transmitter and receiver are indicated in centimeters from the reference point.

A plot of the data contained in one measurement is shown in Figure A.1. This plot contains indications of the mean and median of the power level, in addition to the recorded data.

The matlab script used to generate this plot follows. The parameter `msrt` has to be set up before running this script in the following manner:

```
msrt='meas_R_p0028_n1512';
```

This parameter contains the measurement file name.

```

eval(msrt);
pwr=meas;
freq=fa:(fb-fa)/(length(meas)-1):fb;
figure(1)
pp=plot(freq/1e6,pwr);
med=median(pwr);
mn=mean(pwr);
l1=line([fa fb]/1e6, [med med]);
l2=line([fa fb]/1e6, [mn mn]);
set(l2, 'linestyle', '--');
grid on
tt=title(['Measured Power, file ' msrt '.m']);
set(tt, 'interpreter', 'none');
xx=xlabel('Frequency [MHz]');

```

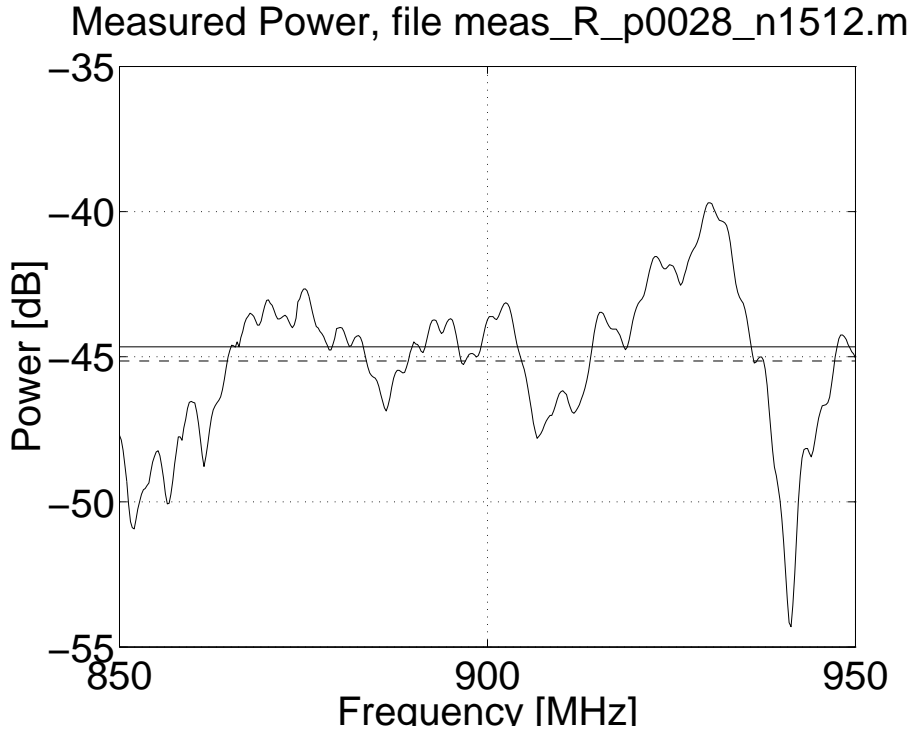


Figure A.1: A single measurement, the mean (-44.7 dB) is indicated in a dashed line and the median (-45.1 dB) in a full line.

```

yy=ylabel('Power [dB]');
aa=axis;
h_span=aa(2)-aa(1);
v_span=aa(4)-aa(3);
text(aa(1)+h_span/10, aa(3)+v_span/10, ...
['Median is ', num2str(med,3), ...
' dB, Mean is ' num2str(mn,3) ' dB.']);

```

## A.1 Measurement File Names

The measurement files are arranged in directories, where the directory name contains the date of the measurements, for example 11\_26\_2001. Many directories contain an explanation file called `exp.txt`. This file contains remarks on the measurement taken at the respective date.

Most of the measurement files have names which contain the location of the receiver, as in `meas_R_p0028_n1512.m`. The first number (here p0028) is the x coordinate, where p indicates a positive number and 0028 is the distance in centimeters from the reference point. The second number (here n1512) is the y coordinate, where n indicates a negative number and the units are centimeters from the reference point.

Some files have special names, in particular `cable_to_cable_before.m` and `cable_to_cable_after.m` contain a calibration measurement without the antennas. Notice that the tracking generator output level is lower than the usual in these measurement. This was necessary in order to avoid saturating the LNA. Such a measurement was taken in the beginning and end of each measurement session.

The files `close_antennas_before.m` and `close_antennas_after.m` contain a calibration measurement done with the antennas 39 cm apart. Such a measurement was taken in the beginning and end of each measurement session.

# Appendix B

## Matlab Code

The code shown below consists of two Matlab sources, that constitute the central part of the software used to calculate the results shown in the thesis. The function `lossy_wg4.m` receives the dimension and construction of a slab waveguide and returns the wave vectors and other characteristics of four modes (two TE and two TM modes). The script `pert_wg19.m` uses the output of `lossy_wg4.m` to calculate the distribution of power over the modes of the waveguide, where the walls are rough.

### B.1 `lossy_wg4.m`

```
function [h_TE_sym, h_TE_asym, h_TM_sym, h_TM_asym, ...
    u_TE_sym, u_TE_asym, u_TM_sym, u_TM_asym] ...
=lossy_wg4(epsilon, a, f, n)
% B. Adam and F. Knuebulhl 'Transversely Excited 337 um HCN
% Waveguide Laser', Applied Physics 8, 281-291 (1975)
% time convention is exp(-jwt)
% a is half the width of the waveguide

% The approximation here can be verified in lossy_TE3
% by calculating R^2
% from the approximated values and comparing to the
% true R^2 (calculated
% from material constants and geometry)
```

```

c=3e8; %m/s
epsilon0=8.85e-12; % F/m

w=2*pi*f;
lambda=c/f;
k=w/c;

epsilont=real(epsilon);
epsilontt=imag(epsilon); % under (16)

%TE (LSE)

%n=2;

eta_TE=epsilontt*lambda/(4*pi*a*(epsilont-1)^(3/2));

% symmetric
ut=pi*(1-eta_TE)*(n+1/2);
utt=-lambda/(2*a*(epsilont-1)^(1/2))*(n+1/2);
ht=sqrt((2*pi/lambda)^2-(ut/a)^2);
htt=lambda^2/(4*a^3*(epsilont-1)^(1/2))*(n+1/2)^2;
u=ut+j*utt; % under (16)
h_TE_sym=ht+j*htt; % above (21). these approximations
% are not always accurate
h_TE_sym=sqrt((2*pi/lambda)^2-(u/a)^2);
u_TE_sym=u;
q_TE_sym=u*tan(u);
%disp(['TE symmetric,      u=' num2str(u,'% .3g') 'h=' ...
%num2str(h_TE_sym,'% .3g') 'q=' num2str(q_TE_sym, '% .3g') ]);

%disp(['P(x>a)/P(x<a)= ' ...
%num2str(-(ut^2+k^2*epsilon*a^2)/ut/(ut^2-k^2*a^2))]);

% antisymmetric
ut=pi*(1-eta_TE)*(n+1);
utt=-lambda/(2*a*(epsilont-1)^(1/2))*(n+1);
ht=sqrt((2*pi/lambda)^2-(ut/a)^2);
htt=lambda^2/(4*a^3*(epsilont-1)^(1/2))*(n+1)^2;
u=ut+j*utt; % under (16)

```

```

h_TE_asym=ht+j*htt; % above (21)
h_TE_asym=sqrt((2*pi/lambda)^2-(u/a)^2);
u_TE_asym=u;
q_TE_asym=-u*cot(u);
%disp(['TE antisymmetric, u=' num2str(u,'%3g') 'h=' ...
%num2str(h_TE_asym,'%3g') 'q=' num2str(q_TE_asym, '%3g') ]);

% TM (LSM)

eta_TM=(epsilont+2*pi*a/lambda*epsilontt* ...
(epsilont-1)^(1/2))/ ...
((2*pi*a/lambda)^2*(epsilont-1));

% symmetric
ut=pi*(1-eta_TM)*(n+1);
utt=-epsilont*lambda/(2*a*(epsilont-1)^(1/2))*(n+1);
ht=sqrt((2*pi/lambda)^2-(ut/a)^2);
htt=lambda^2/(4*a^3*(epsilont-1)^(1/2))*(n+1/2)^2;
u=ut+j*utt; % under (16)
h_TM_sym=ht+j*htt; % above (21)
h_TM_sym=sqrt((2*pi/lambda)^2-(u/a)^2);
u_TM_sym=u;
q_TM_sym=-epsilon*u*cot(u);
%disp(['TM symmetric, u=' num2str(u,'%3g') 'h=' ...
%num2str(h_TM_sym,'%3g') 'q=' num2str(q_TM_sym, '%3g') ]);

% antisymmetric
ut=pi*(1-eta_TM)*(n+1/2);
utt=-epsilont*lambda/(2*a*(epsilont-1)^(1/2))*(n+1/2);
ht=sqrt((2*pi/lambda)^2-(ut/a)^2);
htt=lambda^2/(4*a^3*(epsilont-1)^(1/2))*(n+1)^2;
u=ut+j*utt; % under (16)
h_TM_asym=ht+j*htt; % above (21)
h_TM_asym=sqrt((2*pi/lambda)^2-(u/a)^2);
u_TM_asym=u;
q_TM_asym=epsilon*u*tan(u);
%disp(['TM antisymmetric, u=' num2str(u,'%3g') 'h=' ...
%num2str(h_TM_asym,'%3g') 'q=' num2str(q_TM_asym, '%3g') ]);
%disp(' ');

```

## B.2 pert\_wg19.m

```

% pert_wg.m
% perturbed two dimensional waveguide, hollow
% with lossy walls.
% Similar to D. Marcuse 'Power Distribution and Radiation
% Losses in
% Multimode Dielectric Slab Waveguides' The BSTJ,
% February 1972, p 429-454.

% This includes the TM 0th mode (TEM) with zero loss.

% pert_wg16 addition - penetration into side rooms.

% ground reflection is controled by
% the parameter GROUND_REFLECTION

% pert_wg19 reflection coefficient -1 instead of 1.

% disp(['pert_wg19, WITH_TM=' num2str(WITH_TM)]);
% disp(['pert_wg19, GROUND_REFLECTION=' ...
% num2str(GROUND_REFLECTION)]);

% constants
c=3e8; %m/s
epsilon0=8.85e-12; % F/m
mu0=4*pi*1e-7;
Z0=sqrt(mu0/epsilon0);

% frequency
w=2*pi*f;
lambda=c/f;
k=w/c;

% walls
epsilon_w=epsilon_r_w+j*sigma_w/w/epsilon0;
% for the time convention e(-jwt)
% used in lossy_wg4
epsilon_t_w=real(epsilon_w);

```

```

epsilon_tt_w=imag(epsilon_w); % under (16)
n_w=sqrt(epsilon_w);

sigma=sqrt(sigma_bar_2);

aa_TE=zeros(N_max,3);
ut_TE=zeros(1,N_max);
utt_TE=zeros(1,N_max);
beta_TE=zeros(1,N_max);
aa_TM=zeros(N_max,3);
ut_TM=zeros(1,N_max);
utt_TM=zeros(1,N_max);
beta_TM=zeros(1,N_max);
% TM 0th mode (TEM) missing
for nn=0:N_max/2-1
[h_TE_sym, h_TE_asym, h_TM_sym, h_TM_asym ...
 u_TE_sym, u_TE_asym, u_TM_sym, u_TM_asym] ...
=lossy_wg4(epsilon_w, d, f, nn);
% d is half the width of the waveguide
beta_TE(2*nn+1)=real(h_TE_sym); % even modes
beta_TE(2*nn+2)=real(h_TE_asym); % odd modes
beta_TM(2*nn+3)=real(h_TM_sym); % even modes
beta_TM(2*nn+2)=real(h_TM_asym); % odd modes

ut_TE(2*nn+1)=real(u_TE_sym); % TE sym
ut_TE(2*nn+2)=real(u_TE_asym); % TE asym
ut_TM(2*nn+3)=real(u_TM_sym); % TM sym
ut_TM(2*nn+2)=real(u_TM_asym); % TM asym

utt_TE(2*nn+1)=imag(u_TE_sym); % even modes
utt_TE(2*nn+2)=imag(u_TE_asym); % odd modes
utt_TM(2*nn+3)=imag(u_TM_sym); % even modes
utt_TM(2*nn+2)=imag(u_TM_asym); % odd modes

aa_TE(2*nn+1,1)=cos(ut_TE(2*nn+1)*(d-0.2*sigma)/d);
aa_TE(2*nn+1,2)=cos(ut_TE(2*nn+1)*(d+0.0*sigma)/d); % TE sym
aa_TE(2*nn+1,3)=cos(ut_TE(2*nn+1)*(d+0.2*sigma)/d);
aa_TE(2*nn+2,1)=sin(ut_TE(2*nn+2)*(d-0.2*sigma)/d);
aa_TE(2*nn+2,2)=sin(ut_TE(2*nn+2)*(d+0.0*sigma)/d); % TE asym

```

```

aa_TE(2*nn+2,3)=sin(ut_TE(2*nn+2)*(d+0.2*sigma)/d);

if 0 %???
% H field shape near boundaries
aa_TM(2*nn+3,1)=cos(ut_TM(2*nn+3)*(d-0.2*sigma)/d);
aa_TM(2*nn+3,2)=cos(ut_TM(2*nn+3)*(d+0.0*sigma)/d); % TM sym
aa_TM(2*nn+3,3)=cos(ut_TM(2*nn+3)*(d+0.2*sigma)/d);
aa_TM(2*nn+2,1)=sin(ut_TM(2*nn+2)*(d-0.2*sigma)/d);
aa_TM(2*nn+2,2)=sin(ut_TM(2*nn+2)*(d+0.0*sigma)/d); % TM asym
aa_TM(2*nn+2,3)=sin(ut_TM(2*nn+2)*(d+0.2*sigma)/d);
end;

if 1
% E field shape near boundaries -
% should be used for coupling coefficeints
aa_TM(2*nn+3,1)=sin(ut_TM(2*nn+3)*(d-0.2*sigma)/d);
aa_TM(2*nn+3,2)=sin(ut_TM(2*nn+3)*(d+0.0*sigma)/d); % TM sym
aa_TM(2*nn+3,3)=sin(ut_TM(2*nn+3)*(d+0.2*sigma)/d);
aa_TM(2*nn+2,1)=cos(ut_TM(2*nn+2)*(d-0.2*sigma)/d);
aa_TM(2*nn+2,2)=cos(ut_TM(2*nn+2)*(d+0.0*sigma)/d); % TM asym
aa_TM(2*nn+2,3)=cos(ut_TM(2*nn+2)*(d+0.2*sigma)/d);
end; % if 1
end;

N_TE=sum(ut_TE<k*d);
N_TM= sum(ut_TM<k*d);
% consider only propagating modes (with ut<k*d)
%N_TM=2;

if WITH_TM
N=N_TE+N_TM-1; % ???
else
N=N_TE;
end;
% disp(['N_TE=' num2str(N_TE)]);
% disp(['N_TM=' num2str(N_TM)]);
% disp(['N=' num2str(N)]);

alpha_TE=NaN*ones(1,N_TE);

```

```

alpha_TM=NaN*ones(1,N_TM-1);
for nn=0:2:N_TE-1 % even modes
alpha_TE(nn+1)=lambda^2/2/d^3/sqrt(epsilont_w-1)...
*(nn/2 +1/2)^2;
end;
for mm=2:2:N_TM-1 % even modes
alpha_TM(mm)=lambda^2/2/d^3*epsilont_w...
/sqrt(epsilont_w-1)*(mm/2)^2;
end;

for nn=1:2:N_TE-1 % odd modes
alpha_TE(nn+1)=lambda^2/2/d^3/ ...
sqrt(epsilont_w-1)*((nn-1)/2+1 )^2;
end;
for mm=1:2:N_TM-1 % odd modes
alpha_TM(mm)=lambda^2/2/d^3*epsilont_w...
/sqrt(epsilont_w-1)*(mm/2)^2;
end;

%??? makes a big difference - mm^2 instead of (mm/2)^2
%for mm=2:2:N_TM-1 % even modes
% alpha_TM(mm)=lambda^2/2/d^3...
% *epsilont_w/sqrt(epsilont_w-1)*(mm)^2;
%end;
%for mm=1:2:N_TM-1 % odd modes
% alpha_TM(mm)=lambda^2/2/d^3...
% *epsilont_w/sqrt(epsilont_w-1)*(mm)^2;
%end;
%???

if WITH_TM
alpha=[alpha_TE alpha_TM];
else
alpha=alpha_TE;
end;

alpha=loss_fact*alpha; %???

if WITH_TM

```

```

K_2=zeros(N,N);
P_mat=zeros(N,N);
else
K_2=zeros(N,N);
P_mat=zeros(N,N);
end;

for nn=0:N_TE-1
for mm=0:N_TE-1
% In the calculation of K_2, average over the coupline
% between the modes at x=d and near it.
% This averaging prevents the situation where certain
% modes have no coupling, because their fields equal
% zero at x=d.

% TE to TE coupling
K_2(nn+1, mm+1)= ...
abs(epsilon_w-1)^2 ...
*k^4/d^2/4 ...
/beta_TE(nn+1) ...
/beta_TE(mm+1) ...
*aa_TE(nn+1,2)^2 *aa_TE(mm+1,2)^2;

%*aa_TE(nn+1,2)^2 *aa_TE(mm+1,2)^2;

% average cos term instead of taking it at x=d:
%*(0.25*aa_TE(nn+1,1)*aa_TE(mm+1,1) ...
%+0.5*aa_TE(nn+1,2)*aa_TE(mm+1,2) ...
%+0.25*aa_TE(nn+1,3)*aa_TE(mm+1,3))^2;

P_mat(nn+1,mm+1)=sqrt(pi)*2*sigma_bar_2*D ...
*K_2(nn+1,mm+1) ...
*exp(-(D/2*(beta_TE(nn+1)-beta_TE(mm+1)))^2);
end;
end;

if WITH_TM
for nn=1:N_TM-1
for mm=1:N_TM-1

```

```

% TM to TM coupling
K_2(N_TE+nn, N_TE+mm)= ...
abs(epsilon_w-1)^2 ...
*k^4/d^2/4 ...
/beta_TM(nn+1) ...
/beta_TM(mm+1) ...
*aa_TM(nn+1,2)^2 *aa_TM(mm+1,2)^2;

%*aa_TM(nn+1,2)^2 *aa_TM(mm+1,2)^2;

% average cos term instead of taking it at x=d:
%*(0.25*aa_TM(nn+1,1) *aa_TM(mm+1,1) ...
%+0.5*aa_TM(nn+1,2) *aa_TM(mm+1,2) ...
%+0.25*aa_TM(nn+1,3) *aa_TM(mm+1,3))^2;

P_mat(N_TE+nn,N_TE+mm)=sqrt(pi)*2*sigma_bar_2*D ...
*K_2(N_TE+nn,N_TE+mm) ...
*exp(-(D/2*(beta_TM(nn+1)-beta_TM(mm+1)))^2);
end;
end;

for nn=0:N_TE-1
for mm=1:N_TM-1
% TE to TM coupling
K_2(nn+1, N_TE+mm)= ...
abs(epsilon_w-1)^2 ...
*k^4/d^2/4 ...
/beta_TE(nn+1) ...
/beta_TM(mm+1) ...
*aa_TE(nn+1,2)^2 *aa_TM(mm+1,2)^2;

%*aa_TE(nn+1,2)^2 *aa_TM(mm+1,2)^2;

% average cos term instead of taking it at x=d:
%*(0.25*aa_TE(nn+1,1) *aa_TM(mm+1,1) ...
%+0.5*aa_TE(nn+1,2) *aa_TM(mm+1,2) ...
%+0.25*aa_TE(nn+1,3) *aa_TM(mm+1,3))^2;

% K_2(nn+1, N_TE+mm)=10*K_2(nn+1, N_TE+mm); % ???

```

```

P_mat(nn+1,N_TE+mm)=sqrt(pi)*2*sigma_bar_2*D ...
*K_2(nn+1,N_TE+mm) ...
*exp(-(D/2*(beta_TE(nn+1)-beta_TM(mm+1)))^2);
end;
end;

for nn=1:N_TM-1
for mm=0:N_TE-1

% TM to TE coupling
K_2(N_TE+nn, mm+1)= ...
abs(epsilon_w-1)^2 ...
*k^4/d^2/4 ...
/beta_TM(nn+1) ...
/beta_TE(mm+1) ...
*aa_TM(nn+1,2)^2 *aa_TE(mm+1,2)^2;

%*aa_TM(nn+1,2)^2 *aa_TE(mm+1,2)^2;

% average cos term instead of taking it at x=d:
%*(0.25*aa_TM(nn+1,1) *aa_TE(mm+1,1) ...
%+0.5*aa_TM(nn+1,2) *aa_TE(mm+1,2) ...
%+0.25*aa_TM(nn+1,3) *aa_TE(mm+1,3))^2;

% K_2(N_TE+nn, mm+1)=10*K_2(N_TE+nn, mm+1); % ???

P_mat(N_TE+nn,mm+1)=sqrt(pi)*2*sigma_bar_2*D ...
*K_2(N_TE+nn,mm+1) ...
*exp(-(D/2*(beta_TM(nn+1)-beta_TE(mm+1)))^2);
end;
end;
end; % if WITH_TM

if WITH_TM
P_mat=P_mat.*(ones(N,N)-eye(N)); % zero diagonal
else
P_mat=P_mat.*(ones(N,N)-eye(N)); % zero diagonal
end

```

```

P_mat=coupling_fact*P_mat;

b=sum(P_mat,2).';
P_mat=P_mat+diag(-(alpha+b));

if STEADY_STATE % steady state

[V,lambda_P]=eig(P_mat);
lambda_P=-diag(lambda_P); % because we want
% -alpha(i)*P=P_mat*P

[alpha_P, ii]=min(lambda_P);
B=V(:,ii);
B=B*sign(B(1)); %???
% disp(['steady state power decrease = ' ...
% num2str(alpha_P) ' Nieper/m = ' ...
% num2str(10*alpha_P/log(10)*1000) ' dB/km']);

if 0 % plot steady state
figure
plot(10*log10(B(1:N_TE)),'-');
hold on
if N_TM~=0
plot(10*log10(B(N_TE+1:N_TE+N_TM-1)), '-r');
end;
grid on;
title('Power of modes');
ylabel('P (dB)');
xlabel('n');
aax=axis;
text(1+N_TE/10, aax(4)-0.05*(aax(4)-aax(3)), [ ...
'D=' num2str(D,'% .3g') ' m' ...
', \sigma^2=' num2str(sigma_bar_2,'% .3g') ' m^2' ...
', \lambda=' num2str(lambda,'% .3g') ' m' ...
', d=' num2str(d,'% .3g') ' m' ...
', N_{TE}=' num2str(N_TE,'% .3g') ...
', N_{TM}=' num2str(N_TM,'% .3g') ...
', \sigma_w=' num2str(sigma_w,'% .3g') ' S/m' ...
', \epsilon_{r_w}=' num2str(epsilon_r_w,'% .3g')]);

```

```

[handle, obj]=legend('TE modes', 'TM modes', 0);
aab=get(handle, 'Position');
aab(2)=aab(2)-0.1;
set(handle, 'Position', aab);
hold off;

end; % if plot steady state
end; % if STEADY_STATE

% ----- transmission through walls
transmission_coef=zeros(N,1);
% transmission coefficients through
% walls into side rooms.

% epsilon_rw=3.3; % relative
% sigma_w=0.08; % S/m
% f=910e6; % Hz
% epsilon0=8.85e-12; % F/m
% mu0=4*pi*1e-7; % H/m

% w=2*pi*f;
% epsilon_w=epsilon_rw*epsilon0;

% eta0=sqrt(mu0/epsilon0);
k0=w*sqrt(epsilon0*mu0);
l=9.5e-3; % slab thickness (m)
% disp(['l=' num2str(l/1e-3) 'mm']);
% disp(['n_w=' num2str(n_w)]);

epsilon_rc=epsilon_rw-j*sigma_w/w/epsilon0; % for the
% time convention e(+jwt)
% epsilon_rc=epsilon_rw-j*sigma_w/w/epsilon0;
se=sqrt(epsilon_rc);

t=4*se*exp(-j*2*k0*(se-1)*l)...
/((se+1)^2-(1-se)^2*exp(-j*2*k0*se*l));

% t=4*n_w*exp(-j*2*k0*(n_w-1)*l)/ ...
% ((n_w+1)^2-(1-n_w)^2*exp(-j*2*k0*n_w*l));

```

```

T=abs(t)^2;
% disp(['Power transmission coefficient T=' num2str(T,2) ...
% '=' num2str(T*100,3) '% =' num2str(10*log10(T),2) ' dB']);

% approximation for normal incidence:
% transmission_coef=ones(N,1)*T;

% approximation - normal incidence with
% cos correction (no explanation
% for this correction)
% transmission_coef_TE=sin(pi/2*(1:N_TE)/N_TE)*T;
% transmission_coef_TM=sin(pi/2*(1:(N_TM-1))/(N_TM-1))*T;

% ??? approximation of transmission coefficeints of modes
% this approximation simply 2 incidences on infinite material
% without considering the thickness of the slab.
eta1=sqrt(mu0/epsilon0);
eta2=sqrt(mu0/epsilon0)/n_w;
cos_t1_TE=ut_TE(1:N_TE)/k0;
cos_t1_TM=ut_TM(2:N_TM)/k0;
sin_t2_TE=real(n_w)*sqrt(1-cos_t1_TE.^2);
sin_t2_TM=real(n_w)*sqrt(1-cos_t1_TM.^2);
cos_t2_TE=sqrt(1-sin_t2_TE).^2;
cos_t2_TM=sqrt(1-sin_t2_TM).^2;

transmission_coef_TE=abs((2*eta2*cos_t1_TE./...
(eta2*cos_t1_TE+eta1*cos_t2_TE)).^2*eta1/eta2);
transmission_coef_TE(find(sin_t2_TE>1))=0;
transmission_coef_TM=abs((2*eta2*cos_t1_TM./...
(eta2*cos_t2_TM+eta1*cos_t1_TM)).^2*eta1/eta2);
transmission_coef_TM(find(sin_t2_TM>1))=0;

if WITH_TM
transmission_coef=[transmission_coef_TE transmission_coef_TM];
else
transmission_coef=transmission_coef_TE;
end;

% ----- end calculation of transmission coefficient

```

```

if DYNAMIC_SOLUTION; % dynamic solution
% The dynamic solution of the matrix differential
% equation for P
% works if deltaZ is small enough. If manymodes are
% takes into account,
% deltaZ should be small.
% The dynamic solution converges to the eigen power
% distribution. I tried
% a few initial conditions.
P=zeros(N, 1); % initialization
if (initial_dist==0)
% disp('User supplied initial conditions');
P(1:length(modal_coef))=(abs(modal_coef)).^2;
else % fixed initial conditions
P=ones(N,1); % uniform distribution (default)
if (strcmp(GetIPD(initial_dist),'lowest'))
P(:)=0;
P(1)=1;
P(N_TE+1)=1;
end;
if (strcmp(GetIPD(initial_dist),'highest'))
P(:)=0;
P(N_TE)=1;
P(N-1)=1;
end;
if (strcmp(GetIPD(initial_dist),'high order'))
P(:)=0;
P(round(N_TE/2):N_TE)=round(N_TE/2):N_TE;
if WITH_TM
P(N_TE+round(N_TM/2):N)=round(N_TM/2):N_TM-1;
end;
end;
if (strcmp(GetIPD(initial_dist),'low order'))
P(:)=0;
P(1:round(N_TE/2))=1;
if WITH_TM
P(N_TE+1:N_TE+round(N_TM/2))=1;
end;
end;

```

```

end;
if (strcmp(GetIPD(initial_dist),'TEdelta'))
P(:)=0;
P(1:2:N_TE)=1;
end;
if (strcmp(GetIPD(initial_dist),'TMdelta'))
P(:)=0;
P(N_TE+(1:2:N_TE))=1;
end;
if (strcmp(GetIPD(initial_dist),'Special'))
% mixture of uniform and high order
P=N_TE*ones(N,1).'; % uniform distribution
P(round(N_TE/2):N_TE)= P(round(N_TE/2):N_TE)...
+(round(N_TE/2):N_TE);
if WITH_TM
P(N_TE+round(N_TM/2):N)=P(N_TE+round(N_TM/2):N)+...
(round(N_TM/2):N_TM-1);
end;
P=P.';
end;
P=P/sum(P)*initial_power;
end; % if initial cond ~= 0

tempP=eye(size(P_mat))+P_mat*deltaZ;
MP_mat=tempP^dZm;

%disp(['firstZ=' num2str(firstZ)]);
%disp(['dZm*deltaZ=' num2str(dZm*deltaZ)]);
%disp(['lastZ=' num2str(lastZ)]);
clear z;
z=firstZ:round(100*dZm*deltaZ)/100:lastZ+dZm*deltaZ/10;
%disp(['length(z)= ' num2str(length(z))]);
total_P=[];
P_side=[]; % P_side is the total power in the side rooms

if WITH_TM
beta=[beta_TE(1:N_TE) beta_TM(2:N_TM)];
else
beta=beta_TE(1:N_TE);

```

```

end;

u=[ut_TE(1:N_TE)+j*utt_TE(1:N_TE) ...
  ut_TM(2:N_TM)+j*utt_TM(2:N_TM)];
for ii=1:length(z)
  if (GROUND_REFLECTION==0)
    total_P(ii)=sum(P);
    P_side(ii)=sum(P.*transmission_coef. ');
  end;
  if (GROUND_REFLECTION==1)
    direct_dd=sqrt((ht-hr)^2+z(ii)^2);
    ref_z=z(ii)*ht/(ht+hr);
    ref_dd=sqrt(ht^2+ref_z^2)+sqrt(hr^2+(z(ii)-ref_z)^2);
    delta_dd=ref_dd-direct_dd;
    % coherent addition of direct and reflected ray:
    % power_mult=(abs(1- ...
    % exp(j*beta*delta_dd).*exp(-alpha*delta_dd))).^2;
    % incoherent addition of direct and reflected ray:
    power_mult=1- ...
    (abs(exp(j*beta*delta_dd).*exp(-alpha*delta_dd))).^2;
    total_P(ii)=sum(P.*power_mult. ');
    P_side(ii)=sum(P.*power_mult. '.*transmission_coef. ');
  end; % if GROUND_REFLECTION
  P=MP_mat*P;
  if 0
    if (z(ii)/50==round(z(ii)/50)) % plot every 50 m
      plot(P(1:N_TE));
      hold on
      plot(P(N_TE+1:N_TE+N_TM-1), 'r');
      hold off
      legend('TE', 'TM');
      grid on;
      xlabel('mode #');
      ylabel('P [w]');
      title(['z=' num2str(z(ii)) ' m']);
      drawnow;
      disp(['pausing, z=' num2str(z(ii)) ' m']);
      pause;
    end;
  end;

```

```
end; % if 0
end; % for loop on z
%disp(['size(total_P)= ' num2str(size(total_P))]);

if 0
figure(1)
hold off
plot(total_P)
title('total_P')
end; % if 0

end; % if DYNAMIC_SOLUTION

if 0 & DYNAMIC_SOLUTION & STEADY_STATE % compare steady state
% and dynamic state
disp('Power in lowest TE modes:');
disp(['P(2)/P(1) in the steady state = ' num2str(B(2)/B(1))]);
disp(['At z=' num2str(z(length(z))) ' m, P(2)/P(1)= ' ...
      num2str(P(2)/P(1))]);

disp(['P(3)/P(1) in the steady state = ' num2str(B(3)/B(1))]);
disp(['At z=' num2str(z(length(z))) ' m, P(3)/P(1)= ' ...
      num2str(P(3)/P(1))]);
end; % if DYNAMIC_SOLUTION & STEADY_STATE
```

# Bibliography

- [1] B. Adam and F. Kneubühl. Transversely excited 337  $\mu\text{m}$  HCN waveguide laser. *Appl. Phys.*, 8(4):281–291, December 1975.
- [2] H. W. Arnold, R. R. Murray, and D. C. Cox. 815 MHz radio attenuation measured within two commercial buildings. *IEEE Transactions on Antennas and Propagation*, 37(10):1335–1339, October 1989.
- [3] M. Barbiroli, V. Degli Eposti, and P. Grazioso. Extraction of a simplified model for street corner loss in microcells from ray-tracing simulation. *Wireless Personal Communications*, 12:225–237, 2000.
- [4] H. L. Bertoni. *Radio propagation for modern wireless systems*. Prentice Hall, 2000.
- [5] H. L. Bertoni, W. Honcharenko, L. R. Maciel, and H. H. Xia. UHF propagation prediction for wireless personal communications. *Proceedings of the IEEE*, 82(9):1333–1359, September 1994.
- [6] N. Blaunstein. Average field attenuation in the nonregular impedance street waveguide. *IEEE Transactions on Antennas and Propagation*, 46(12):1782–1789, December 1998.
- [7] N. Blaunstein. *Radio Propagation in Cellular Networks*. Artech House, 2000.
- [8] N. Blaunstein, R. Giladi, and M. Levin. Unified approach to predicting cellular characteristics in urban environments with rectangular grid-plan streets. *Radio Science*, 34(5):1085–1102, September–October 1999.

- [9] N. Blaunstein and M. Levin. Propagation loss prediction in the urban environment with rectangular grid plan streets. *Radio Science*, 32(2):453–467, March-April 1997.
- [10] J. J. Burke. Propagation constants of resonant waves on homogeneous, isotropic slab waveguides. *Applied Optics*, 9(11):2444–2452, November 1970.
- [11] G. Cancellieri and P. Fantini. Mode coupling effects in optical fibres: perturbative solution of the time-dependent power flow equation. *Optical and Quantum Electronics*, 15:119–136, 1983.
- [12] S. T. S. Chia, R. Steele, E. Green, and A. Baran. Propagation and bit error ratio measurements for a microcellular system. *Journal of the Institution of Electronic and Radio Engineers*, 57(6):S255–S266, November/December 1987.
- [13] D. Chizhik, G. J. Foschini, M. J. Gans, and R. A. Valenzuela. Keyholes, correlations and capacities of multi-element transmit and receive antennas. In *Vehicular Technology Conference*, volume 1, pages 284–287, 2001 Spring.
- [14] D. J. Cichon, T. C. Becker, and M. Döttling. Ray optical prediction of outdoor and indoor coverage in urban macro- and micro-cells. In *46th Vehicular Technology Conference*, volume 1, pages 41–45. IEEE, 1996.
- [15] D. C. Cox, 2002. Data Provided by D. C. Cox.
- [16] D. C. Cox, R. R. Murray, and A. W. Norris. 800-MHz attenuation measured in and around suburban houses. *AT&T Bell Laboratories Technical Journal*, 63(6):921–954, July-August 1984.
- [17] B. Crosignani, C. H. Papas, and P. Di Porto. Theory of time-dependent propagation in mulitmode lightguides. *Journal of the Optical Society of America*, 67(10):1300–1307, October 1977.
- [18] P. Degauque, S. Kyheng, and B. Demoulin. Mobile radiocommunication in tunnels. In *Melecom, Mediterranean Electrotechnical Conference*, pages 145–148, 1987.

- [19] V. Degli-Esposti and H. L. Bertoni. Evaluation of the role of diffuse scattering in urban microcellular propagation. In *Vehicular Technology Conference*, pages 1392–6. IEEE, 1999 Fall.
- [20] V. Degli-Esposti, H. El-Sallabi, D. Guideccu, K. Kalliola, P. Azzi, L. Vuokko, J. Kivinen, and P. Vainikainen. Analysis and simulation of the diffuse scattering phenomenon in urban environments. In *XXVII General Assembly*. URSI, 2002.
- [21] J. J. Degnan. The waveguide laser: A review. *Applied Physics*, 11(1):1–33, September 1976.
- [22] U. Dersch and E. Zollinger. Propagation mechanisms in microcell and indoor environment. *IEEE Transactions on Vehicular Technology*, 43(4):1058–1066, November 1994.
- [23] D. M. J. Devasirvatham. A comparison of time delay spread and signal level measurements within two dissimilar office buildings. *Transactions on Antennas and Propagation*, 35(3), March 1987.
- [24] H.M. El-Sallabi, G. Liang, H.L. Bertony, and P. Vainikainen. Influence of diffraction coefficient on ray prediction of power and delay spread in urban microcells. In *Vehicular Technology Conference*. IEEE, 2002 Spring.
- [25] A. G. Emslie, R. L. Lagace, and P. F. Strong. Theory of the propagation of UHF radio waves in coal mine tunnels. *IEEE Transactions on Antennas and Propagation*, AP-23(2):192–205, March 1975.
- [26] V. Erceg, S. J. Fortune, J. Ling, A. J. Rustako, and R. A. Valenzuela. Comparisons of a computer-based propagation prediction tool with experimental data collected in urban microcellular environments. *IEEE Journal on Selected Areas in Communications*, pages 677–684, May 1997.
- [27] V. Erceg, S. Ghassemzadeh, M. Taylor, D. Li, and D. L. Schilling. Urban/suburban out-of-sight propagation modeling. *IEEE Communications Magazine*, pages 56–61, June 1992.

- [28] V. Erceg, L. J. Greenstein, S. Y. Tjandra, S. R. Parkoff, A. Gupta, B. Kulic, A. A. Julius, and R. Bianchi. An empirically based path loss model for wireless channels in suburban environment. *IEEE Journal on Selected Areas in Communications*, pages 1205–1211, July 1999.
- [29] V. Erceg, J. Rustako, and R.S. Roman. Diffraction around corners and its effects on the microcell coverage area in urban and suburban environments at 900 MHz, 2 GHz, and 6 GHz. *IEEE Transactions on Vehicular Technology*, pages 762–6, August 1994.
- [30] V. Erceg, D. L. Schilling, S. Ghassemzadeh, D. Li, and M. Taylor. Propagation modeling and measurements in an urban and suburban environment using broadband direct sequence spread spectrum. In *42nd Vehicular Technology Conference*, volume 1, pages 317–320. IEEE, 1992.
- [31] G. J. Foschini and M. J. Gans. On limits of wireless communications in a fading environment when using multiple antennas. *Wireless Personal Communications*, 6(3):311–335, March 1998.
- [32] K. Fujimori and H. Arai. Ray tracing analysis of propagation characteristics in tunnels including transmitting antenna. In *Antennas and Propagation Society International Symposium*, volume 2, pages 1222–5, 1996.
- [33] D. Gesbert, H. Bölcskei, and A. Paulraj. MIMO wireless channels: Capacity and performance prediction. In *Global Telecommunications Conference*, volume 2, pages 1083–1088. IEEE, 2000.
- [34] D. G. Hall. In-phase scattering in planar optical waveguides: refractive-index fluctuations and surface roughness. *Journal of the Optical Society of America A*, 2(5):747–752, May 1985.
- [35] D. Har, H. H. Xia, and H. L. Bertoni. Path-loss prediction model for microcells. *IEEE Transactions on Vehicular Technology*, 48(5):1453–1462, September 1999.
- [36] S. Ichitsubo, T. Furuno, and R. Kawasaki. A statistical model for microcellular multipath propagation environment. In *47th Vehicular Technology Conference*. IEEE, 1997.

- [37] A. Ishimaru. *Wave Propagation and Scattering in Random Media*. Academic Press, 1978. Chapter 21.
- [38] W. C. Jakes. *Microwave Mobile Communications*. IEEE, 1974. IEEE reprint edition, originally published by Wiley.
- [39] S. Kim, B. Bougerolles, and H. L. Bertoni. Transmission and reflection properties of interior walls. In *International Conference on Personal Communications*. IEEE, September 1994.
- [40] S.-C. Kim, B. J. Guarino Jr., T. M. Willis III, V. Erceg, S. J. Fortune, R. A. Valenzuela, L. W. Thomas, J. Ling, and J. D. Moore. Radio propagation measurements and prediction using three-dimensional ray tracing in urban environments at 908 MHz and 1.9 GHz. *IEEE Transactions on Vehicular Technology*, 48(3):931–946, May 1999.
- [41] J. Kivinen, X. Zhao, and P. Vainikainen. Empirical characterization of wideband indoor radio channel at 5.3 GHz. *IEEE Transactions on Antennas and Propagation*, 49(8):1192–1203, August 2001.
- [42] W. E. Kohler. Propagation in a randomly perturbed multimode matched waveguide. *Wave Motion*, 4:243–263, 1982.
- [43] H. Krammer. Field configurations and propagation constants of modes in hollow rectangular dielectric waveguides. *IEEE Journal of Quantum Electronics*, pages 505–507, August 1976.
- [44] P. Kreuzgruber, T. Brijndl, W. Kuran, and R. Gahleitner. Prediction of indoor radio propagation with the ray splitting model including edge diffraction and rough scattering. In *44th Vehicular Technology Conference*, volume 2, pages 878–882. IEEE, 1994.
- [45] P. Kyritsi. *Multiple Element Antenna Systems in an Indoor Environment*. PhD thesis, Stanford University, 2001.
- [46] P. Kyritsi and D. C. Cox. Modal analysis of MIMO capacity in a hallway. In *Global Telecommunications Conference*, volume 1, pages 567–571. IEEE, 2001.

- [47] P. Kyritsi, R.A. Valenzuela, and D.C. Cox. Effect of channel estimation on the accuracy of capacity estimation. In *Vehicular Technology Conference*, Rhodes, Greece, May 2001. IEEE.
- [48] K. D. Laakmann and W. H. Steier. Waveguides: characteristic modes of hollow rectangular dielectric waveguides. *Applied Optics*, 15(5):1334–1340, May 1976.
- [49] O. Landron, M. J. Feuerstein, and T. S. Rappaport. In situ microwave reflection coefficient measurements for smooth and rough exterior wall surfaces. In *43rd Vehicular Technology Conference*, pages 77–80. IEEE, 1993.
- [50] O. Landron, M. J. Feuerstein, and T. S. Rappaport. A comparison of theoretical and empirical reflection coefficients for typical exterior wall surfaces in a mobile radio environment. *IEEE Transactions on Antennas and Propagation*, 44(3):341–351, March 1996. Table I.
- [51] J. Laurila, K. Kalliola, M. Toeltsch, K. Hugl, P. Vainikainen, and E. Bonek. Wideband 3-D characterization of mobile radio channels in urban environment. *IEEE Transactions on Antennas and Propagation*, 50(2):233–243, February 2002.
- [52] J. Lee and H. L. Bertoni. Coupling at L, T and cross junctions in tunnels and urban street canyons. In *Vehicular Technoloty Conference*, volume 1, pages 274–278. IEEE, 2001 Spring.
- [53] F. Lotse and A. Wejke. Propagation measurements for microcells in central stockholm. In *Vehicular Technology Conference*, pages 539–541. IEEE, 1990.
- [54] S. F. Mahmoud and J. R. Wait. Geometrical optical approach for electromagnetic wave propagation in rectangular mine tunnels. *Radio Science*, 9(12):1147–1158, December 1974.
- [55] E. A. J. Marcatili and R. A. Schmeltzer. Hollow metallic and dielectric waveguides for long distance optical transmission and lasers. *The Bell System Technical Journal*, pages 1783–1809, July 1964.
- [56] D. Marcuse. Mode conversion caused by surface imperfections of a dielectric slab waveguide. *The Bell System Technical Journal*, pages 3187–3215, December 1969.

- [57] D. Marcuse. Radiation losses of dielectric waveguides in terms of the power spectrum of the wall distortion function. *The Bell System Technical Journal*, pages 3233–3242, December 1969.
- [58] D. Marcuse. Derivation of coupled power equations. *The Bell System Technical Journal*, 51(1):229–237, January 1972.
- [59] D. Marcuse. Fluctuations of the power of coupled modes. *The Bell System Technical Journal*, 51(8):1793–1800, October 1972.
- [60] D. Marcuse. Higher-order loss processes and the loss penalty of multimode operation. *The Bell System Technical Journal*, 51(8):1819–1836, October 1972.
- [61] D. Marcuse. Hollow dielectric waveguide for distributed feedback lasers. *IEEE Journal of Quantum Electronics*, QE-8(7):661–669, July 1972.
- [62] D. Marcuse. Power distributions and radiation losses in multimode dielectric slab waveguides. *The Bell System Technical Journal*, 51(2):429–454, February 1972.
- [63] D. Marcuse. Pulse propagation in multimode dielectric waveguides. *The Bell System Technical Journal*, 51(6):1199–1232, July-Aug 1972.
- [64] D. Marcuse. *Theory of Dielectric Optical Waveguides*. Academic Press, second edition, 1991.
- [65] T. L. Marzetta. Blast training: Estimating channel characteristics for high capacity space-time wireless. In *37th Annual Allerton Conference on Communication, Control and Computing*, Monticello, IL, September 1999. IEEE.
- [66] S. E. Miller. coupled wave theory and waveguide applications. *The Bell System Technical Journal*, pages 661–719, May 1954.
- [67] A. F. Molisch, M. Steinbauer, and H. Asplund. "virtual cell deployment areas" and "cluster tracing" - new methods for directional channel modeling in microcells. In *Vehicular Technology Conference*. IEEE, 2002 Spring.

- [68] M. Nomoto, S. Abe, and M. Miyagi. Graphical representation of mode selectivity in hollow waveguides with and without inner dielectric layer: slab waveguide model. *Optics Communications*, 108:243–246, June 1994.
- [69] D. Pasquet. Accurate graphic resolution of the characteristic equations of a hollow dielectric slab waveguide. *International Journal of Infrared and Millimeter Waves*, 2(3):453–463, 1981.
- [70] D. Porrat, P. Kyritsi, and D. C. Cox. MIMO capacity in hallways and adjacent rooms. In *Globecom*. IEEE, 2002.
- [71] S. Ramo, J. R. Whinnery, and T. Van Duzer. *Fields and Waves in Communication Electronics*. John Wiley & Sons, third edition, 1994.
- [72] T. S. Rappaport. *Wireless Communications Principles and Practices*. Prentice Hall PTR, 1996.
- [73] S. O. Rice. Reflection of electromagnetic waves from slightly rough surfaces. In M. Kline, editor, *The Theory of Electromagnetic Waves*, pages 315–378. Dover Publications, 1965. Reprint of a 1951 publication of Interscience Publishers.
- [74] K. Sakai and M. Koshihara. Analysis of electromagnetic field distribution in tunnels by the boundary-element method. *IEE Proceedings*, 137(4):202–208, August 1990.
- [75] H. Shimizu, J. Masui, M. Ishii, K. Sakawa, and T. Kobayashi. LOS and NLOS path-loss and delay characteristics at 3.35GHz in a residential environment. *IEICE Transactions Fundamentals*, E83-A(7):1356–1364, July 2000.
- [76] D.-S. Shiu, G. J. Foschini, M. J. Gans, and J. M. Kahn. Fading correlation and its effect on the capacity of multielement antenna systems. *IEEE Transactions on Communications*, 48(3):502–512, March 2000.
- [77] W. C. Stone. Electromagnetic signal attenuation in construction materials. Technical Report NISTIR 6055, NIST, October 1997. NIST Construction Automation Program Report No. 3.

- [78] G. L. Stüber. *Principles of Mobile Communication*. Kluwer Academic Publishers, 1996.
- [79] D. Swierk and A. Heimrath. Random multimode optical media: I. mode coupling process in slab waveguide with stochastic wall perturbations. *Journal of Modern Optics*, 39(4):681–688, 1992.
- [80] S. Y. Tan and H. S. Tan. UTD propagation model in an urban street scene for microcellular communications. *IEEE Transactions on Electromagnetic Compatibility*, 35(4):423–428, November 1993.
- [81] S. Y. Tan and H. S. Tan. Propagation model for microcellular communications applied to path loss measurements in Ottawa city streets. *IEEE Transactions on Vehicular Technology*, 44(2):313–317, May 1995.
- [82] S. Y. Tan and H. S. Tan. A microcellular communications propagation model based on the uniform theory of diffraction and multiple image theory. *IEEE Transactions on Antennas and Propagation*, 44(10):1317–1326, October 1996.
- [83] L. Tyler. *Notes on Waves*. Stanford Bookstore, 1998. Notes for the Course EE241.
- [84] R. Vacek. Electromagnetic wave propagation in general multimode waveguide structures exhibiting simultaneously attenuation, dispersion and coupling phenomena. In *Microwave and Optoelectronics Conference*, pages 599–605. IEEE, 1997.
- [85] J. Walfisch and H. L. Bertoni. A theoretical model of UHF propagation in urban environments. *IEEE Transactions on Antennas and Propagation*, 36(12), December 1988.
- [86] J. H. Whitteker. Measurements of path loss at 910 MHz for proposed microcell urban mobile systems. *IEEE Transactions on Vehicular Technology*, 37(3):125–129, August 1988.
- [87] J. H. Whitteker, 2001. Private Communication.
- [88] Y. P. Zhang and Y. Hwang. Enhancement of rectangular tunnel waveguide model. In *Asia Pacific Microwave Conference*, pages 197–200, 1997.